

**Instruments and techniques
for analysing the time-resolved
transverse phase space distribution
of high-brightness electron beams**

Dissertation

zur

Erlangung des akademischen Grades

Doktor-Ingenieur (Dr.-Ing.)

der Fakultät für Informatik und Elektrotechnik

der Universität Rostock

vorgelegt von

M.Eng. Dipl.-Ing. (FH) Jeniffa Rudolph

geb. am 08.07.1982 in Hennigsdorf

Rostock, 18. September 2012

Gutachter: Prof. Dr. Ursula van Rienen, Universität Rostock
Prof. Dr. Andreas Jankowiak, Helmholtz-Zentrum Berlin
Prof. Dr. Thomas Weis, Technische Universität Dortmund

Datum der Einreichung: 18. September 2012

Datum der Verteidigung: 29. November 2012

Abstract

This thesis deals with the instruments and techniques used to characterise the transverse phase space distribution of high-brightness electron beams. In particular, methods are considered allowing to measure the emittance as a function of the longitudinal coordinate within the bunch (slice emittance) with a resolution in the ps to sub-ps range.

The main objective of this work is the analysis of techniques applicable for the time-resolved phase space characterisation for future high-brightness electron beam sources and single-pass accelerators based on these. The competence built up by understanding and comparing different techniques is to be used for the design and operation of slice diagnostic systems for the Berlin Energy Recovery Linac Project (*BERLinPro*). In the framework of the thesis, two methods applicable for slice emittance measurements are considered, namely the zero-phasing technique and the use of a transverse deflector. These methods combine the conventional quadrupole scan technique with a transfer of the longitudinal distribution into a transverse distribution. Measurements were performed within different collaborative projects. The experimental setup, the measurement itself and the data analysis are discussed as well as measurement results and simulations. In addition, the phase space tomography technique is introduced. In contrast to quadrupole scan-based techniques, tomography is model-independent and can reconstruct the phase space distribution from simple projected measurements. The developed image reconstruction routine based on the Maximum Entropy algorithm is introduced. The quality of the reconstruction is tested using different model distributions, simulated data and measurement data. The results of the tests are presented.

The adequacy of the investigated techniques, the experimental procedures as well as the developed data analysis tools could be verified. The experimental and practical experience gathered during this work, the implemented data analysis routines and the tomography tools form the basis for the future implementation and use of time-resolved diagnostics in *BERLinPro*. Though the design of the diagnostic systems is still in its early stages, an estimation of suitable parameters of a deflector to be used for bunch characterisation downstream of the gun is specified in a first step within this work.

Kurzfassung

Die vorliegende Dissertation befasst sich mit Instrumenten und Techniken, die zur Charakterisierung des transversalen Phasenraums hoch-brillanter Elektronenstrahlen eingesetzt werden. Es werden insbesondere Methoden betrachtet, die eine Bestimmung der Emittanz in Abhängigkeit der longitudinalen Koordinate im Elektronenbunch (Scheiben-Emittanz) mit einer zeitlichen Auflösung im ps bis sub-ps Bereich ermöglichen.

Ziel der Arbeit ist die Analyse von Techniken, die eine zeitaufgelöste Untersuchung der Phasenraumverteilung von zukünftigen hoch-brillanten Elektronenstrahlquellen und auf diesen basierenden Single-Pass Beschleunigern ermöglichen. Die erworbenen Kompetenzen sollen für die Auslegung und den Betrieb von Systemen zur Scheiben-Diagnose für das Berlin Energy Recovery Linac Project (*BERLinPro*) eingesetzt werden. Im Rahmen der Arbeit werden zwei Methoden betrachtet, die eine Messung der Scheiben-Emittanz ermöglichen: Die Zero-Phasing Technik und der transversal ablenkende Deflektor. Beide Methoden basieren auf der Kombination aus der konventionellen Quadrupolscan-Technik und einer Umwandlung der longitudinalen Verteilung des Elektronenpulses in eine transversale Verteilung. Es werden Messungen vorgestellt, die im Rahmen zweier Kollaborationsprojekte an verschiedenen Photoinjektoren durchgeführt wurden. Hierbei werden der experimentelle Aufbau, die Messprozedur, die Analyse der Messdaten und gewonnene Resultate sowie Simulationen beleuchtet. Zusätzlich wird die Phasenraum-Tomographie eingeführt. Diese modellunabhängige Technik ermöglicht die Rekonstruktion der realen Phasenraum-Verteilung aus einfachen projizierten Messungen. Eine auf dem Maximum Entropie Algorithmus basierende Routine zur Bildrekonstruktion wird vorgestellt. Die Routine wird mittels verschiedener Modellverteilungen, simulierter Daten und Messungen getestet und die Ergebnisse dieser Untersuchungen werden diskutiert.

Die Eignung der eingesetzten Techniken und experimentellen Methoden sowie der zur Datenanalyse angewandten Prozeduren konnte bestätigt werden. Die theoretischen und praktischen Erfahrungen, die im Verlauf dieser Arbeit gewonnen wurden, die entwickelten Analysemethoden sowie die Tomographie-Werkzeuge bilden die Grundlage für zukünftige Anwendungen zur zeitaufgelösten Diagnose für *BERLinPro*. Die Auslegung der experimentellen Umsetzung befindet sich noch in der Startphase. In einem ersten Schritt konnten die Anforderungen an einen Deflektor spezifiziert werden, der für eine detaillierte Charakterisierung der Elektronenpakete kurz nach der Elektronenquelle für *BERLinPro* vorgesehen ist.

Acknowledgements

I would particularly like to thank Prof. Dr. Ursula van Rienen for giving me the opportunity of defending my Phd at the Universität Rostock and Prof. Dr. Andreas Jankowiak, the head of the Institute of Accelerator Physics at HZB, for greatly supporting me and my work. Furthermore, I want to thank Dr. Thorsten Kamps for encouraging me to write my dissertation.

I greatly appreciate the supervision and advice of Dr. Michael Abo-Bakr who was always open-minded for extensive discussions of my thoughts and results. I am very grateful for his introductions to the simulation programs I used within my work and for providing me with starter kits of example files. I wish to thank him for the headache-causing days and hours we spent discussing problems, as those of implementing the tomographic reconstruction which proved to be particularly intractable. He was my first contact for questions and always able to encourage me whenever I was stuck in a problem.

I am most grateful to Dr. Jochen Teichert who made it possible for me to take the very first zero-phasing measurements at ELBE. He supported me to become familiar with the machine and answered all my questions even during the usual night shifts foreseen for the measurements. If needed, he went to the tunnel with a measuring tape to provide me with parameters. Without his great patience with machine optimisation, I would hardly have been able to manage threading the beam through the dogleg. At this point, I also like to thank the whole ELBE crew for delivering beam for my measurements and helping me setting up and controlling the machine.

Many thanks go to Prof. Dr. Pietro Musumeci for enabling me to take measurements using the transverse deflector at PEGASUS as well as to Joshua Moody and Cheyne Scoby for supporting me by introducing me to the lab and setting up the machine for the measurements.

I would also like to thank Terry Atkinson for helping me with the measurements at the linac which I used to test my tomography tools and for mutually keeping our heads over water, especially when Michael was absent. A special thank goes to Bettina Kuske who always supported me with valuable advice, food for thoughts and different point of views, which I am very grateful for. She managed rescuing me when I was suffering from acute ‘Satzfindungsstörung’. Thanks to Dr. Axel Neumann for checking my understanding of the deflector technique and to Alessandro Ferrarotto for the discussions and explanations concerning the deflector.

Furthermore, I want to express my deep gratitude to my colleagues who were willing to take the effort of proof-reading my thesis and helped me with a multitude of comments and suggestions. Here, I would particularly like to thank Dr. Michael Abo-Bakr, Terry Atkinson and Bettina Kuske.

My final acknowledgement is to my parents, Margitta and Wolfgang, and to my partner and friend, Mike, who were always there for me when I needed them and never stopped believing in me and my abilities. Thank you.

Contents

1	Introduction	1
2	Phase space and emittance	3
2.1	Phase space definition	3
2.2	Statistical definition of emittance	4
2.3	Significance of the emittance in light sources	7
3	Projected emittance measurement techniques	9
3.1	Slit- and pepperpot-techniques	9
3.2	Quadrupole scan technique	10
3.2.1	Quadrupole scan in thin lens approximation	12
3.2.2	Quadrupole scan for a thick quadrupole magnet	13
4	Slice emittance and slice energy spread	15
4.1	Slice emittance and slice emittance measurement techniques	15
4.2	Zero-phasing technique	17
4.2.1	Beam size downstream of the spectrometer magnet	18
4.3	Transverse deflector technique	19
4.3.1	Beam size downstream of the deflector	20
4.4	Technique to measure the slice energy spread	23
4.5	Temporal resolution criterion	24
5	Slice emittance measurements	27
5.1	The zero-phasing technique at ELBE	27
5.1.1	Measurement setup	28
5.1.2	Experimental results	44
5.1.3	Simulation results	49
5.1.4	Conclusion	54
5.2	Transverse deflector technique at PEGASUS	55
5.2.1	Measurement setup	57
5.2.2	Experimental results	58
5.2.3	Conclusion	60
5.3	Conclusion of slice emittance measurement techniques	61
6	Phase space tomography	65
6.1	General principle of tomography	65
6.1.1	Tomographic image reconstruction	65
6.1.2	Implementation of image reconstruction	69
6.1.3	Testing the reconstruction algorithm	71
6.2	Phase space tomography	76
6.2.1	Application of the quadrupole scan for phase space tomography	78
6.3	Phase space tomography at the BESSY II pre-injector linac	81
6.3.1	Data analysis procedure	81
6.3.2	Phase space reconstruction	82
6.4	Conclusion of phase space tomography	84

7	Slice diagnostics for <i>BERLinPro</i>	85
7.1	Transverse deflecting cavity for the <i>BERLinPro</i> gun	86
7.1.1	Aperture of the beam pipe	87
7.1.2	Deflecting voltage requirements	88
8	Summary	91
A	Dispersion function for setups A1, A2 and A3	93
B	Results of the zero-phasing measurements	95
C	Testing the tomographic reconstruction algorithm	99
	References	101

List of Figures

2.1	Characterisation of the phase space ellipse by the emittance and Twiss-parameters	6
2.2	Transformation of the phase space ellipse along the beamline	7
2.3	Matching of the photon and electron beam in a FEL resonator	8
3.1	Single-slit technique for emittance measurements	9
3.2	Double-slit technique for emittance measurements	10
3.3	Quadrupole scan technique for emittance measurements	12
4.1	Working principle of emittance compensation	16
4.2	Zero-phasing technique for slice emittance measurements	18
4.3	Magnetic field components of the TM_{110} -mode for a pillbox cavity.	19
4.4	Transverse deflector technique for slice emittance measurements	20
4.5	Geometric consideration of the deflection by the TCAV	23
4.6	Combination of deflector and dipole to measure the slice energy spread . .	24
4.7	Definition of the resolution criterion for slice diagnostics	25
5.1	View of the ELBE SRF-injector	28
5.2	Experimental setup for zero-phasing measurements at ELBE	29
5.3	Imaging properties of the ‘Browne-Buechner’ spectrometer	30
5.4	Resolution and magnification map for a point source	33
5.5	Resolution and magnification map for a parallel source	34
5.6	Imaging of the ‘Browne-Buechner’ spectrometer for a parallel source . . .	35
5.7	Resolution and magnification map for a realistic source	36
5.8	Simulation of the spectrometer imaging properties	37
5.9	Construction model of the spectrometer unit	39
5.10	Overview of possible spectrometer magnet installations	41
5.11	p - x correlations in the slit and screen plane for setup A1	42
5.12	p - x correlations in the slit and screen plane for setup A2	43
5.13	p - x correlations in the slit and screen plane for setup A3	44
5.14	Spectrometer magnet mounted in the ELBE beamline	45
5.15	Sequence of spectrometer screen images	46
5.16	Preparation of spectrometer images for analysis	47
5.17	Zero-phasing: slice emittance for measurement ‘series 6’	48
5.18	Zero-phasing: slice emittance measurement results for all series.	49
5.19	Zero-phasing: simulation procedure using different program codes	50
5.20	Simulated slice emittance values downstream of the injector	51
5.21	Space charge effects as a function of the beam energy	52
5.22	Simulated slice emittance values for measurement period 2010	53
5.23	Evaluation of the data analysis routine	54
5.24	Comparison of measured and simulated slice emittance values	55
5.25	View of the PEGASUS photoinjector	56
5.26	Experimental setup for deflector measurements at PEGASUS	57
5.27	Deflector measurements: slice emittance for measurement ‘series 1’	59
5.28	Deflector technique: slice emittance measurement results for all series . .	60

6.1	Working principle of tomography	66
6.2	Binned model distribution and projected values	67
6.3	Binned model distribution and definition of multipliers	68
6.4	Calculation of bin intersections	70
6.5	Convergence studies: development of projected values, density and emittance	72
6.6	Emittance overestimation due to weighted polygon coordinates	72
6.7	Emittance and calculation time as a function of the number of bins	73
6.8	Reconstruction of a normal distribution (3 histograms, 25 bins)	74
6.9	Reconstruction of overlapping normal distributions (5 histograms, 25 bins)	75
6.10	Reconstruction of a normal distribution from non-equidistant projections	76
6.11	Working principle of phase space tomography in horizontal direction . . .	77
6.12	Periodic β -functions in a two-cell FODO lattice	79
6.13	Reconstruction of a phase space distribution from simulated projections. .	80
6.14	Beam size and phase advance as a function of the quadrupole strength . .	81
6.15	Reconstructed phase space distribution of the BESSY II pre-injector linac	83
7.1	Schematic representation of <i>BERLinPro</i>	85
7.2	First model of the RF deflector foreseen to characterise the <i>BERLinPro</i> gun	86
7.3	Minimum aperture as a function of the normalised emittance	87
7.4	Required deflector voltage as a function of the beam energy and the β -function	89
7.5	Number of slices analysable within the resolution as a function of RF power	89
A.1	First (red) and second order (blue) dispersion along the beamline for A1.	93
A.2	First (red) and second order (blue) dispersion along the beamline for A2.	93
A.3	First (red) and second order (blue) dispersion along the beamline for A3.	94
B.1	Zero-phasing: slice emittance for measurement ‘series 1’ (2010)	95
B.2	Zero-phasing: slice emittance for measurement ‘series 2’ (2010)	95
B.3	Zero-phasing: slice emittance for measurement ‘series 3’ (2010)	95
B.4	Zero-phasing: slice emittance for measurement ‘series 4’ (2010)	96
B.5	Zero-phasing: slice emittance for measurement ‘series 5’ (2010)	96
B.6	Zero-phasing: slice emittance for measurement ‘series 6’ (2010)	96
B.7	Zero-phasing: slice emittance for measurement ‘series 7’ (2011)	97
B.8	Zero-phasing: slice emittance for measurement ‘series 8’ (2011)	97
B.9	Zero-phasing: slice emittance for measurement ‘series 9’ (2011)	97
B.10	Zero-phasing: slice emittance for measurement ‘series 10’ (2011)	98
C.1	Model distribution of three partly overlapping normal distributions. . . .	99
C.2	Reconstruction of overlapping normal distributions (3 histograms, 25 bins)	99
C.3	Reconstruction of overlapping normal distributions (10 histograms, 25 bins)	99

List of Tables

5.1	Parameters of the ELBE SRF-injector	27
5.2	Temporal resolution of the zero-phasing measurements	39
5.3	Specifications of the implemented spectrometer	40
5.4	Dispersion in the slit and screen plane for setups A1, A2 and A3	42
5.5	Settings for zero-phasing measurements	46
5.6	Simulated ASTRA output parameters of the SRF-injector	51
5.7	Estimation of space charge effects	52
5.8	Parameters of the PEGASUS photoinjector	56
5.9	Parameters used to estimate the resolution of the deflector measurements	58
5.10	Deflector technique: summary of the slice emittance results	60
5.11	Comparison of the zero-phasing and the deflector technique	61
5.12	Estimation of the required deflecting voltage and RF power	62
5.13	Estimated resolution for the zero-phasing and the deflector technique under measurement conditions	63
6.1	comparison of the emittance and Twiss-parameters of the model and the reconstructed normal distribution	74
6.2	Emittance and Twiss-parameters from reconstruction of a normal distribu- tion using non-equidistant projections	75
6.3	Comparison of results from quadrupole scan and tomographic reconstruc- tion from simulated data	80
6.4	Quadrupole strength and calculated phase advance for the ideal views . .	82
6.5	Summary of results from tomographic phase space reconstruction	83
7.1	Expected beam and deflector parameters for the <i>BERLinPro</i> gun	87
7.2	Required deflecting voltage	88
B.1	Zero-phasing: measured slice emittance values for all series	98

1 Introduction

Electron accelerators being the basis of synchrotron radiation sources serve as powerful scientific instruments for a broad range of research fields including material sciences, biology and medicine. The most important parameter describing the quality of the photon beam is the brightness, giving a measure of the photon density in phase space. The quest for high-brightness photon beams is essentially based on user's demand for high photon densities on their research probes. High brightness of the photon beam requires a high-brightness electron beam as the beam parameters being directly correlated. To achieve a high electron beam brightness, a low emittance is needed.

In light sources based on storage rings, the electron beam experiences radiation damping and quantum excitation resulting in a comparatively large equilibrium emittance depending on the beam energy and the machine's beam optics. Many fourth generation light sources are based on linear accelerators (linacs). These single-pass machines, as Free Electron Lasers (FELs), do not undergo excitation processes. Hence, the emittance of linacs is determined by the emittance being delivered by the electron source and only shrinking with the beam energy. Therefore, the research on low-emittance electron sources is of fundamental interest. Superconducting radio-frequency (SRF)-photoinjectors are a highly promising electron source especially for continuous-wave (cw) operation because of the combination of electron production by photoemission and superconducting accelerator technology. Due to the transverse and longitudinal structure of the laser pulse being directly transferred to the electron bunch and the instantaneous high-gradient acceleration in the SRF cavity, bunches of high charge and low emittance can be generated. The verification and control of the achieved source performance establishes the substantial need for a detailed characterisation of the electron beam's projected parameters and its phase space distribution. Moreover, the detailed knowledge of the variation of the beam parameters along the bunch is essential for certain applications and advanced techniques allowing to measure 'sliced parameters' become necessary. The optimisation of the FEL process or emittance compensation techniques may serve as examples requiring slice diagnostics.

This work describes instruments and measurement techniques applicable for time-resolved diagnostics for high-brightness electron sources and single-pass accelerators. The main objective of the work is to gather experience with the design and operation of slice diagnostics systems, which will be an essential contribution for electron beam characterisation of the Berlin Energy Recovery Linac Project (*BERLinPro*) [1]. *BERLinPro* is a demonstrator ERL under development at the Helmholtz-Zentrum Berlin (HZB). The machine is designed to deliver a high-current and low-emittance beam of 50 MeV beam energy.

In the first and second chapter of this work, the emittance parameter describing the beam's focusability and techniques to measure the projected emittance of electron beams, as the quadrupole scan technique, are introduced. Afterwards, the need for slice diagnostics is further motivated and the basic working principles of the techniques are explained. The methods described are the zero-phasing technique and the transverse deflector technique for slice emittance measurements. Both rely on a combination of the quadrupole scan with the possibility to transfer the longitudinal particle distribution into a transverse distribution. The techniques have been experimentally applied within different collabo-

rative research projects. The zero-phasing technique is implemented at the Elektronen Linearbeschleuniger für Strahlen hoher Brillanz und niedriger Emittanz (ELBE) [2] at the Helmholtz-Zentrum Dresden-Rossendorf (HZDR) in order to characterise the newly installed SRF-photoinjector foreseen as the future electron source for ELBE. Chapter 5 gives a detailed description of the setup, the procedure, simulations and the data analysis routine as well as results of the measurements. The measurements using the deflector were taken at the Photoelectron Generated Amplified Spontaneous Radiation Source (PEGASUS) photoinjector [3] at the University of California Los Angeles (UCLA). The procedure and results of these measurements are examined more briefly. The working principle of phase space tomography to reconstruct the actual projected phase space distribution of the beam is introduced in Chapter 6. A routine for image reconstruction was developed and tests using model distributions and simulated data are discussed. In addition, the results of the first application of this routine to measured data taken within the commissioning phase of the new pre-injector linac for the electron storage ring BESSY II are given. The work is finished with a brief discussion of the slice diagnostic needs of *BERLinPro* and design requirements for the deflector foreseen for the gun characterisation of this project.

2 Phase space and emittance

This chapter gives an introduction to the emittance parameter for electron beam description. The transverse and longitudinal phase spaces are defined and the emittance is introduced as a measure of the phase space area occupied by the electrons. Afterwards, the commonly used rms-emittance is derived starting from a statistical point of view. The derivations in this section follow [4] and [5].

2.1 Phase space definition

The particles in a beam can be described by a density distribution $f(x, p_x, y, p_y, z, p_z)$ of a set of points in six-dimensional phase space. The volume occupied by the particles in (x, p_x, y, p_y, z, p_z) can be expressed as

$$V_6 = \int_V dx dp_x dy dp_y dz dp_z, \quad (2.1)$$

where x , y and z are the coordinates describing the particle position and p_x , p_y and p_z are the corresponding momenta of the particles. The projection of the particle distribution onto a particular phase plane yields three two-dimensional sub-phase spaces (x, p_x) , (y, p_y) and (z, p_z) . According to Liouville's theorem [4], the six-dimensional phase space volume stays constant under the influence of conservative forces. Assuming the motion of particles in one sub-space to be uncoupled of all others, each sub-space can be considered individually. In this case Liouville's theorem holds true for each of these phase spaces. The occupied area for each sub-space is given by

$$A_x = \int_A dx dp_x \quad (2.2)$$

$$A_y = \int_A dy dp_y \quad (2.3)$$

$$A_z = \int_A dz dp_z. \quad (2.4)$$

A_z describes the longitudinal phase space. A_x and A_y refer to the transverse phase space which are considered in this work. The following derivations are exemplarily shown for the horizontal x -plane, all formulas hold true in the vertical y -plane as well.

The relativistic transverse momentum p_x can be calculated using the following relation

$$p_x = m_0 \gamma v_x = m_0 \gamma \frac{dx}{dt} = m_0 \gamma \frac{dx}{dz} \frac{dz}{dt} = m_0 \gamma \beta c \frac{dx}{dz} = m_0 c \beta \gamma x', \quad (2.5)$$

where m_0 is the rest mass, γ the relativistic factor $\gamma = 1/\sqrt{1-\beta^2}$ and the relativistic factor β is defined as the ratio of the particle velocity to the vacuum light velocity $\beta = v/c = (dz/dt)/c$. Inserting these relations into Eq. (2.2) gives an expression for the transverse phase space area A_x in terms of the transverse particle coordinate x and its

corresponding divergence angle x'

$$A_x = m_0 \gamma \beta c \int_A dx dx'. \quad (2.6)$$

As stated above, the transverse phase space area defined by particle coordinate and momentum (x, p_x) stays constant in time. Since it is easier to measure the angular trajectory than the momentum of a particle, it is convenient to make use of the phase space definition shown in Eq. (2.6). The geometric emittance is defined to give a measure of the occupied phase space regardless of its shape. It can be expressed as

$$\varepsilon_x = \frac{A_x}{\pi m_0 \gamma \beta c} = \frac{1}{\pi} \int_A dx dx'. \quad (2.7)$$

It is convenient to define a normalised emittance which stays constant during acceleration

$$\varepsilon_{x,n} = \beta \gamma \varepsilon_x = \frac{\beta \gamma}{\pi} \int_A dx dx'. \quad (2.8)$$

The normalised emittance is a figure of merit describing the focusability of the beam independent of the beam energy.

2.2 Statistical definition of emittance

A statistical distribution of N particles in 2D-phase space (x, x') may be characterised by its moments. Using the general relations [6]

$$\langle x \rangle = \frac{1}{N} \sum_{i=1}^N x_i \quad (2.9)$$

$$\text{var}(x) = \frac{1}{N} \sum_{i=1}^N (x_i - \langle x \rangle)^2 \quad (2.10)$$

$$\text{cov}(x, x') = \frac{1}{N} \sum_{i=1}^N (x_i - \langle x \rangle) (x'_i - \langle x' \rangle) \quad (2.11)$$

for the mean, variance and covariance, a covariance matrix σ describing the particle distribution [7, 8] may be defined as

$$\sigma = \begin{bmatrix} \text{var}(x) & \text{cov}(x, x') \\ \text{cov}(x', x) & \text{var}(x') \end{bmatrix}. \quad (2.12)$$

For a coordinate system characterising the phase space chosen such that the mean values $\langle x \rangle$ and $\langle x' \rangle$ equal zero, the covariance matrix simplifies to

$$\sigma = \begin{bmatrix} \langle x^2 \rangle & \langle x x' \rangle \\ \langle x' x \rangle & \langle x'^2 \rangle \end{bmatrix}. \quad (2.13)$$

Statistically, the root-mean-square (rms)-value σ is defined as $\sigma_x = \sqrt{\sigma_{xx}} = \sqrt{\text{var}(x)} = \sqrt{\text{cov}(x, x)}$. The elements $\sigma_{xx'}$ and $\sigma_{x'x}$ are equal and the covariance matrix can be

expressed as

$$\sigma = \begin{bmatrix} \sigma_{xx} & \sigma_{xx'} \\ \sigma_{x'x} & \sigma_{x'x'} \end{bmatrix} = \begin{bmatrix} \sigma_{11} & \sigma_{12} \\ \sigma_{21} & \sigma_{22} \end{bmatrix} = \begin{bmatrix} \sigma_{11} & \sigma_{12} \\ \sigma_{12} & \sigma_{22} \end{bmatrix}. \quad (2.14)$$

The covariance matrix is called ‘beam matrix’ or ‘sigma matrix’ (‘ σ -matrix’) when used for particle beam description. In general, the phase space area occupied by the particle distribution can be described by a surrounding ellipse. This so-called phase space ellipse can be represented by the σ -matrix. Since the particle ensemble is not a hard-edged distribution with sharp boundaries, it is useful to define a parameter which describes the ellipse containing a certain fraction of particles. The equation of an ellipse centred at $\langle x \rangle = \langle x' \rangle = 0$ may be formulated by [9]

$$\begin{bmatrix} x \\ x' \end{bmatrix}^T \sigma^{-1} \begin{bmatrix} x \\ x' \end{bmatrix} = k^2. \quad (2.15)$$

Here, σ^{-1} is the inverse of the symmetric σ -matrix and the variable k represents the number of standard deviations enclosed by the ellipse. The 1σ -ellipse corresponds to 68 % of normal distributed particles and is commonly used to describe electron beams. This leads to the relations

$$\begin{bmatrix} x \\ x' \end{bmatrix}^T \sigma^{-1} \begin{bmatrix} x \\ x' \end{bmatrix} = 1 \quad (2.16)$$

$$\begin{bmatrix} x & x' \end{bmatrix} \frac{1}{\det \sigma} \begin{bmatrix} \sigma_{22} & -\sigma_{12} \\ -\sigma_{12} & \sigma_{11} \end{bmatrix} \begin{bmatrix} x \\ x' \end{bmatrix} = 1, \quad (2.17)$$

which may also be written as

$$\frac{\sigma_{22} x^2 - 2\sigma_{12} xx' + \sigma_{11} x'^2}{\det \sigma} = 1. \quad (2.18)$$

Assuming an uncorrelated ellipse with semi-axes a and b coinciding with the axes of the (x, x') -coordinate system, the matrix element σ_{12} becomes zero and therefore

$$\frac{\sigma_{22} x^2}{\det \sigma} + \frac{\sigma_{11} x'^2}{\det \sigma} = 1. \quad (2.19)$$

The normal form to describe an ellipse is given by

$$\frac{x^2}{a^2} + \frac{x'^2}{b^2} = 1. \quad (2.20)$$

Comparison between Eqs. (2.19) and (2.20) leads to the relations

$$a^2 = \frac{\det \sigma}{\sigma_{22}} \quad \text{and} \quad b^2 = \frac{\det \sigma}{\sigma_{11}}. \quad (2.21)$$

The area A of an ellipse can be calculated by the geometrical relation $A = \pi ab$. Again for an uncorrelated ellipse ($\sigma_{12} = \sigma_{21} = 0$), the determinant of the σ -matrix is $\det \sigma = \sigma_{22} \sigma_{11}$ and the area of the phase space ellipse is equal to

$$A = \pi \sqrt{\sigma_{11} \sigma_{22}}. \quad (2.22)$$

The emittance was introduced as the occupied phase space area divided by π in Eq. (2.7). Therefore, it can be now expressed as

$$\varepsilon_x = \sqrt{\sigma_{11}\sigma_{22}}. \quad (2.23)$$

The uncorrelated ellipse may be rotated such that the semi-axes do no longer coincide with the coordinate axes. This introduces a correlation element $\sigma_{12} \neq 0$ while the enclosed area stays constant. Hence, Eq. (2.23) can be generalised to the form

$$\varepsilon_x^{\text{rms}} = \sqrt{\det \sigma} = \sqrt{\sigma_{11}\sigma_{22} - \sigma_{12}^2}. \quad (2.24)$$

This variable is called rms-emittance since its definition refers to a 1σ -phase space ellipse. In analogy to Eq. (2.8), the normalised rms-emittance is defined by

$$\varepsilon_{x,n}^{\text{rms}} = \beta \gamma \sqrt{\sigma_{11}\sigma_{22} - \sigma_{12}^2} \quad (2.25)$$

$$= \beta \gamma \sqrt{\langle x^2 \rangle \langle x'^2 \rangle - \langle xx' \rangle^2}. \quad (2.26)$$

This definition will be used in this thesis and it will be simply referred to as normalised emittance $\varepsilon_{x,n}$ omitting the index ‘rms’ from here on.

The previous considerations characterised the phase space ellipse using the variances and covariances σ_{11} , σ_{12} and σ_{22} . Other common parameters to describe the phase space ellipse are the Twiss-parameters α , β and γ [10]. The Twiss-parameters are defined as the σ -matrix elements normalised by the geometric emittance

$$\beta_x = \frac{\sigma_{11}}{\varepsilon_x}, \quad \alpha_x = -\frac{\sigma_{12}}{\varepsilon_x} \quad \text{and} \quad \gamma_x = \frac{\sigma_{22}}{\varepsilon_x} \quad (2.27)$$

and the σ -matrix can be expressed accordingly as

$$\sigma = \begin{bmatrix} \sigma_{11} & \sigma_{12} \\ \sigma_{12} & \sigma_{22} \end{bmatrix} = \varepsilon_x \begin{bmatrix} \beta_x & -\alpha_x \\ -\alpha_x & \gamma_x \end{bmatrix}. \quad (2.28)$$

Fig. 2.1 illustrates the size and orientation of the phase space ellipse characterised by the emittance and the Twiss-parameters. The appearance of the phase space ellipse and

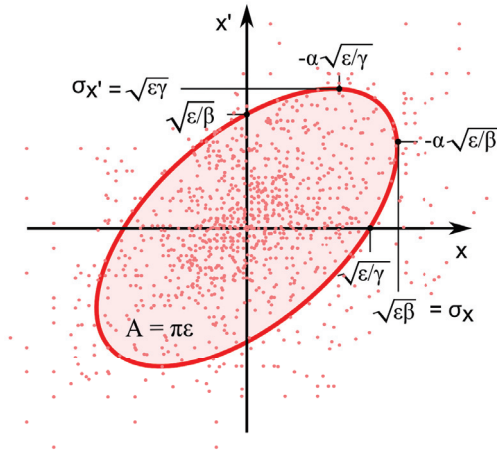


Figure 2.1: Definition of the phase space ellipse given in [10]. The Twiss-parameters are used to describe the size and orientation of the ellipse.

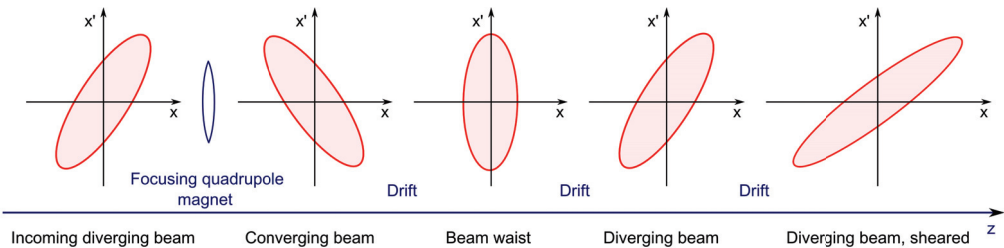


Figure 2.2: Transformation of the phase space ellipse through the beamline [10]. The beamline consists of a focusing quadrupole magnet followed by a drift section. The incoming beam is divergent. The beam is focused by the quadrupole magnet, passes a beam waist and diverges again. Shearing can be observed towards the end of the beamline.

hence the Twiss-parameters vary along the beamline depending on the optical elements. Fig. 2.2 shows the transformation through a short beamline consisting of a focusing quadrupole magnet followed by a drift section schematically. The incoming divergent beam is transformed to a converging beam. The beam reaches a minimum beam size at the waist and then diverges. A longer drift leads to shearing of the ellipse with a constant maximum x' -coordinate and increasing x -coordinate.

2.3 Significance of the emittance in light sources

The emittance parameter is of essential importance when electron beams are applied as drivers for light sources and FELs. Generally, a low emittance is a figure of merit. A low emittance is the basis to achieve a high brightness defined as $B \propto I/(\varepsilon_x \varepsilon_y)$. The brightness gives a measure of the electron density in phase space [4], i.e. a measure of the number of photons on the user's sample.

In light sources as storage rings, synchrotron radiation is produced in bending magnets and undulators. The properties of the radiated photon beams are directly correlated to the electron beam parameters. A low-emittance and high-brightness electron beam allows to achieve a photon beam of low emittance and hence high brightness.

In a FEL, the electron beam interacts with a photon beam within an undulator. The electron beam is modulated by the electromagnetic field of the photon beam. The resulting micro-bunch structure then causes the bunch to radiate coherently. FELs open up short wavelength regimes that are not available using conventional lasers [11]. Wavelengths down to a few Ångstrom have been demonstrated at the Linac Coherent Light Source (LCLS) X-ray FEL in Stanford [12]. The interaction requires optimum overlap of the beams along the complete undulator length. Thus, the beam size and the divergence and hence the emittance of the electron beam need to suit the photon beam parameters. Maximum coupling of the beams occurs for equal emittance of electron and photon beam. The emittance ε_{ph} of a diffraction-limited photon beam of wavelength λ_{ph} is given by $\varepsilon_{\text{ph}} = \lambda_{\text{ph}}/(4\pi)$ [10, 13]. Hence, the requirement on the normalised electron beam emittance can be expressed as

$$\varepsilon_n = \beta\gamma \frac{\lambda_{\text{ph}}}{4\pi}. \quad (2.29)$$

An intuitive description of the optimal matching is given in Fig. 2.3 for an on-axis beam in an optical resonator. Three different cases are shown, namely the emittance of the

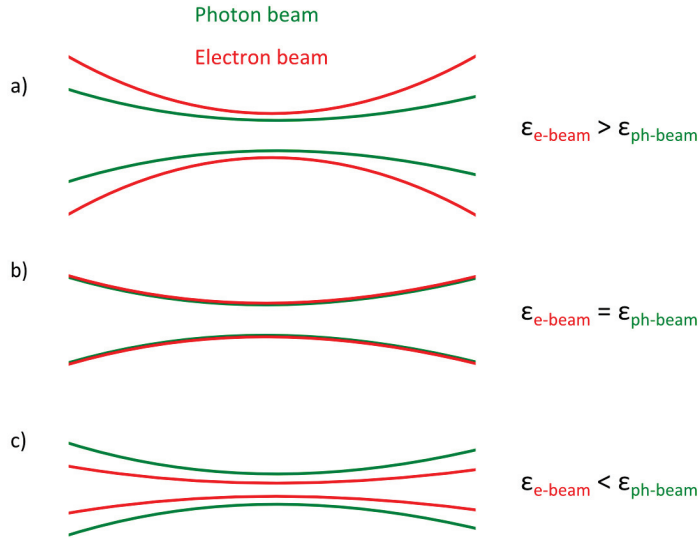


Figure 2.3: Schematic drawing of the overlap between electron beam (red) and photon beam (green) within an optical FEL resonator [14]. The photon beam has a fixed emittance value corresponding to the diffraction limit. In case a) the emittance of the electron beam is larger than the emittance of the photon beam and only part of the electrons contribute to the interaction. The optimum emittance matching described by Eq. (2.29) is given in case b). Case c) shows an electron beam of lower emittance such that interaction is restricted to a part of the photon beam.

electron beam being larger (a), equal (b) and smaller (c) than the emittance of the photon beam.

The smaller the wavelength of the FEL, the higher the demands on the beam emittance, as can be seen from Eq. (2.29). The normalised emittance required for successful lasing of the LCLS can be calculated using the design parameters of $E = 15$ GeV and $\lambda_{\text{ph}} = 0.15$ nm taken from [15] to be $\epsilon_n = 0.35$ mm mrad. X-ray FELs are operated as single-pass devices in self-amplified spontaneous emission (SASE)-mode since optical resonators are difficult to realise for the X-ray regime [11]. The saturation length describes the distance of interaction needed to achieve maximum radiation power. A small saturation length substantially reduces the cost of the undulator sections [16]. The saturation length can be essentially reduced by a lower emittance [17]. Additionally, the maximum output power of the FEL radiation is increasing for a lower emittance.

3 Projected emittance measurement techniques

The importance of the emittance as a figure of merit and for beam applications was discussed in the previous chapter, demonstrating the need for emittance measurements. This chapter gives a short overview of the most important techniques for projected emittance measurement and their working principles.

3.1 Slit- and pepperpot-techniques

This section gives an overview on the slit- and pepperpot-technique for emittance measurements [4, 5, 18]. Both these methods are very similar and the working principle is explained with the slit-technique.

The application of slit-techniques is restricted to the low energy regime due to the decrease of the geometric emittance and the beam divergence with increasing energy and the large penetration depth of high energy particles. The single-slit method uses a single-slit mask to cut a small fraction of the incoming beam which is referred to as beamlet. In contrast to the space charge dominated incoming beam, the beamlet is fully dominated by emittance since the charge of the beamlet is low compared to the total bunch charge. An image of the beamlet is projected onto a scintillator screen which is placed at a known distance of the slit mask. The position of the slit x_{slit} defines the horizontal position coordinate. Since the distance between slit and screen is known, the divergence corresponding to the slit position can be calculated from the centroid of the beamlet on the screen x_{screen} . Furthermore, the width $\sigma_{x'}$ of the beamlet gives a measure of the spread in divergence at the slit position and the light intensity on the screen is proportional to the number

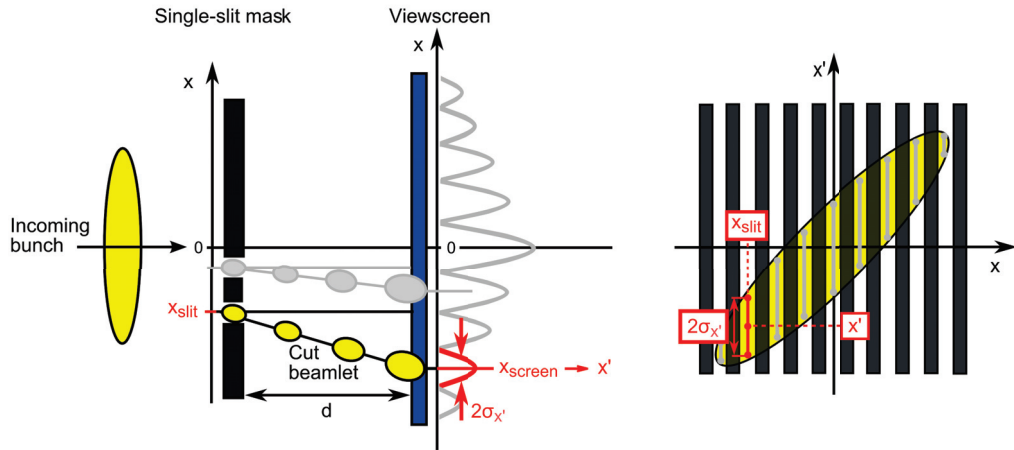


Figure 3.1: Working principle of the single-slit technique (left) and the principle of the phase space reconstruction for nine slit positions (right). The slit cuts a small beamlet from the beam and determines the x -coordinate. The beamlet propagates to a screen. From the image on the screen the corresponding divergence information can be determined. The procedure is repeated for different slit positions. Finally, the phase space ellipse can be reconstructed.

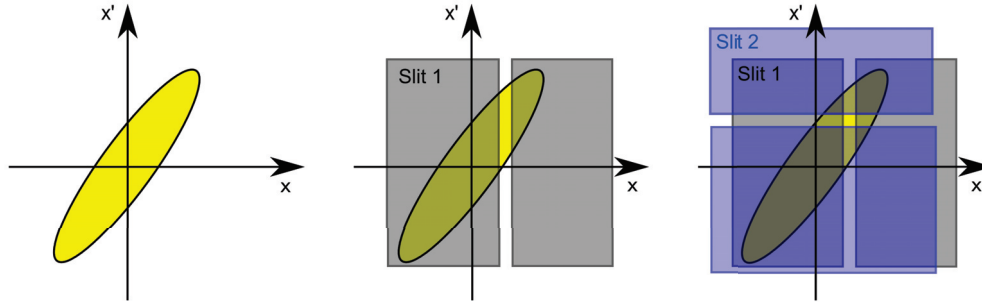


Figure 3.2: Phase space reconstruction for double-slit scan technique. The first slit cuts a small horizontal slice of the beam. Thus, the first slit defines the x -coordinate. A second slit rotated by 90° with respect to the first slit is used to analyse the x' -coordinate.

of particles in the beamlet. Scanning the slit over the whole beam allows to reconstruct the horizontal phase space distribution of the beam. In order to measure the emittance in both transverse planes, a second slit mask with the slit rotated by 90° is needed. Fig. 3.1 illustrates the working principle of a single-slit measurement. It shows the beamlet propagation (left side) and the reconstruction of the phase space area from the measured data as indicated above (right side).

Alternatively, a multi-slit mask can be used instead of scanning a single slit over the beam. This variation of the method has the advantage of the complete phase space information taken in a single-shot measurement and therefore avoids influence of beam fluctuations to the measurement results. It is also a faster method but one has to make sure the distance of the screen is properly set in order to avoid overlapping between projections. In single-slit measurements, the distance is limited to maximum values only by the signal to noise ratio [18]. A third modification of the method includes the use of a second slit which is perpendicular to the first instead of the screen to analyse the divergence distribution. The second slit is followed by a Faraday-cup which measures the current of the beamlet [8]. As described before, the first slit determines the position coordinate. The second slit is used to scan the divergence distribution for each position coordinate. Therefore, the intensity profile for each position can be determined and both beamlet centroid position and width can be used to reconstruct the phase space distribution. The phase space reconstruction for this method is illustrated in Fig. 3.2.

The pepperpot-technique makes use of the same principles as the slit-technique. It uses a multi-hole plate followed by an imaging screen instead of a multi-slit mask and therefore the emittance of both the transverse planes can be measured simultaneously [5].

3.2 Quadrupole scan technique

This section gives an introduction to the quadrupole scan technique. It is considered in more detail than the slit-methods since this technique was applied for the emittance measurements described in this work. A detailed description of the experimental procedure can be found in Chapter 5.

The quadrupole scan is a common procedure to measure the emittance, especially of electron beams that are not dominated by space charge. Moreover, it is the method of choice for beams of various energy ranges due to its simplicity and availability. The

essential advantage of the method is the fact that the existing components of the accelerator can be used. At least one quadrupole magnet followed by a drift section and a scintillator screen for beam size measurements are needed to determine the emittance.

In Section 2.2, the σ -matrix was introduced to describe the electron distribution. The transformation of the σ -matrix through the beamline can be expressed as [10]

$$\sigma(s) = M \cdot \sigma(0) \cdot M^T, \quad (3.1)$$

where $\sigma(0)$ and $\sigma(s)$ are the σ -matrices at the start of the beamline and at the position s respectively. M is the 2×2 transfer matrix describing the beam optics between these two positions in the considered transverse plane. It is simply given by its elements

$$M = \begin{bmatrix} m_{11} & m_{12} \\ m_{12} & m_{22} \end{bmatrix}. \quad (3.2)$$

Eq. (3.1) states that the σ -matrix can be calculated at any arbitrary position in a beamline if both the σ -matrix at a defined position and the beam transport optics are known. Recalling the definition of the σ -matrix which identified the element σ_{11} as the squared rms beam size reveals the possibility to directly determine σ_{11} from the measured beam size. According to Eq. (3.1), the element σ_{11} at position s is given by

$$\sigma_{11}(s) = m_{11}^2 \sigma_{11}(0) + 2 m_{11} m_{12} \sigma_{12}(0) + m_{12}^2 \sigma_{22}(0). \quad (3.3)$$

This indicates that three different measurements, each with varied and known beam optics, lead to a set of three equations with three unknowns allowing to calculate all elements of the σ -matrix at the start of the beamline. This can be expressed in matrix form [19] as

$$\begin{bmatrix} \sigma_{11}^{(a)}(s) \\ \sigma_{11}^{(b)}(s) \\ \sigma_{11}^{(c)}(s) \end{bmatrix} = \underbrace{\begin{bmatrix} m_{11}^{2(a)} & 2 m_{11}^{(a)} m_{12}^{(a)} & m_{12}^{2(a)} \\ m_{11}^{2(b)} & 2 m_{11}^{(b)} m_{12}^{(b)} & m_{12}^{2(b)} \\ m_{11}^{2(c)} & 2 m_{11}^{(c)} m_{12}^{(c)} & m_{12}^{2(c)} \end{bmatrix}}_A \cdot \begin{bmatrix} \sigma_{11}(0) \\ \sigma_{12}(0) \\ \sigma_{22}(0) \end{bmatrix}. \quad (3.4)$$

The indices a, b and c denote the different beam size measurements. The unknown σ -matrix elements $\sigma_{11}(0)$, $\sigma_{12}(0)$ and $\sigma_{22}(0)$ can be calculated according to

$$\begin{bmatrix} \sigma_{11}(0) \\ \sigma_{12}(0) \\ \sigma_{22}(0) \end{bmatrix} = A^{-1} \cdot \begin{bmatrix} \sigma_{11}^{(a)}(s) \\ \sigma_{11}^{(b)}(s) \\ \sigma_{11}^{(c)}(s) \end{bmatrix}. \quad (3.5)$$

Once the σ -matrix was reconstructed, the emittance can be calculated as its determinant, as given by Eq. (2.24). Moreover, the Twiss-parameters can be determined using Eq. (2.27) allowing to reconstruct the phase space ellipse at the start of the beamline.

In principle, variation of the beam optics can be realised by measuring the size of the beam at different locations in the beamline while keeping all beamline elements constant [10, 20]. An easier possibility to implement the quadrupole scan method is to vary the strength of a single quadrupole magnet and measure the beam size on a screen downstream of the quadrupole magnet. Fig. 3.3 shows the working principle of the quadrupole scan technique schematically. Three exemplary settings of the quadrupole magnet are shown with increasing magnet strength from case a) to case c). The figure clarifies the development

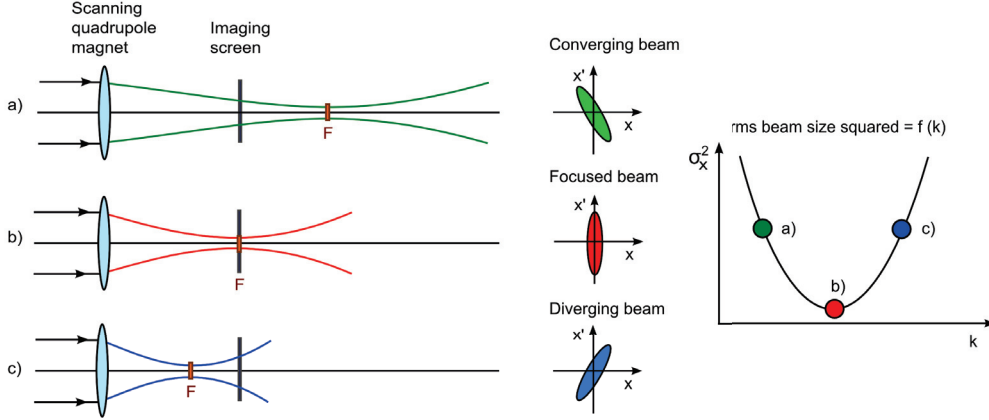


Figure 3.3: Schematic drawing of the working principle of the quadrupole scan technique. Three settings of a quadrupole magnet with increasing strength from a) to c) are shown.

of the beam envelope and the position of the focal points as well as the orientation of the phase space ellipse. Furthermore, it shows the parabolic dependence between squared rms beam size and the strength of the quadrupole magnet. In case a) a low magnet strength is applied and the beam gets focused downstream of the screen. This results in a large beam on the screen. Now, the strength of the quadrupole magnet is increased, as in case b). The focal point of the beam is located on the screen and a minimum beam size is measured. Further increase of the strength leads to case c). The beam is focused upstream of the screen. Thus, it is diverging in the screen plane and a higher beam size is observed. Clearly, the beam size for more than three settings of the quadrupole magnet can be measured to better define the parabolic dependence and apply a fitting routine, see next section.

3.2.1 Quadrupole scan in thin lens approximation

This section gives a short analytical analysis of the quadrupole scan using the matrix formalism. The quadrupole magnet is assumed to fulfil the thin lens approximation which requires the length of the quadrupole magnet to be much shorter than its focal length $l \ll f$. The focal length of the quadrupole magnet is given by $f = 1/(kl)$ with the length l and strength k of the quadrupole magnet. Therefore, the thin lens criterion can also be expressed as $l^2 \ll 1/k$. The matrix notation used in the following is taken from [10].

The total transfer matrix for a beamline consisting of different optical elements is given as the product of the matrices of the individual elements. The transfer matrix of a drift section of length d is given by

$$M_d = \begin{bmatrix} 1 & d \\ 0 & 1 \end{bmatrix} \quad (3.6)$$

and the thin quadrupole magnet is described by

$$M_q = \begin{bmatrix} 1 & 0 \\ -kl & 1 \end{bmatrix}. \quad (3.7)$$

Therefore, the total transfer matrix of a thin quadrupole magnet followed by a drift

section is found to be

$$M = M_d \cdot M_q = \begin{bmatrix} 1 - kld & d \\ -kl & 1 \end{bmatrix}. \quad (3.8)$$

The dependence in Eq. (3.3) can be rewritten using Eq. (3.8)

$$\sigma_{11}(s) = (1 - kld)^2 \sigma_{11}(0) + 2d(1 - kld) \sigma_{12}(0) + d^2 \sigma_{22}(0), \quad (3.9)$$

which is equal to

$$\begin{aligned} \sigma_{11}(s) = & k^2 \cdot ((ld)^2 \sigma_{11}(0)) + k \cdot (-2ld \sigma_{11}(0) - 2ld^2 \sigma_{12}(0)) \\ & + (\sigma_{11}(0) + 2d \sigma_{12}(0) + d^2 \sigma_{22}(0)). \end{aligned} \quad (3.10)$$

The squared beam size $\sigma_{11}(s)$ is a quadratic function of k having the general form

$$y(x) = ax^2 + bx + c. \quad (3.11)$$

The polynomial relation between $\sigma_{11}(s)$ and the strength of the quadrupole magnet can be used for a simple fitting procedure which returns the coefficients a , b and c [21]. The σ -matrix elements can be calculated from the coefficients using the following relations

$$\sigma_{11}(0) = \frac{a}{(ld)^2} \quad (3.12)$$

$$\sigma_{12}(0) = -\frac{b + 2d\sigma_{11}(0)}{2d^2} \quad (3.13)$$

$$\sigma_{22}(0) = \frac{c - \sigma_{11}(0) - 2d\sigma_{12}(0)}{d^2}. \quad (3.14)$$

3.2.2 Quadrupole scan for a thick quadrupole magnet

In case the thin lens approximation does not hold, a more general description of the quadrupole magnet is needed. In this section, the derivation used for the thin quadrupole magnet is applied for a thick quadrupole magnet. The transfer matrix for a thick quadrupole magnet is given by

$$M_q = \begin{bmatrix} \cos(\sqrt{k}l) & \frac{1}{\sqrt{k}} \sin(\sqrt{k}l) \\ -\sqrt{k} \sin(\sqrt{k}l) & \cos(\sqrt{k}l) \end{bmatrix}. \quad (3.15)$$

A beamline section consisting of a thick quadrupole magnet followed by a drift section is described by the total transfer matrix

$$M = \begin{bmatrix} \cos(\sqrt{k}l) - d\sqrt{k} \sin(\sqrt{k}l) & \frac{1}{\sqrt{k}} \sin(\sqrt{k}l) + d \cos(\sqrt{k}l) \\ -\sqrt{k} \sin(\sqrt{k}l) & \cos(\sqrt{k}l) \end{bmatrix}, \quad (3.16)$$

and Eq. (3.3) yields the following relation for the beam size

$$\begin{aligned} \sigma_{11}(s) = & \sigma_{11}(0) \cdot \left[\cos(\sqrt{k}l) - d\sqrt{k} \sin(\sqrt{k}l) \right]^2 \\ & + \sigma_{12}(0) \cdot \left[2 \left[\cos(\sqrt{k}l) - d\sqrt{k} \sin(\sqrt{k}l) \right] \cdot \left[\frac{1}{\sqrt{k}} \sin(\sqrt{k}l) + d \cos(\sqrt{k}l) \right] \right] \\ & + \sigma_{22}(0) \cdot \left[\frac{1}{\sqrt{k}} \sin(\sqrt{k}l) + d \cos(\sqrt{k}l) \right]^2. \end{aligned} \quad (3.17)$$

This function cannot exactly be transformed into the quadratic form given in Eq. (3.11). Therefore, another procedure to determine the σ -matrix elements is necessary. The least-squares procedure [22] provides a convenient possibility for analysis. The method allows to determine the parameters of a theoretical function best representing the measured data. In order to realise the parameter determination, a function χ^2 is introduced. The function is defined as the quadratic sum of the difference between measured data and theoretical prediction weighted by the error of the measured data. A minimisation of χ^2 yields the required function parameters. In the particular case of the quadrupole scan, the theoretical function is generally given by Eq. (3.3) and the χ^2 -function can be expressed as

$$\chi^2 = \sum_{i=1}^N \left[\frac{\sigma_{11}^{(i)}(s) - \left(m_{11}^{(i)2} \sigma_{11}(0) + 2 m_{11}^{(i)} m_{12}^{(i)} \sigma_{12}(0) + m_{12}^{(i)2} \sigma_{22}(0) \right)}{F(\sigma_{11}^{(i)}(s))} \right]^2. \quad (3.18)$$

Here, N is the number of measurements, i is the index of each measurement and $F(\sigma_{11}^{(i)}(s))$ is the error of each measured beam size. Minimisation yields the σ -matrix elements at the start of the beamline needed for the emittance calculation. In practice, a large number of beam size measurements is used for the least-squares analysis in order to reduce the experimental uncertainties.

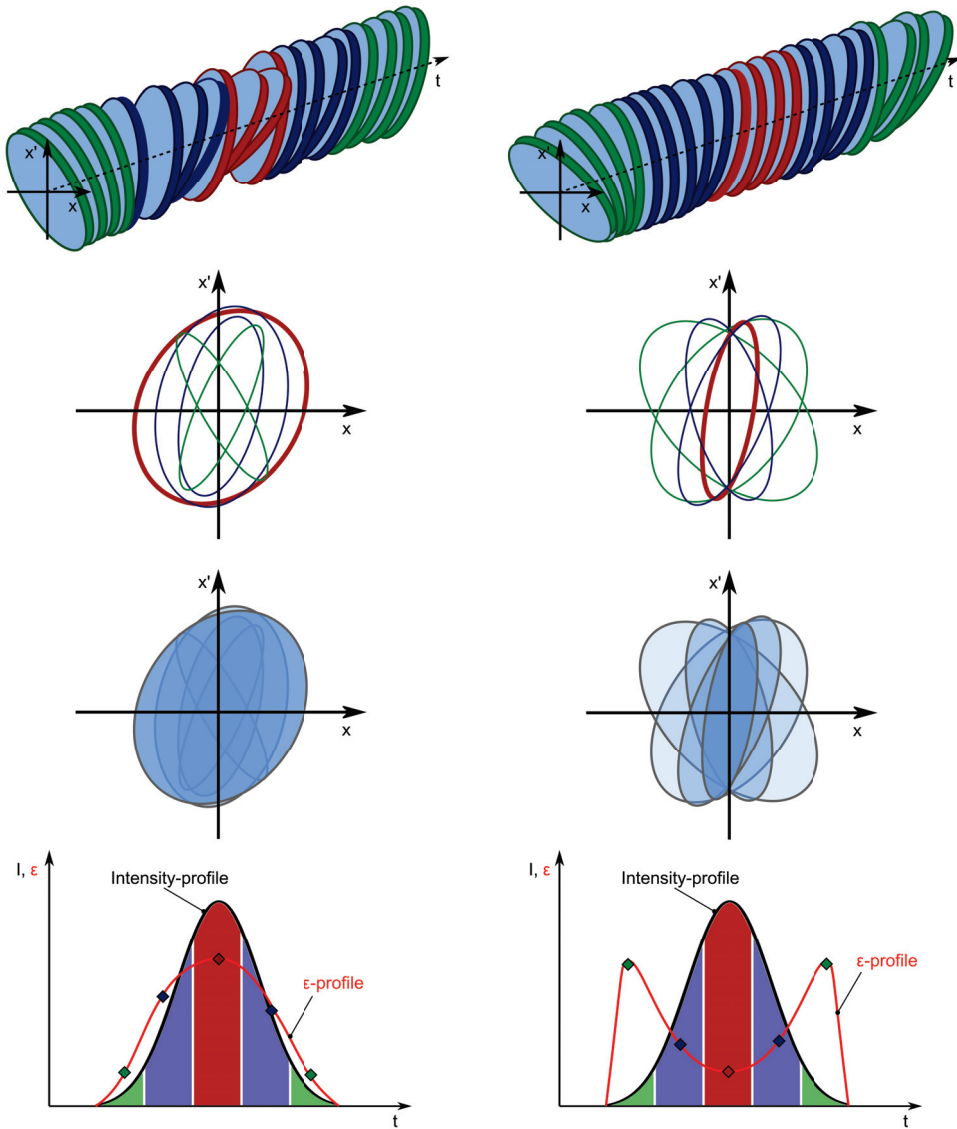
4 Slice emittance and slice energy spread

A variety of beam parameter measurements rely on imaging the beam on a screen. These measurements yield projected values of the entire bunch. High-performance applications of electron beams require time-resolved measurements of beam parameters along the bunch. These are referred to as ‘slice’ parameters. The ‘slice emittance’, ‘slice energy spread’ and techniques allowing to measure these quantities are considered in this chapter.

4.1 Slice emittance and slice emittance measurement techniques

Conventional emittance measurements using the quadrupole scan technique introduced in Section 3.2 require a number of beam size measurements on a screen placed in the beamline. A projected beam size of the overall bunch is measured, leading to a projected emittance calculation. A variety of effects contribute to a growth of the projected emittance. Many of them depend on the longitudinal position within the bunch. Such are space charge defocusing influenced by the amount of charge in a slice, the energy variation induced by RF acceleration resulting in different focusing of magnetic lenses and time-dependent RF fields inducing transverse kicks depending on the slice position [23]. These effects cause a different orientation and size of the phase space ellipses of different slices and therefore a growth of the projected emittance. The increase due to differently oriented phase spaces can partly be compensated for by implementing an ‘emittance compensation’ scheme. Emittance compensation allows to adjust the orientation of the phase space ellipses of the slices and thereby reduces the overall projected emittance.

The principle of emittance compensation has been first proposed by Carlsten in [24]. It relies on the possibility of compensating the emittance growth resulting from linear space charge forces using focusing solenoidal fields. The defocusing due to space charge depends on the electron density and causes the slices’ phase space distributions to rotate with different velocities leading to misalignment of the phase space ellipses. Using an appropriate solenoidal field allows to induce a kick to the slices such that the faster rotating slices lag behind the slower rotating slices. The faster slices are able to catch up to the slower slices while passing through a drift section following the solenoid. Alignment of the slices’ phase space is achieved in a distance depending on the strength of the kick. Instantaneous onset of acceleration at this point allows to reduce the influence of space charge defocusing and the low projected emittance is maintained. The working principle of emittance compensation is illustrated in Fig. 4.1, with Fig. 4.1a showing the uncompensated and Fig. 4.1b presenting the compensated case. The upper part of the schematics shows the phase space ellipses of 20 thin ‘micro’-slices within the bunch. Assuming a number of five slices per bunch to be analysed for this example, each of these ‘macro’-slices is composed of four micro-slices of the same colour. The phase space ellipses of the macro-slices corresponding to the projected phase space of the four micro-slices are indicated in the middle of Fig. 4.1, using the introduced colour code. In addition, the same phase space ellipses are shown, this time shaded according to the charge content of the slices. The darker the blue colour, the more charge is included. The lower part of the schematic indicates both the intensity and the emittance profile along the temporal



(a) No emittance compensation applied. The phase space ellipses of the ‘micro’-slices have different orientations. Especially, the centre slices (red) show misalignment (top), which mirrors in the phase space of the ‘macro’-slices (centre). The red ‘macro’-slice has the largest emittance while the emittance decreases towards the ends of the bunch as represented in the emittance profile along the bunch, see below.

(b) Emittance compensation applied. The ‘micro’-slices are aligned in the centre of the bunch. This leads to a reduced ‘macro’-slice emittance and a flat emittance characteristic in the high intensity region of the bunch centre. The phase space ellipses of outer slices are considered less relevant due to the low charge content.

Figure 4.1: Schematic representation of the working principle of emittance compensation. The upper part illustrates the phase space ellipses of 20 different ‘micro’-slices along the temporal coordinate within the bunch. Four successive ‘micro’-slices are summarised as a ‘macro’-slice and are coloured accordingly. The resulting phase space ellipse of each ‘macro’-slice is shown in the middle. The additional phase space presentation takes into account the charge content of the slices. The intense blue colour indicates high charge, pale blue is for lower charge content. Below, both the intensity and the emittance profile along the bunch are given.

coordinate of the bunch. The phase space ellipses of the micro-slices in Fig. 4.1a vary in orientation with the most misalignment due to space charge effects observed for the centre slices. This results in a larger phase space area occupied by the electrons of the bunch centre and smaller phase space ellipses for the outer macro-slices. As a result, the projected emittance of the bunch is large, as can be seen from the shaded phase space representation. The corresponding emittance profile reveals a maximum of emittance in the high-intensity centre of the bunch. Considering Fig. 4.1b, the orientation of the phase space ellipses has been influenced as described above. Primarily, the high-intensity slices of the bunch centre are aligned. The influence of the compensation on the low-intensity slices is considered less relevant. The emittance characteristic along the bunch changed and the smallest emittance values are achieved in the high-intensity regime. Consequently, the projected emittance of the bunch is essentially reduced. The emittance profile reveals two maxima for the low-intensity head and tail of the bunch and a flat characteristic of low emittance values in the centre of the bunch.

The results of a successful compensation can be summarised as a reduced projected emittance of the total bunch due to low intensity in slices of large emittance and a range providing low emittance and high brightness values in the high-intensity centre of the bunch. Both these effects are of relevance for applications of high-brightness electron beams: The reduction of the projected emittance of the electron beam increases the photon beam brightness. The characteristic of the emittance along the bunch is relevant for operation of FELs. In the FEL, the interaction takes place within small longitudinal fractions of the bunch, which is due to the electrons slipping behind the photons. The radiation produced within the individual fractions sums up to the total radiation output of the FEL. Thus, optimum conditions for interaction within the slices provide an optimised FEL process. Relevant parameters to characterise and evaluate the process are the beam overlap, the saturation length and the total amount of radiation power, see Section 2.3. All of these are positively influenced by a low emittance and hence a high brightness of the electron beam. The range of constant low emittance and high beam brightness in the centre of the bunch enables good beam overlap, a short saturation length and a high radiation power, all being approximately constant for the individual slices. The low-brightness tails of the bunch do not contribute to the FEL process.

The measurement of the slice emittance delivering the orientation of the phase space ellipses along the bunch is a crucial requirement for the initialisation and verification of the emittance compensation [25]. In order to make the longitudinal slices accessible for measurements, the longitudinal distribution is transferred into a transverse distribution which can be observed on a screen. Two different methods are applicable for the conversion: The zero-phasing technique and the transverse deflector technique. The following sections give a short overview of the working principles and the temporal resolution of both methods. The schematic illustrations and derivations are given for one transverse plane only. They hold true in the other plane accordingly.

4.2 Zero-phasing technique

The zero-phasing technique uses an energy chirped beam that is sent through a spectrometer magnet to transfer the longitudinal beam distribution into a transverse distribution. Slice emittance measurements are possible in combination with the quadrupole scan technique introduced in Section 3.2. The application of the zero-phasing technique for

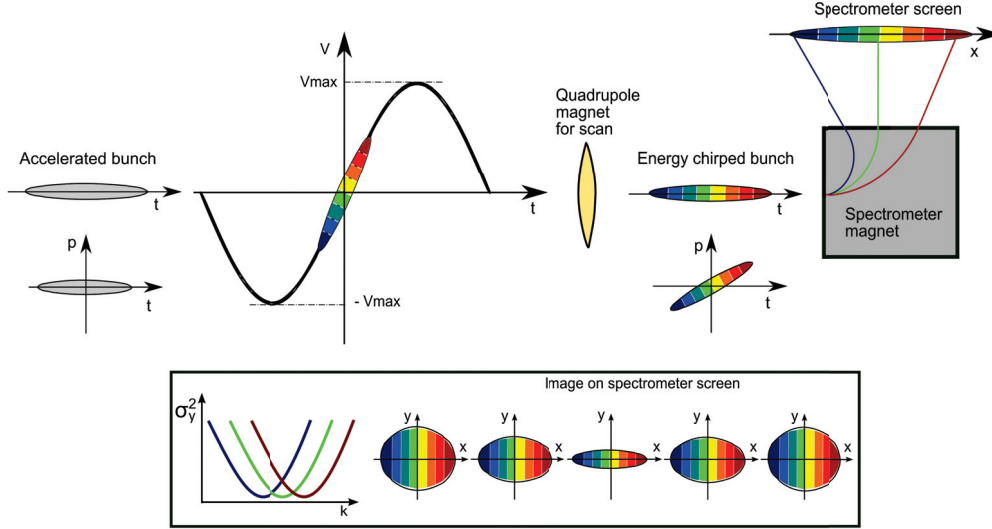


Figure 4.2: Working principle of the zero-phasing technique. The shown setup presumes a horizontally deflecting spectrometer magnet. Therefore, only the vertical beam size and hence the vertical emittance for each slice can be measured.

emittance and bunch length measurements has been demonstrated before [25, 26, 27]. Fig. 4.2 explains the working principle schematically. The pre-accelerated bunch is sent through a cavity at the zero-crossing phase of the RF wave. In doing so, a linear correlation between the longitudinal position in the bunch and the particle momentum is induced. Afterwards, the momentum chirped bunch passes through a horizontally deflecting spectrometer magnet. Due to the difference in momentum, the longitudinal slices experience different bending radii, resulting in a transverse separation of the slices observable on the screen. Now, the vertical beam size σ_y can be measured for each of the longitudinal slices. Applying the quadrupole scan technique to the chirped beam allows to reconstruct the vertical emittance for the individual slices. The horizontal beam size and hence emittance becomes accessible using a vertically deflecting dipole magnet.

The correlation between the particle position on the screen and the longitudinal position of the particle in the bunch has to be linear in order to unambiguously reconstruct the longitudinal slice position t from the observed transverse position x_s . This in turn demands for a linear momentum chirp as well as for a linear correlation between the momentum chirp and the coordinate on the screen. The correlation between the longitudinal position and the momentum is induced by the slope of the RF wave. Minimum slope variation occurs at the zero-crossing phase due to the sinusoidal characteristic of the RF wave. Operation at non-zero off-crest phases is also possible as long as the induced energy correlation remains approximately linear. The linearity of the t - p -correlation has to be verified for the chosen phase of the cavity and the bunch length. Each particle momentum is then correlated to a coordinate on the screen using the dispersion generated in the spectrometer magnet. Linearity of the p - x correlation is only achieved if the first order dispersion predominates higher order effects.

4.2.1 Beam size downstream of the spectrometer magnet

The beam size on the screen $\sigma_{x,s}$ composes of the beam size from emittance $\sigma_{x,\varepsilon}$ and a dispersive term $\sigma_{x,\eta}$, as given in Eq. (4.1). Expressing the dispersive beam size as

the dispersion and the relative momentum spread σ_p/p_0 of the beam from reference momentum p_0 leads to Eq. (4.2). Effects from first and second order horizontal dispersion, η_x and $\eta_{2,x}$, are included here.

$$\sigma_{x,s} = \sqrt{\sigma_{x,\varepsilon}^2 + \sigma_{x,\eta}^2} \quad (4.1)$$

$$\sigma_{x,s} = \sqrt{\sigma_{x,\varepsilon}^2 + \left[\eta_x \frac{\sigma_p}{p_0} + \eta_{2,x} \left(\frac{\sigma_p}{p_0} \right)^2 \right]^2} \quad (4.2)$$

Assuming $\sigma_{x,\varepsilon} \ll \sigma_{x,\eta}$, the particle coordinate on the screen can be calculated accordingly by

$$\Rightarrow x_s = \eta_x \frac{\Delta p}{p_0} + \eta_{2,x} \left(\frac{\Delta p}{p_0} \right)^2, \quad (4.3)$$

where $\Delta p/p_0$ is the relative momentum deviation for the considered particle. Eq. (4.3) provides the relation $|\eta_x| \gg |\eta_{2,x}| \cdot \Delta p_{\max}/p_0$ that has to be fulfilled in order to achieve linearity of the p - x -correlation. Here, a maximum overall relative energy deviation $\Delta p_{\max}/p_0$ is used. Thus, not only the chirp cavity phase but also the beam transport optics determining the dispersion have to be carefully checked to verify their appropriateness for slice emittance measurements.

4.3 Transverse deflector technique

The deflector technique for slice emittance measurements relies on a combination of a transverse deflecting RF cavity (TCAV) and the quadrupole scan technique. The deflector induces a time-dependent transverse kick to the beam, directly transferring the longitudinal distribution to a transverse distribution. This technique is more direct than the zero-phasing technique since the intermediate step of inducing an energy correlation is not required. Applications of the deflector for slice emittance as well as bunch length measurements have been described in [29, 30, 31]. The working principle of the transverse deflector technique is shown in Fig. 4.4. The electron bunch passes the deflector cavity at the zero-crossing phase of the RF. The deflecting voltage induces a vertical kick on the beam which depends linearly on the longitudinal position within the bunch. Thus, head

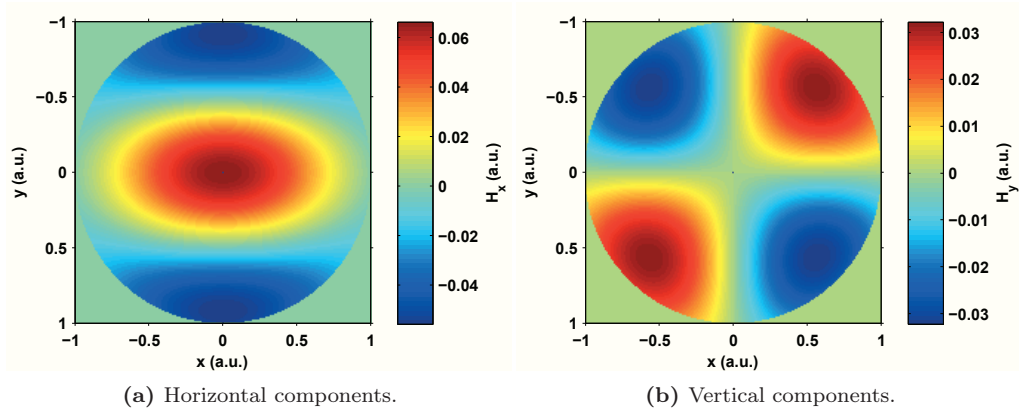


Figure 4.3: Magnetic field components for the TM_{110} -mode for a pillbox cavity calculated using Matlab [28].

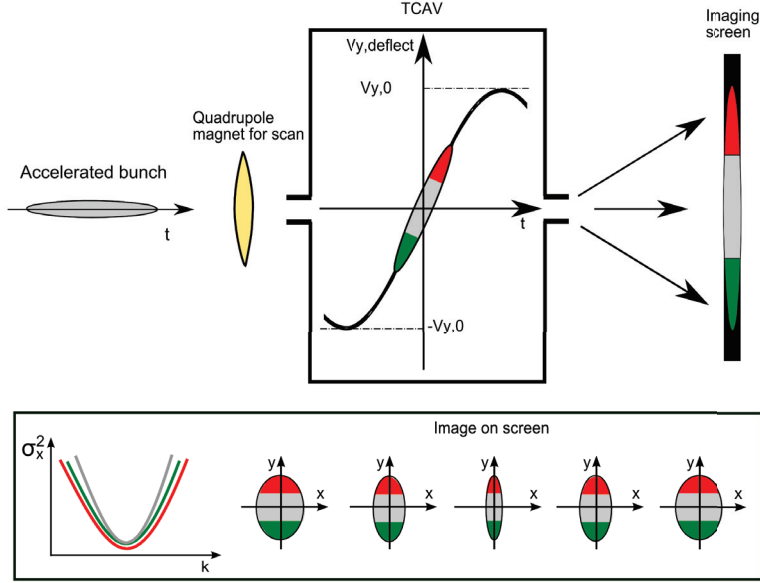


Figure 4.4: Working principle of the transverse deflecting cavity. The schematic representation shows a deflector inducing a vertical kick to the beam. With this specific setup the horizontal beam size and hence the horizontal emittance of the slices can be measured.

and tail of the bunch experience kicks in opposite direction such that the longitudinal beam distribution is transferred into a vertical distribution. A screen placed downstream of the deflector is used to observe the vertical distribution and the horizontal beam size can be measured for different longitudinal slices. A linear correlation between the transverse and the time coordinate is needed for unambiguous reconstruction of the longitudinal position from a transverse coordinate on the screen.

Generally, transverse magnetic or electric field components are required to achieve transverse deflection. The TM_{110} -cavity mode provides deflection induced by transverse components of the magnetic field while the transverse electric fields are zero. Fig. 4.3 shows the distribution of the transverse magnetic field components for the TM_{110} -mode for a pillbox cavity. The x -components of the magnetic field are presented in Fig. 4.3a, where a maximum field amplitude is observed in the centre of the cavity. Fig. 4.3b clarifies that the y -components of the magnetic field are zero on the longitudinal axis of the cavity and for any positions of coordinates $x = 0$ or $y = 0$. Therefore, the kick induced by this polarisation of the TM_{110} -mode acts in vertical direction.

4.3.1 Beam size downstream of the deflector

The total beam size $\sigma_{y,s}$ on the screen placed downstream of the deflector is given by the quadratic sum of the beam size from emittance $\sigma_{y,\varepsilon}$ and the beam size caused by the deflector $\sigma_{y,tcav}$

$$\sigma_{y,s} = \sqrt{\sigma_{y,\varepsilon}^2 + \sigma_{y,tcav}^2}. \quad (4.4)$$

High accuracy in the reconstruction of the longitudinal coordinate is achieved for a total beam size being dominated by the deflector $\sigma_{y,\varepsilon} \ll \sigma_{y,\text{tcav}}$, leading to

$$\sigma_{y,s} \approx \sigma_{y,\text{tcav}}. \quad (4.5)$$

Thus, an expression for $\sigma_{y,\text{tcav}}$ needs to be found to estimate the beam size on the screen. For this purpose, a transverse deflecting voltage will be introduced. The electrons are assumed to enter the deflector on its longitudinal axis and the induced kick is assumed to be small. The derivations follow [32] and [33].

The vertical screen coordinate of a particle at a certain position in the bunch depends on the strength of the induced vertical deflection. The deflection is caused by time-dependent electric and magnetic fields of the general form $\vec{E} = \vec{E}(z, t) = \vec{E}_0(z) \cos(\omega t + \varphi)$ and $\vec{B} = \vec{B}(z, t) = \vec{B}_0(z) \sin(\omega t + \varphi)$, where ω is the angular frequency of the RF wave, t the time and φ the start phase. $\vec{B}_0(z)$ and $\vec{E}_0(z)$ are the amplitudes of the magnetic and electric field vector at a longitudinal position z in the beamline. The fields act on the electron beam as the Lorentz-force

$$\vec{F} = e \left(\vec{v} \times \vec{B} + \vec{E} \right), \quad (4.6)$$

with the elementary charge e and the velocity \vec{v} of the moving electron. Considering only the vertical component of the Lorentz-force which causes the kick in vertical direction yields

$$F_y = e (v_z B_x + E_y). \quad (4.7)$$

The on-axis transverse components of the electric field E_x and E_y are zero for the TM₁₁₀-mode [33] and the kick is purely caused by the horizontal component of the magnetic field B_x . Moreover, the TM₁₁₀-mode provides magnetic field components which are constant along the longitudinal axis z of an ideal pillbox cavity. Therefore, only the temporal behaviour of $B_x(z, t) = B_x(t) = B_{x,0} \sin(\omega t + \varphi)$ has to be taken into account. Eq. (4.7) can be rewritten as

$$F_y = e v_z B_{x,0} \sin(\omega t + \varphi), \quad (4.8)$$

where $B_{x,0}$ is the amplitude of the horizontal magnetic field.

A transverse deflecting voltage V_y may be introduced as an equivalent variable describing the deflection along the deflector of length L . From the relation $W_{\text{el}} = eV_y$ for the electric work one finds

$$V_y = \frac{1}{e} \int_{-L/2}^{L/2} F_y \, dz. \quad (4.9)$$

Inserting Eq. (4.8), the voltage can be expressed as

$$V_y = v_z B_{x,0} \int_{-L/2}^{L/2} \sin(\omega t + \varphi) \, dz, \quad (4.10)$$

where v_z is constant along the deflector. Now, the bunch centroid is assumed to pass the centre of the cavity given by $t = 0$ at $\varphi = 0$. The transformation of the temporal variable

t to a spatial coordinate z in form of $t = z/v_z$ leads to

$$V_y = v_z B_{x,0} \int_{-L/2}^{L/2} \sin\left(\omega \frac{z}{v_z}\right) dz. \quad (4.11)$$

Integration gives

$$V_y = \frac{v_z^2 B_{x,0}}{\omega} \left[-\cos\left(\omega \frac{z}{v_z}\right) \right]_{-L/2}^{L/2}. \quad (4.12)$$

As expected, the voltage seen by a particle at the bunch centroid z_0 is zero

$$V_y(z_0) = -\frac{v_z^2 B_{x,0}}{\omega} \left(\cos\left(\omega \frac{L}{2v_z}\right) - \cos\left(-\omega \frac{L}{2v_z}\right) \right) = 0. \quad (4.13)$$

Let $\Delta z = z - z_0$ describe the particle's position with respect to the bunch centroid. The voltage seen by a particle at a coordinate $z_0 + \Delta z$ is derived using addition theorems

$$\begin{aligned} V_y(z_0 + \Delta z) &= -\frac{v_z^2 B_{x,0}}{\omega} \left[\cos\left(\frac{\omega z_0}{v_z}\right) \cos\left(\frac{\omega \Delta z}{v_z}\right) + \sin\left(\frac{\omega z_0}{v_z}\right) \sin\left(\frac{\omega \Delta z}{v_z}\right) \right]_{-L/2}^{L/2} \\ &= -2 \frac{v_z^2 B_{x,0}}{\omega} \sin\left(\frac{\omega L}{2v_z}\right) \sin\left(\frac{\omega \Delta z}{v_z}\right). \end{aligned} \quad (4.14)$$

The voltage difference $\Delta V_y = V_y(z_0) - V_y(z_0 + \Delta z)$ is then found to be $\Delta V_y = -V_y(z_0 + \Delta z)$. Replacing ω by $2\pi f = 2\pi c/\lambda$ and using $v_z = \beta c$ gives

$$\Delta V_y = \frac{\beta^2 c \lambda B_{x,0}}{\pi} \sin\left(\frac{\pi L}{\beta \lambda}\right) \sin\left(\frac{2\pi \Delta z}{\beta \lambda}\right). \quad (4.15)$$

Here, f and λ are the frequency and wavelength of the RF. Summarising the constant terms to an amplitude (peak) value of the deflecting voltage $V_{y,0}$ leads to

$$\Delta V_y = V_{y,0} \sin\left(\frac{2\pi \Delta z}{\beta \lambda}\right). \quad (4.16)$$

For Δz in the range of bunch lengths of 1 mm corresponding to ~ 3 ps, the approximation

$$\Delta V_y \approx V_{y,0} \frac{2\pi \Delta z}{\beta \lambda} \quad (4.17)$$

is valid to describe the difference in deflecting voltage affecting particles separated by Δz . The relation derived for the deflecting voltage will be used in the following to find an expression for the beam size on the screen.

The correlation between the transverse voltage and the vertical coordinate of a particle on the screen can be derived following a simple geometric consideration illustrated in Fig. 4.5. The deflecting angle y'_0 is given by the ratio of the transverse to the longitudinal momentum p_y/p_z . Assuming a drift section between the deflector and the screen, a particle of the start coordinates $(y_0 = 0, y'_0)$ transforms to a coordinate y_s at the screen given by $y_s = d \tan y'_0$ which is $y_s \approx d y'_0$ for small deflecting angles. It follows from Fig. 4.5 that

$$y'_0 = \frac{p_y}{p_z} = \frac{y_s}{d}. \quad (4.18)$$

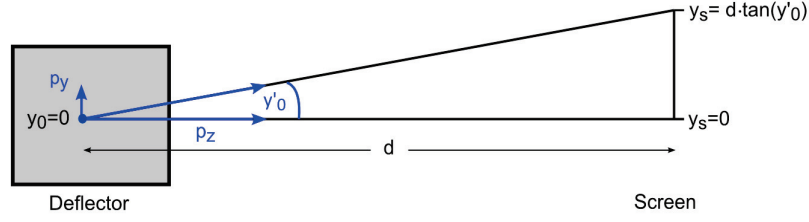


Figure 4.5: Geometric consideration to calculate the particle coordinate on the screen caused by the deflector.

Alternatively, the angle can be expressed as the ratio of transverse beam energy E_y and the energy E_z in longitudinal direction

$$y'_0 = \frac{E_y}{E_z} = \frac{e \Delta V_y}{\beta c p_z}. \quad (4.19)$$

The coordinate y_s and the beam size $\sigma_{y,s}$ on the screen are then given by

$$y_s = \Delta V_y \frac{d e}{\beta c p_z} \quad (4.20)$$

$$\Rightarrow \sigma_{y,s} = \Delta V_y(\sigma_z) \frac{d e}{\beta c p_z}. \quad (4.21)$$

$V_y(\sigma_z)$ refers to the voltage seen by a particle at longitudinal position of $\Delta z = \sigma_z$ and σ_z is the length of the bunch. Using Eq. (4.17) gives the coordinate and the resulting beam size on the screen as a function of the peak deflecting voltage

$$y_s = V_{y,0} \frac{2\pi \Delta z}{\beta^2 \lambda} \frac{d e}{c p_z} \quad (4.22)$$

$$\Rightarrow \sigma_{y,s} = V_{y,0} \frac{2\pi \sigma_z}{\beta^2 \lambda} \frac{d e}{c p_z}. \quad (4.23)$$

4.4 Technique to measure the slice energy spread

Commonly, one uses a spectrometer magnet and screen combination to measure the dispersed beam size of the entire bunch from which the projected energy and energy spread of the beam can be determined. Similarly to the emittance, the mean energy and energy spread vary along the bunch which is a result of RF acceleration and space charge effects in longitudinal direction. The operation of SASE-FELs does not only set restrictions to the slice emittance but also to the relative energy spread of the slices [15], demonstrating the request for slice energy and slice energy spread measurements.

A combination of a deflecting cavity and a dipole magnet is used to measure the energy and energy spread as a function of the temporal coordinate within the bunch [34, 35]. The working principle of the technique is illustrated in Fig. 4.6. The TCAV transfers the longitudinal distribution into a vertical distribution as explained in Section 4.3. The spectrometer magnet following the deflector transfers the energy distribution of the beam into a horizontal distribution. A screen downstream of the spectrometer magnet is used to observe the resulting image of the beam. The y -axis corresponds to the temporal

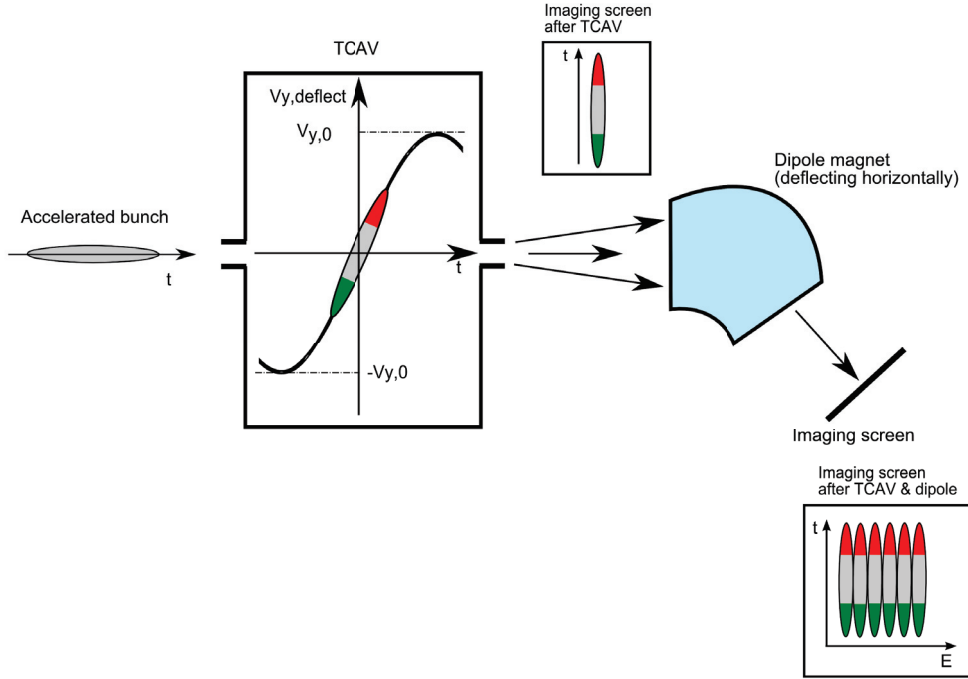


Figure 4.6: Combination of TCAV and dipole magnet to measure the slice energy spread of the beam. The deflector kicks the beam such that the longitudinal coordinate is mapped onto the vertical y -axis. The kicked beam is sent through a dipole magnet which transforms the energy coordinate to a horizontal x -coordinate on the screen.

coordinate and the x -axis to the energy coordinate. The mean energy and energy spread can be found from the mean x -coordinate and from the beam size σ_x of the individual slices.

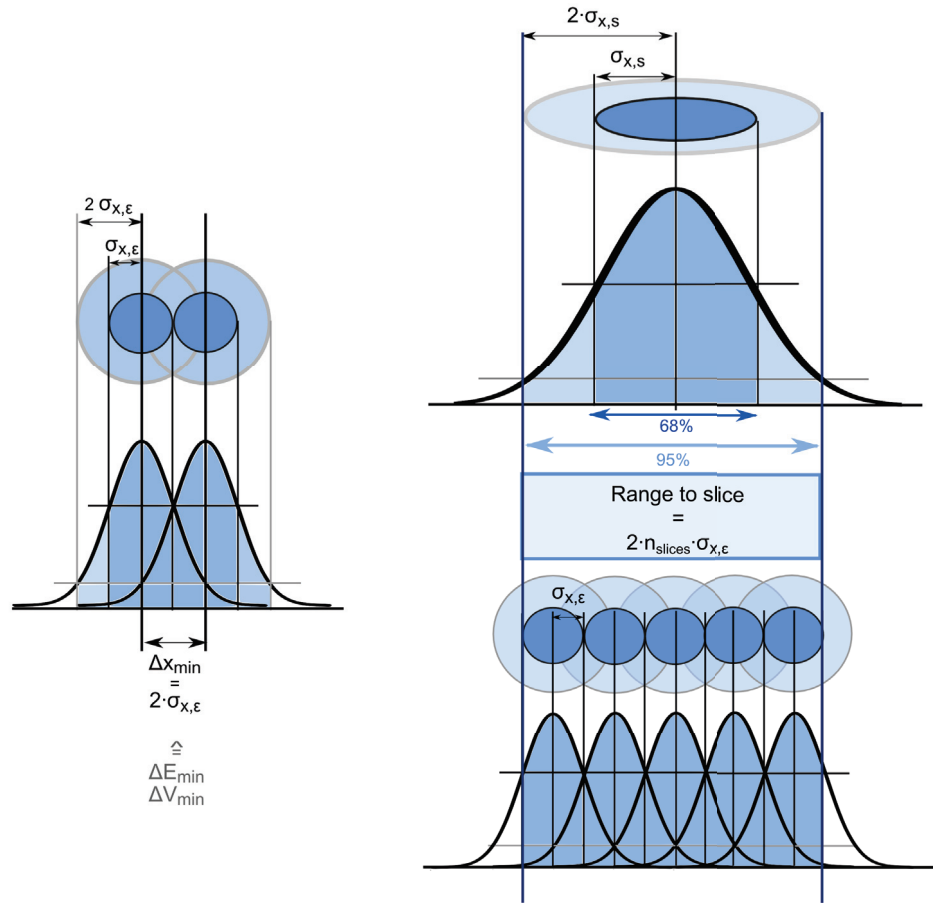
4.5 Temporal resolution criterion

The temporal resolution is an essential parameter of a slice diagnostics system. It allows to find a reasonable number of longitudinal slices to be analysed. The definition of the resolution is independent of the measurement technique applied and will be introduced in this section.

As seen from Eqs. (4.2) and (4.4), the beam size on the screen consists of the beam size from emittance and the part induced by the spectrometer magnet or deflector. It was required for $\sigma_{x,\varepsilon}$ to be much lower than the beam size induced by the technique itself for unambiguous reconstruction of the longitudinal coordinate from the screen coordinate. As a matter of fact, the contribution of $\sigma_{x,\varepsilon}$ is non-zero and therefore limiting the resolution of the system. The resolution criterion used in this work is found from the schematic illustration in Fig. 4.7a. Assuming two slices of different longitudinal positions within the bunch, these may be resolved if the difference in their centroid positions on the screen induced by the slicing technique is not less than two times the beam size from emittance, namely

$$\Delta x_{\min} = 2 \sigma_{x,\varepsilon}. \quad (4.24)$$

The distance Δx between two slices depends on the difference in energy ΔE seen by



(a) The distance between the slice centroids on the screen has to be not less than two times the beam size from emittance of a single slice in order to resolve both slices.

(b) The graphic schematically represents the beam distribution on the screen. By definition, a range of four times the beam size on the screen is used for slicing.

Figure 4.7: Definition of the resolution criterion and the range of the beam used for slicing.

different slices for the zero-phasing technique or on the difference in deflecting voltage ΔV_y for the deflector respectively. These in turn depend on the temporal coordinate of the slices within the bunch such that the spatial resolution criterion can be directly translated into a temporal resolution. To estimate the maximum number of slices to be analysed within the resolution criterion, a range of the beam image on the screen that is used for slicing has to be determined. A $\pm 2 \sigma_{x,s}$ -range corresponding to 95% of the electrons was chosen to be appropriate. The definition of the slicing range is schematically presented in the upper part of Fig. 4.7b. The $\pm 2 \sigma_{x,s}$ -range corresponds to the chosen number of slices according to $4 \sigma_{x,s} = n_{\text{slices}} \cdot 2 \sigma_{x,\epsilon}$. In the example, five slices are indicated with the resolution requirement fulfilled for adjacent slices. The number of slices depends on the beam size on the screen and the beam size from emittance according to

$$n_{\text{slices}} = \frac{4 \sigma_{x,s}}{2 \sigma_{x,\epsilon}} = \frac{4 \sigma_{x,s}}{\Delta x_{\min}}, \quad (4.25)$$

stating the demand to maximise the total beam size on the screen while maintaining as small as possible beam size contributions from emittance. Minimisation of $\sigma_{x,\epsilon}$ can be

achieved in various ways, e.g by imaging of an entrance slit. Estimations of the temporal resolution for the zero-phasing technique and the deflector technique under measurement conditions can be found in Sections 5.1.1 and 5.2.1.

5 Slice emittance measurements

Measurements were performed within this thesis, applying the two techniques to investigate the slice emittance introduced in Chapter 4. The zero-phasing technique is implemented at the ELBE SRF-injector and the corresponding measurements are described in Section 5.1. Measurements using the deflector technique took place at the PEGASUS photoinjector and are described in Section 5.2. Both examples are examined with regard to their setup, the procedure of data taking and data analysis and results.

5.1 The zero-phasing technique at ELBE

The linear accelerator ELBE delivers high-brightness electron bunches to multiple user stations including two IR-FEL oscillators [2]. In the framework of an upgrade program, the current thermionic injector is being replaced by a SRF-photoinjector [36, 37]. The SRF-injector promises higher beam brightness especially required for future experiments using high power laser radiation. Moreover, it is a test bench for the application of SRF-technology in electron injectors [38].

The heart of the SRF-injector is a 3.5-cell 1.3 GHz niobium cavity combined with a Cs₂Te-cathode illuminated by a 263 nm photocathode laser. The cw injector of 13 MHz repetition rate is designed to deliver a high-energy and medium average-current beam of low emittance and variable bunch charge. Two main operation regimes are distinguished, the ‘ELBE mode’ for FEL-operation and the ‘High-charge mode’ to produce pulsed secondary particle beams. An overview of the beam parameters for the modes is given in Tab. 5.1 [39]. The injector cavity currently implemented limits the injector performance since the design value of the accelerating gradient can not be reached due to a scratch in its back wall. The beam parameters are expected to be improved after installation of a new cavity. The parameters for the present as well as for the new cavity are listed in Tab. 5.1.

Table 5.1: Parameters of the ELBE SRF-photoinjector for the ‘ELBE operation mode’ and the ‘High-charge mode’, both for the current and the planned high-gradient injector cavity. The beam energy, gradient and emittance given for the present cavity are measured values, all others are design values.

Parameter	Present cavity		New cavity	
	ELBE	High-charge	ELBE	High-charge
Beam energy	3 MeV		< 9.5 MeV	
Peak gradient	18 MV/m		50 MV/m	
Bunch charge	77 pC	400 pC	77 pC	1 nC
Laser pulse length (rms)	1.7 ps	6.4 ps	1.7 ps	6.4 ps
Laser rep. rate	13 MHz	(2 – 250) kHz	13 MHz	≤ 500 kHz
Average current	1 mA	0.1 mA	1 mA	0.5 mA
Peak current (max.)	20 A	26 A	20 A	67 A
Norm. emittance	2 mm mrad	7.5 mm mrad	1 mm mrad	2.5 mm mrad

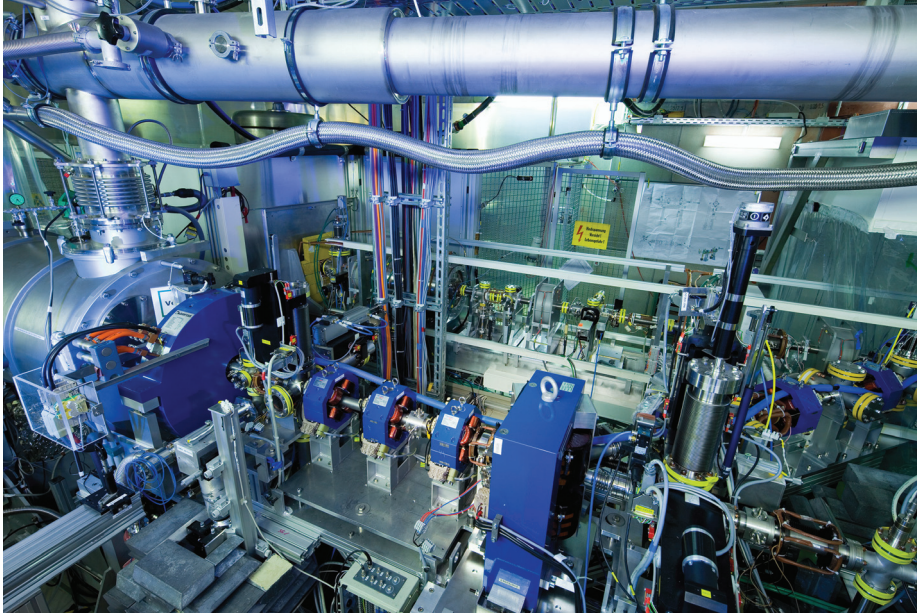


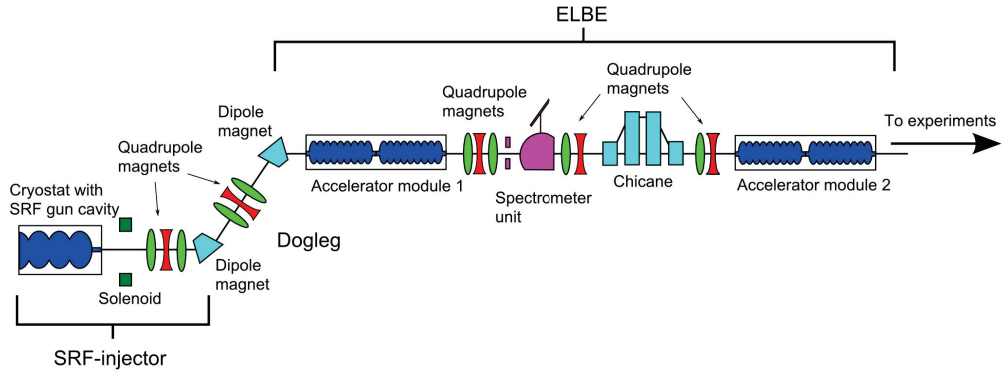
Figure 5.1: View of the ELBE SRF-photoinjector. On the left, the cryo-tank containing the superconducting injector cavity can be seen. It is followed by a solenoid, a first diagnostic station containing a screen and a Faraday-cup and a triplet of quadrupole magnets. A dipole magnet as the first element of the dogleg-beamline deflects the beam to allow injection into the ELBE beamline is visible in the background of the photograph. A diagnostics beamline is set up in forward direction of the injector.

During the commissioning phase, the SRF-injector was running in parallel to the thermionic injector. After installation of an injection beamline (dogleg) in winter 2009/2010 [40], beam from the SRF-injector can now be injected into the ELBE linac. A view of the SRF-injector including the cryo-tank, the focusing solenoid and the triplet of quadrupole magnets is presented in Fig. 5.1. The dogleg for injection of the beam into ELBE can be partly seen on the right side.

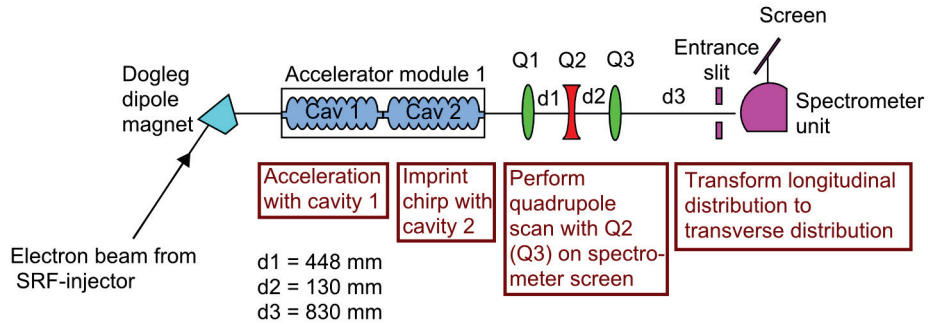
Detailed characterisation of the electron beam quality delivered by the new electron injector includes vertical slice emittance measurements in addition to measurements of the projected emittance. The following sections describe the zero-phasing measurements at ELBE. The experimental setup, the results of measurements as well as the simulations of the measurement procedure are discussed.

5.1.1 Measurement setup

The setup is described with emphasis on the spectrometer unit and possible installation positions of the spectrometer. Fig. 5.2 shows the setup of the ELBE beamline including the SRF-injector and the injection beamline to ELBE schematically. It summarises the components used for the measurement and their purpose. The ELBE accelerator consists of two accelerating modules equipped with two cavities. The first cavity of the first accelerator module is used for acceleration and is optimised for maximum energy and minimum energy spread. The second cavity is operated largely off-crest in order to create the required time-momentum correlation. To complete the zero-phasing measurement setup, the ELBE beamline has been upgraded by a special spectrometer magnet, namely a ‘Browne-Buechner’ spectrometer. The spectrometer magnet is placed in a straight section



(a) Overview of the beamline including SRF-injector and ELBE.



(b) Detailed view of components used for the measurement.

Figure 5.2: Schematic view of the setup for zero-phasing measurements at ELBE.

downstream of the accelerator module and the triplet of quadrupole magnets. The second and third quadrupole magnet of this triplet were used to perform the quadrupole scan.

‘Browne-Buechner’ spectrometer magnet

The ‘Browne-Buechner’ spectrometer [41, 42] is a dipole magnet having a uniform magnetic field with a circular boundary of radius ρ_0 and a deflecting angle for reference energy particles of 90° . Fig. 5.3 shows the imaging properties of the ‘Browne-Buechner’ spectrometer schematically. A point source, when placed at a distance ρ_0 from the boundary of the field, is focused onto a hyperbolic surface. The focal surface can be approximated by a plane suspended at an angle of $\alpha = 26.6^\circ$ [43] with respect to the reference orbit. Reference energy particles are focused with a focal length equal to ρ_0 . The exact positions for different energies in the focal plane are determined by Barber’s rule [44]. It states that the point source, its images and the centre of the corresponding central trajectory are collinear for all energies, see Fig. 5.3. Practically, the point source Q is approximated by a horizontal entrance slit. The location of the slit is referred to as the ‘slit plane’ in the following.

Energy resolution of the spectrometer The beam size on the spectrometer screen plane is determined by the beam size from emittance at the screen and a dispersive term, as introduced in Eq. (4.2). Including only first order dispersion, the beam size on the

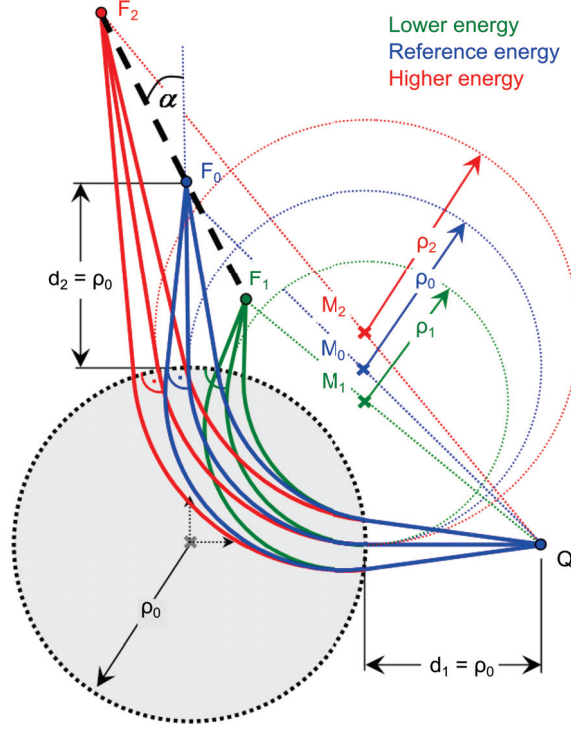


Figure 5.3: Schematic drawing of the imaging properties of the ‘Browne-Buechner’ spectrometer. Q is the point source, F_0 , F_1 , F_2 are the energy dependent images of Q (foci) and M_0 , M_1 , M_2 are the centres of the circular trajectories described by the particles in the magnetic field. ρ_0 , ρ_1 and ρ_2 are the radii corresponding to these circles. The colour code as well as the indices mark the different energies. Blue and index ‘0’ refer to the reference energy, green and index ‘1’ to a lower energy and red and index ‘2’ to a higher energy.

screen can be calculated by

$$\sigma_{x,s} = \sqrt{\sigma_{x,\varepsilon}^2 + \left(\eta_x \frac{\sigma_p}{p_0}\right)^2}. \quad (5.1)$$

According to the location of the focal plane, see Fig. 5.3, the spectrometer screen is tilted by 26.6° with respect to the reference orbit. A magnification factor of $\sqrt{5}$ has to be added to Eq. (5.1) to account for the tilt. The following considerations refer to a beam energy of 18 MeV. Hence, the simplification $\sigma_p/p_0 = \sigma_E/E_0$ is valid and will be used from here on. A resolution criterion was introduced in Fig. 4.7a of Section 4.5. The minimum distance Δx_{\min} on the screen given by Eq. (4.24) corresponds to a minimum difference in energy

$$\Delta x_{\min} = \eta_x \frac{\Delta E_{\min}}{E_0} = 2 \sigma_{x,\varepsilon} \quad (5.2)$$

$$\Rightarrow \Delta E_{\min} = 2 \frac{\sigma_{x,\varepsilon} E_0}{\eta_x}. \quad (5.3)$$

ΔE_{\min} is called the energy resolution of the spectrometer which should be as low as possible.

Energy resolution and imaging properties of the spectrometer unit The imaging properties of the so-called symmetric spectrometer setup for a point source was

introduced in Fig. 5.3. The symmetric setup is characterised by $d_1 = d_2 = \rho$ where d_1 is the distance between the slit plane and the entrance of the spectrometer, d_2 the drift length between the exit of the spectrometer and the observation (screen) plane and $\rho = \rho_0$ is the deflecting radius for reference energy particles. Since an ideal point source can not be realised, it is reasonable to consider the influence of the source characteristic on the energy resolution. In addition, the effect of diverging drift lengths d_1 and d_2 on the resolution is investigated in order to understand the special properties of the symmetric setup.

As can be seen from Eq. (5.3), the energy resolution depends on the emittance dependent beam size and the dispersion in the observation plane. Both parameters can be determined by their corresponding values at the start of the beamline and their transformation through the spectrometer unit. Subsequently, the matrix formalism [9, 10] is used to derive expressions for the beam size and the dispersion in the observation plane. Both depend on the initial beam size, the divergence and the drift lengths. The considerations include first order effects only and are limited to reference energy particles. Moreover, the investigation has to be restricted to a plane perpendicular to the reference orbit due to limitations of the matrix formalism. In this case, Eq. (5.1) simplifies to $\sigma_{x,s} = \sigma_{x,\varepsilon}$ and the energy resolution can be calculated directly from the beam size on the screen.

The transfer matrix for a drift of length d was introduced in Eq. (3.6). The ‘Browne-Buechner’ spectrometer is described in a simplified way as a sector magnet with the edge of the magnetic field perpendicular to the reference orbit. The corresponding 2×2 -matrix is given by

$$M_{\text{dipole}} = \begin{bmatrix} \cos\left(\frac{s}{\rho}\right) & \rho \sin\left(\frac{s}{\rho}\right) \\ -\frac{1}{\rho} \sin\left(\frac{s}{\rho}\right) & \cos\left(\frac{s}{\rho}\right) \end{bmatrix}, \quad (5.4)$$

where, s is the arc length within the dipole magnet. The analysed spectrometer unit is composed of a drift d_1 upstream of the spectrometer magnet, the 90° -spectrometer magnet of radius $\rho = 0.2$ m and a drift d_2 . The total transfer matrix for the unit is the product of the single transfer matrices $M_{\text{total}} = M_{d,2} \cdot M_{\text{dipole},90^\circ} \cdot M_{d,1}$. The matrix $M_{\text{dipole},90^\circ}$ can be derived from Eq. (5.4). For a deflection of 90° , s is a quarter of the full circle circumference $\rho s = 2\pi\rho/4$ and s/ρ is found to be $\pi/2$, simplifying the matrix to

$$M_{\text{dipole},90^\circ} = \begin{bmatrix} 0 & \rho \\ -\frac{1}{\rho} & 0 \end{bmatrix}. \quad (5.5)$$

The transformation of the σ -matrix through the beamline was introduced in Eq. (3.1). The element $\sigma_{11}(s)$ is found to be

$$\begin{aligned} \sigma_{11}(s) = & \frac{d_1^2 d_2^2 \sigma_{22}(0) + 2 d_1 d_2^2 \sigma_{12}(0) - 2 d_1 d_2 \rho^2 \sigma_{22}(0) + d_2^2 \sigma_{11}(0)}{\rho^2} \\ & + \frac{-2 d_2 \rho^2 \sigma_{12}(0) + \rho^4 \sigma_{22}(0)}{\rho^2}. \end{aligned} \quad (5.6)$$

Assuming a point source characterised by $\sigma_{x,0} = 0$ and a parallel source given by $\sigma_{x',0} = 0$,

the beam size in the screen plane $\sigma_{x,s} = \sqrt{\sigma_{11}(s)}$ simplifies to

$$\sigma_{x,s} = \frac{\sigma_{x',0} (d_1 d_2 - \rho^2)}{\rho} \quad \text{for a point source} \quad (5.7)$$

$$\sigma_{x,s} = \frac{d_2 \sigma_{x,0}}{\rho} \quad \text{for a parallel source.} \quad (5.8)$$

The dispersion function from a start position $s = 0$ to the spectrometer screen transforms as follows

$$\begin{bmatrix} \eta_{x,s} \\ \eta'_{x,s} \end{bmatrix} = M_{\text{total}} \cdot \begin{bmatrix} \eta_{x,0} \\ \eta'_{x,0} \end{bmatrix}. \quad (5.9)$$

The dispersion at the screen is then given by

$$\eta_{x,s} = \frac{-d_1 d_2 \eta'_{x,0} - d_2 \eta_{x,0} + d_2 \rho + \eta'_{x,0} \rho^2 + \rho^2}{\rho}. \quad (5.10)$$

Starting with zero dispersion in the slit plane $\eta_{x,0} = \eta'_{x,0} = 0$ leads to the simple relation

$$\eta_{x,s} = d_2 + \rho. \quad (5.11)$$

The relations derived for the beam size and dispersion on the screen plane, Eqs. (5.6) and (5.11), are now used to calculate the resolution as a function of the drift lengths d_1 and d_2 . A magnification factor defined as the ratio of the beam size in the screen plane and the source beam size, $\sigma_{x,s}/\sigma_{x,0}$, is introduced, permitting a simple possibility to describe the spectrometer imaging properties. Both the resolution and magnification are presented in 2D plots for varied drift lengths, yielding a ‘energy resolution map’ and a ‘magnification map’.

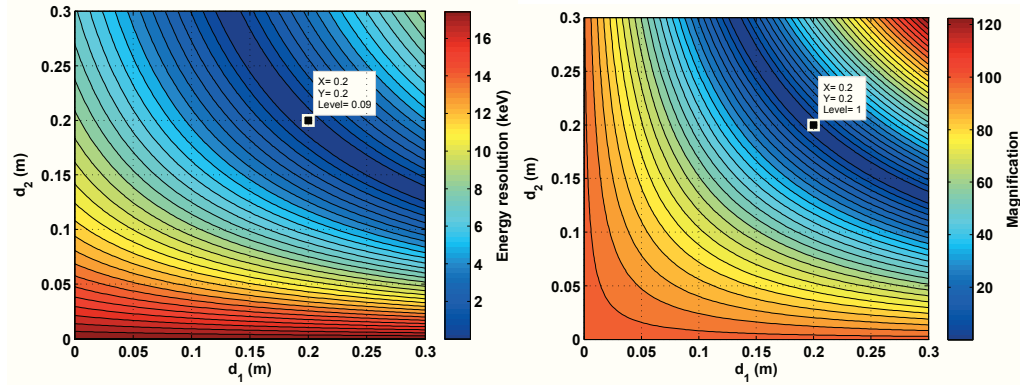
The subsequent sections discuss the characteristics of the resolution and the magnification for the point source, the parallel source and a realistic source. The presented calculations were performed using a specified spectrometer deflecting radius of $\rho = 0.2$ m.

Point source The magnification and energy resolution for a point source can be derived using Eqs. (5.3), (5.7), (5.11) and the relation $\sigma_{x,s} = \sigma_{x,\varepsilon}$, leading to

$$\frac{\sigma_{x,s}}{\sigma_{x,0}} = \frac{\sigma_{x',0} (d_1 d_2 - \rho^2)}{\rho \sigma_{x,0}} \quad (5.12)$$

$$\Delta E_{\text{min}} = \frac{2 E_0 \sigma_{x',0} (d_1 d_2 - \rho^2)}{\rho (d_2 + \rho)}. \quad (5.13)$$

The energy resolution in the screen plane depends on the initial divergence and both drift lengths d_1 and d_2 . The smallest possible ΔE_{min} in the screen plane is achieved for a focus given by $d_1 d_2 = \rho^2$. In addition, this condition causes ΔE_{min} to become independent of the initial divergence. The simplest setup to fulfil this condition is the symmetric spectrometer setup introduced in Fig. 5.3. Further analysis is performed by means of the energy resolution and magnification maps calculated from Eqs. (5.6) and (5.11). Figs. 5.4a and 5.4b represent the maps for a point source which was approximated by the initial conditions $\sigma_{x,0} = 1 \mu\text{m}$ and $\sigma_{x',0} = 500 \mu\text{rad}$. The magnification characteristic shown in Fig. 5.4b is symmetric with respect to a line defined by equal drift lengths $d_1 = d_2$. The energy resolution map is similar to the magnification map since the resolution is directly



(a) Energy resolution in keV for the point source.

(b) Magnification of the spectrometer for the point source.

Figure 5.4: Energy resolution and magnification of the spectrometer as a function of the drift lengths upstream (d_1) and downstream (d_2) of the spectrometer calculated from Eqs. (5.6) and (5.11). The beam size was set to $\sigma_{x,0} = 1\mu\text{m}$ and the beam divergence to $\sigma_{x',0} = 500\mu\text{rad}$ in order to approximate a point source.

proportional to the beam size in the observation plane. Furthermore, the resolution is inversely proportional to the dispersion in the screen plane. Since the dispersion was shown to increase linearly with d_2 , see Eq. (5.11), this induces a deviation from symmetry. One observes a band of low magnification and low ΔE_{\min} for $d_1 d_2 = \rho^2$. Point-to-point imaging occurs for this special setting proving the properties of the setup as discussed in Fig. 5.3. The included mark displays the resolution and magnification value for the position with both drift lengths $d_1 = d_2 = \rho = 0.2\text{m}$. As expected the magnification factor is equal to one and the energy resolution is 0.09 keV.

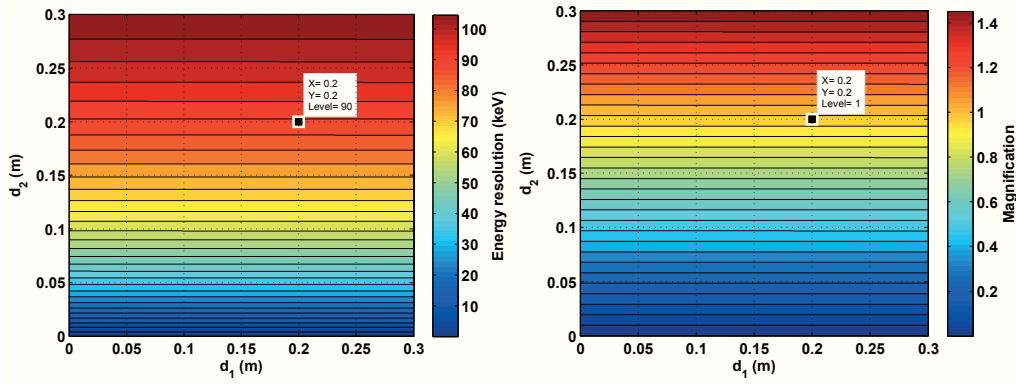
Parallel source The energy resolution and magnification for the parallel source are given by

$$\frac{\sigma_{x,s}}{\sigma_{x,0}} = \frac{d_2}{\rho} \quad (5.14)$$

$$\Delta E_{\min} = \frac{2 E_0 \sigma_{x,0} d_2}{\rho (d_2 + \rho)}. \quad (5.15)$$

The energy resolution in the screen plane essentially depends on the size of the source in the slit plane and is proportional to the magnification. Both the energy resolution and the magnification are independent of the distance d_1 and increase with the distance downstream of the spectrometer. The minimum of ΔE_{\min} and of the magnification (focal point) is located directly at the spectrometer exit. An observation plane in a distance $d_2 = \rho$ yields 1:1-imaging.

The resolution and magnification maps calculated for a parallel source are presented in Figs. 5.5a and 5.5b. The source characteristic was approximated by $\sigma_{x,0} = 1\text{mm}$ and $\sigma_{x',0} = 1\mu\text{rad}$. As expected from Eq. (5.14), the magnification factor is equal to one for $d_2 = \rho$ and decreases towards the spectrometer exit plane. The energy resolution map shows similar behaviour. ΔE_{\min} for the symmetric setup is 90 keV, as can be seen from the included mark. This increase of the energy resolution mirrors the factor of 1,000 in the beam size of the parallel source compared to the point source.



(a) Energy resolution in keV for the parallel source.

(b) Magnification of the spectrometer for the parallel source.

Figure 5.5: Energy resolution and magnification of the spectrometer as a function of the drift lengths upstream (d_1) and downstream (d_2) of the spectrometer calculated from Eqs. (5.6) and (5.11). The beam size was set to $\sigma_{x,0} = 1$ mm and the beam divergence to $\sigma_{x',0} = 1$ μ rad in order to simulate a parallel source.

A schematic visualisation of a parallel beam entering the spectrometer is presented in Fig. 5.6. The setup is identical to Fig. 5.3 but the location of the focal plane is shifted towards the spectrometer exit plane due to the parallel source.

Conclusion for ideal sources It was shown that the energy resolution and the magnification of the spectrometer setup depend on the properties of the setup as well as of the sources under consideration.

The properties of the point source are:

- An entrance slit of adjustable width can be used to confine the entrance beam size.
- The energy resolution is controlled by the width of the slit and the lowest ΔE_{\min} is determined by the minimum achievable slit size.
- The optimum resolution is achieved in a focal plane given by $d_2 = \rho$, making the setup realisable from the constructional point of view.

The parallel source in distance $d_1 = \rho$ is characterised by:

- Adjusting the source is challenging and requires to control the divergence.
- The divergence varies during the measurement procedure, leading to a shifted resolution plane. Hence, maintaining a constant energy resolution is hardly achievable.
- The optimum resolution is achieved at $d_2 = 0$ and can not be realised in a realistic setup.
- For any $d_2 > 0$, the beam size is enlarged at the screen, see Eq. (5.8), and the resolution is not optimal.

In conclusion, a symmetric spectrometer unit combined with a point source has essential benefit compared to different setups, namely an accessible area of low and exactly defined energy resolution.

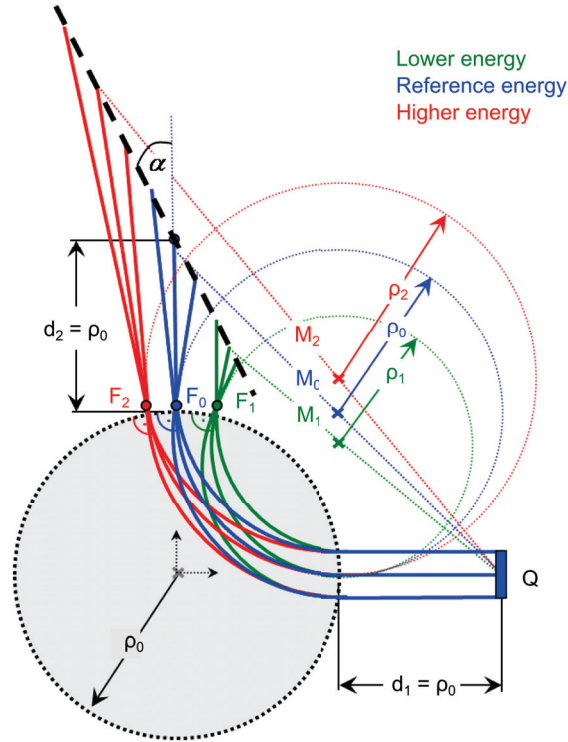


Figure 5.6: Imaging properties of the ‘Browne-Buechner’ spectrometer for a parallel source. Images of the source Q are observed in the focal plane defined by the imaging of the point source, see Fig. 5.3. The position of the focal points is shifted towards the exit of the spectrometer magnet.

Realistic source In order to show that the symmetric spectrometer setup is suitable for measurement conditions as well, the resolution and magnification maps are calculated for realistic beam sizes and divergences. Two sets of realistic source parameters were investigated. Firstly, calculations were performed assuming the spectrometer entrance slit to be opened to a full width $FW_{\text{slit}} = 20 \text{ mm}$, in which case the resolution is determined by the beam size in the spectrometer slit plane. Average beam size and divergence values $\sigma_{x,0} = 400 \mu\text{m}$ and $\sigma_{x',0} = 350 \mu\text{rad}$ were found from simulations of the measurements. The energy resolution and magnification characteristics for the open slit case can be seen in Figs. 5.7a and 5.7b. The resolution was calculated to 36 keV for the symmetric setup and the energy resolution generally decreases for a plane that is located closer to the spectrometer exit. Obviously, these source parameters provide a resolution characteristic most comparable to that of a parallel source and therefore do not allow to fully benefit from the spectrometer properties.

Secondly, a setting using the minimum size of the adjustable entrance slit width [43] was calculated. The rms-value of a hard-edge distribution having a full width FW can be shown to be $\sigma_{\text{hard-edge}} = FW_{\text{hard-edge}}/\sqrt{12}$ using the integral form of the rms-definition. The entrance slit of $100 \mu\text{m}$ full width corresponds to a beam size of $\sigma_{x,0} = 100 \mu\text{m}/\sqrt{12} = 29 \mu\text{m}$. The simulated average divergence for this setting is $70 \mu\text{rad}$. The divergence is smaller than for the open-slit setting. A correlation between the beam size and divergence ($\alpha \neq 0$) in the slit plane causes the slit to change both parameters simultaneously. The calculated resolution and magnification maps can be found in Figs. 5.7d and 5.7c. The maps clearly mirror the property of the source which is much closer to a point source.

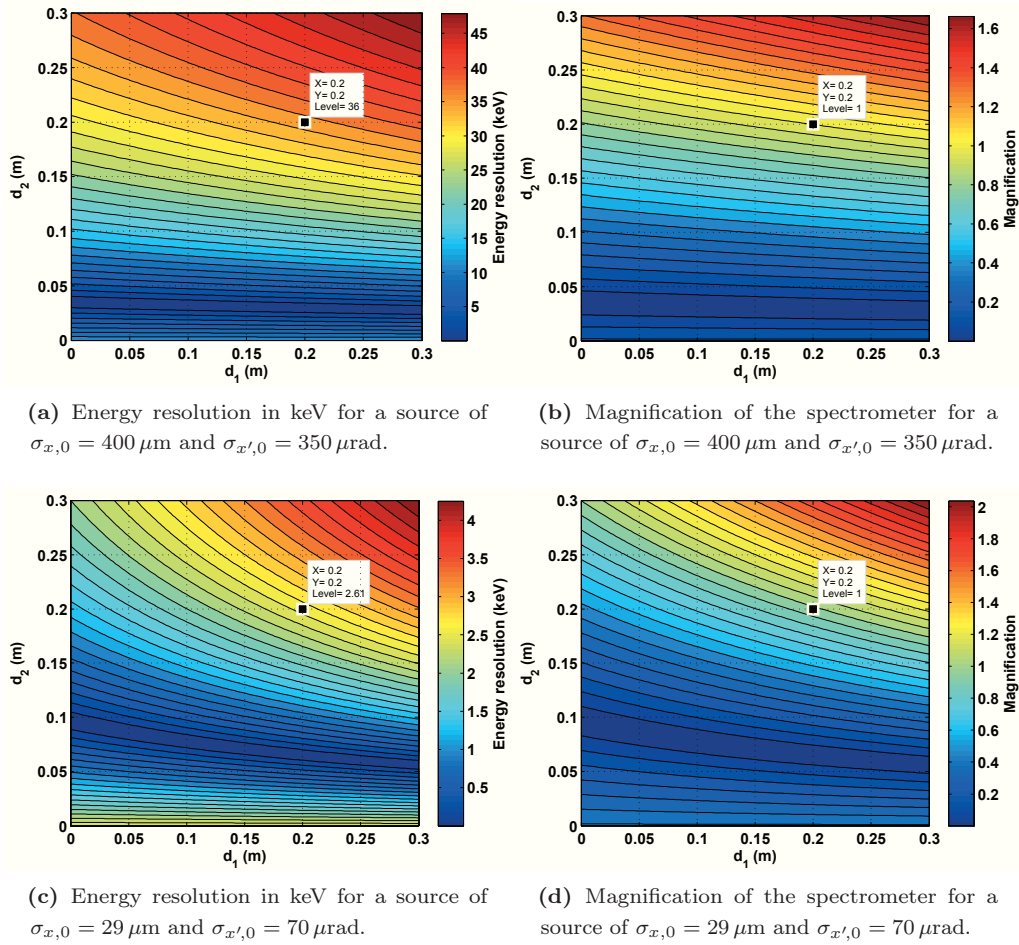
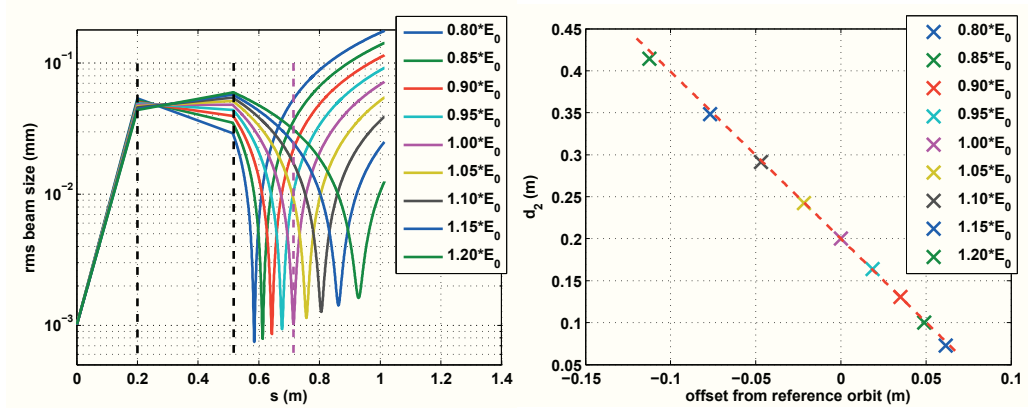


Figure 5.7: Energy resolution and magnification of the spectrometer as a function of the drift lengths upstream (d_1) and downstream (d_2) of the spectrometer calculated from Eqs. (5.6) and (5.11). The calculations were performed for realistic conditions during the measurement.

Anyhow, the observed characteristic is a mixture of both limiting cases. The band of low energy resolution does not show the symmetry observed in Fig. 5.4a. For a distance $d_1 = 0.2 \text{ m}$, the lowest ΔE_{\min} is achieved at $d_2 = 0.07 \text{ m}$ (darkblue). The energy resolution of the symmetric setup $d_1 = d_2 = 0.2 \text{ m}$ was estimated to 2.6 keV . The reduction of the entrance slit width leads to a decrease in ΔE_{\min} compared to the open-slit setting by a factor of 14. The magnification is largely independent of the slit setting, compare Fig. 5.7.

Simulation of the focal plane It was previously shown that 1:1-imaging occurs for reference energy particles in a plane given by a distance $d_2 = r$ perpendicular to the reference orbit. Non-reference energy particles have not been considered up to now. This section briefly investigates the imaging properties for particles with energy deviation using an ELEGANT simulation [45].

A beamline of 1 m total length was used. The beamline consists of a drift $d_1 = 0.2 \text{ m}$ upstream of the spectrometer magnet, the spectrometer magnet and a drift section d_2 downstream of the spectrometer which was finely subdivided. It was mandatory to take



(a) Evolution of the rms beam size σ_x along the spectrometer beamline for different energies. The black dashed lines indicate the spectrometer entrance and exit, the dashed magenta line stands for the focal plane for reference energy.

(b) Reconstructed focal plane. The dashed red line shows the location of the theoretical focal plane.

Figure 5.8: Simulation of the spectrometer imaging properties for varied beam energy. The beam size of the source was set to $\sigma_{x,0} = 1 \mu\text{m}$ and the divergence was $\sigma_{x',0} = 0.3 \text{ mrad}$. Second order effects were included.

into account the curved field boundary and second order effects for the simulation of the imaging properties of the spectrometer. A mono-energetic beam of reference energy and initial parameters $\sigma_{x,0} = 1 \mu\text{m}$, $\sigma_{x',0} = 0.3 \text{ mrad}$ (approximated point source) and a normalised emittance of 1 mm mrad was tracked through the beamline. The calculation was repeated for mono-energetic beams with energies deviating from the reference energy by up to $\pm 20\%$. The results of the simulation are presented in Fig. 5.8. The evolution of the beam size along the beamline is depicted in Fig. 5.8a. The minimum in beam size indicates the position of the focus for each beam energy. The vertical lines indicate the spectrometer entrance and exit plane (black, dashed) and the theoretically expected focal distance for reference energy (magenta, dashed). The position of the minimal beam size depends on the beam energy and moves away from the exit plane with increasing energy. 1:1-imaging is observed for reference energy particles. Higher energies lead to a slightly higher magnification factor while lower energies reduce the magnification. Since the simulated source is no ideal point source, this behaviour is in accordance with the schematic drawing in Fig. 5.6, which revealed an increased image size with increased energy. The combination of the focal distances and the transverse offset of the beam centre at the focal distance determined from the simulation allows to reconstruct the focal plane as presented in Fig. 5.8b. The theoretical focal plane rotated by 26.6° with respect to the reference orbit is drawn as a red dashed line for comparison. Both the simulated and the theoretical plane are identical for small energy deviations. Reference energy particles are focused in a distance $d_2 = \rho = 0.2 \text{ m}$ and the theoretical predictions are verified. A slight variation between both planes occurs for larger energy deviations since the realistic focal surface is hyperbolic. This influence is assumed to be small for the energy deviations well below $\pm 5\%$ expected during the measurement.

Temporal resolution for realistic measurement settings The knowledge of the energy resolution of the spectrometer unit as well as the induced energy chirp of the

electron bunch finally allows to estimate the temporal resolution of the setup. From there, the maximum number of slices to be analysed for a given bunch length can be found. The estimation was performed for measurement conditions.

First, the general limitation of the resolution by the screen size was estimated using Eq. (5.1). Neglecting $\sigma_{x,\varepsilon}$ and rearranging gives the expression

$$\Delta E_{s,\max} = \frac{\Delta x_s}{\eta_x} \quad (5.16)$$

for the energy acceptance of the screen. Here, Δx_s is the geometric size of the screen transformed to a plane perpendicular to the reference orbit, which is equal to $45 \text{ mm}/\sqrt{5}$ [46]. The energy acceptance of the screen was estimated knowing $\eta_x = 0.4 \text{ m}$ to $\Delta E_{s,\max} = \pm 2.5 \%$. This corresponds to an absolute value of $\pm 450 \text{ keV}$. The maximum number of slices fitting on the screen is given by $n_{\text{slices}} = \Delta E_{s,\max}/\Delta E_{\min}$. A spectrometer unit with an entrance slit closed to minimum width allows to analyse up to ~ 350 slices within the resolution of 2.6 keV . The number of slices decreases for an energy resolution which is limited by the beam size of $400 \mu\text{m}$ (entrance slit 20 mm full width). Here, a resolution of 36 keV was estimated in the previous section, limiting the number of slices to 25.

The rms energy spread σ_E actually induced to the bunch during the measurement can be estimated from the energy E gained in the cavity. The energy gain depends on the effective peak accelerating voltage $V_{0,\text{eff}}$ and is given by

$$E = e V = e V_{0,\text{eff}} \sin(\omega t + \varphi). \quad (5.17)$$

Taking the temporal derivative dE/dt and rearranging leads to

$$\Delta E = \Delta t \cdot \omega e V_{0,\text{eff}} \cos \varphi \quad (5.18)$$

for $t = 0$. The rms energy spread is then found using $\Delta E = \sigma_E$ and $\Delta t = \sigma_t$

$$\sigma_E = \sigma_t \cdot \omega e V_{0,\text{eff}} \cos \varphi, \quad (5.19)$$

where σ_t is the rms bunch length. The possible number of slices to be analysed can be calculated from Eq. (4.25). Eq. (5.2) yields $\sigma_{x,s} = \eta_x \sigma_E/E_0$ and $\Delta x_{\min} = \eta_x \Delta E_{\min}/E_0$, such that the number of slices can be expressed as

$$n_{\text{slices}} = \frac{4 \sigma_E}{\Delta E_{\min}}. \quad (5.20)$$

The temporal resolution Δt_{\min} achieved for measurement settings can be calculated from Eq. (5.18) by setting $\Delta E = \Delta E_{\min}$

$$\Delta t_{\min} = \frac{\Delta E_{\min}}{\omega e V_{0,\text{eff}} \cos \varphi}. \quad (5.21)$$

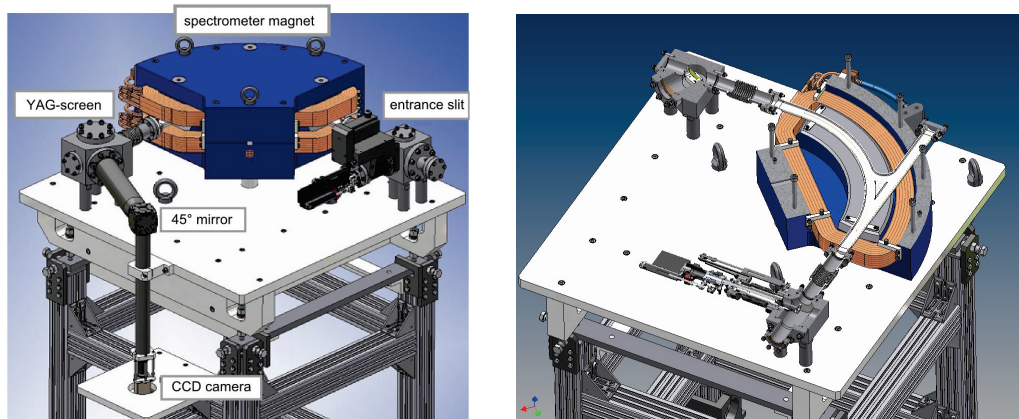
ΔE_{\min} is the energy resolution estimated for measurement conditions. The temporal resolution and the corresponding number of slices for different settings are summarised in Tab. 5.2. $V_{0,\text{eff}}$ and the phases are real settings, the bunch lengths were found from simulations. For detailed information on the measurements and the simulations see Section 5.1.2. The results in Tab. 5.2 underline the relevance of the beam size at the slit plane. Temporal resolutions between 80 fs and 140 fs are achievable for a beam size of $29 \mu\text{m}$. This corresponds to a maximum of 70 slices. A beam size of $400 \mu\text{m}$ leads to a

Table 5.2: Estimation of the temporal resolution under realistic measurement conditions. The temporal resolution is estimated both for the minimum slit size $\sigma_{x,0} = 29 \mu\text{m}$ and for an open slit assuming an average beam size of $\sigma_{x,0} = 400 \mu\text{m}$. The beam energy for measurements was $\sim 18 \text{ MeV}$.

Meas. series	$V_{0,\text{eff}}$ (MV)	φ ($^\circ$)	σ_t (ps)	σ_E (keV)	$\sigma_{x,0} = 29 \mu\text{m}$		$\sigma_{x,0} = 400 \mu\text{m}$	
					Δt_{min} (fs)	n_{slices}	Δt_{min} (ps)	n_{slices}
1, 2	7.4	72	2.4	45	140	69	1.9	5
3	"	114	3.4	84	106	129	1.5	9
4, 5	"	"	2.0	49	"	76	"	5
6	"	120	2.0	60	86	93	1.2	7
7 – 10	7.1	63	3.4	90	99	174	1.4	10
11	"	55	"	113	78	138	1.1	13

lower temporal resolution of (1.1 – 1.9) ps and the possible number of slices varies between five and 13. This source characteristic marks the overall limitation of the slice number. It assures the resolution criterion to be fulfilled for all measurement series. Thus, five slices were chosen for the measurement analysis, see description in Section 5.1.2.

Specifications of the implemented spectrometer unit The implemented ‘Browne-Buechner’ spectrometer [43, 46] includes an entrance slit approximating the point source, the spectrometer magnet itself and a Yttrium Aluminium Garnet (YAG)-screen placed in the focal plane. The screen image is viewed using a downwards deflecting mirror and a CCD camera. Fig. 5.9 shows different views of the spectrometer in a constructional model with the individual components of the spectrometer unit marked in Fig. 5.9a. Tab. 5.3 summarises the most important parameters of the spectrometer.



(a) Construction model of the spectrometer unit.

(b) Sectional view of the construction model of the spectrometer.

Figure 5.9: The spectrometer unit implemented at ELBE [46] consists of an entrance slit approximating the point source, the dipole magnet and a YAG-screen. The image on the screen is observed using a combination of a plane mirror and CCD-camera.

Table 5.3: Specifications of the installed ‘Browne-Buechner’ spectrometer magnet [43, 46].

Parameter	
Deflecting angle	90°
Deflecting radius	0.2 m
Distance slit to spectrometer	"
Distance spectrometer to screen	"
Adjustable slit range (full width)	(0.1 – 20) mm
Energy range	(5 – 50) MeV
Screen material	YAG
$\eta_{x,s}$ (for $\eta_{x,0} = 0$)	-0.4 m
$\eta_{2x,s}$ (for $\eta_{2x,0} = 0$)	0.2 m

Spectrometer magnet installation

Different alternatives were considered in order to find the optimum position of the spectrometer magnet in the ELBE beamline. The following section introduces the relevant possibilities and discusses proof of principle simulations that verify the chosen setup to be the most appropriate for the slice emittance measurements.

The vacuum chamber of the spectrometer magnet allows for 90° deflection of the beam or straight passage, as can be seen in Fig. 5.9b. This generally allows the spectrometer magnet to be placed directly in the ELBE main beamline. The vertical aperture of the vacuum chamber is 8 mm compared to 36 mm diameter standard for the ELBE beamline. Hence, it was considered to avoid an installation in the main beamline to prevent electrons from being scraped by the beam pipe. Especially high current operation modes were suspected to be problematic regarding radiation issues caused by beam losses. Compatibility for the installation in the ELBE beamline could only be verified or disproved by practical tests. Before installation of the spectrometer magnet for testing, different setup options with the spectrometer magnet placed in the main beamline or within an added diagnostic beamline were considered. Fig. 5.10 gives an overview of all installations that will be discussed subsequently.

Evaluation of different spectrometer magnet positions In Section 4.2, the relation $|\eta_x| \gg |\eta_{2,x}| \cdot \Delta p_{\max}/p_0$ was introduced as a criterion to be fulfilled in order to achieve a linear p - x -correlation on the spectrometer screen. Moreover, the dispersion η_x in the spectrometer slit plane is an important parameter. The dispersion is required to be zero at this position. If non-zero, the slit acts as an energy filter transmitting only a part of the beam to the screen and a simultaneous measurement of all slices is not possible. The linearity criterion as well as the requirement of $\eta_x = 0$ at the entrance slit were used to evaluate the different installations of the spectrometer magnet.

Proof of principle simulations of the measurement procedure were performed. The optical beamline was optimised for the individual setup regarding appropriate β -functions and dispersion values. Design settings of the SRF-injector and ELBE beamline were used as reference and start values. The zero-crossing phase was used to imprint a momentum chirp of $p_{\max}/p_0 \approx 15\%$. The simulations deliver the dispersion characteristic as well as the p - x -correlation in the spectrometer slit and screen plane. The representation of the dispersion function along the beamline for the most relevant setups can be found in

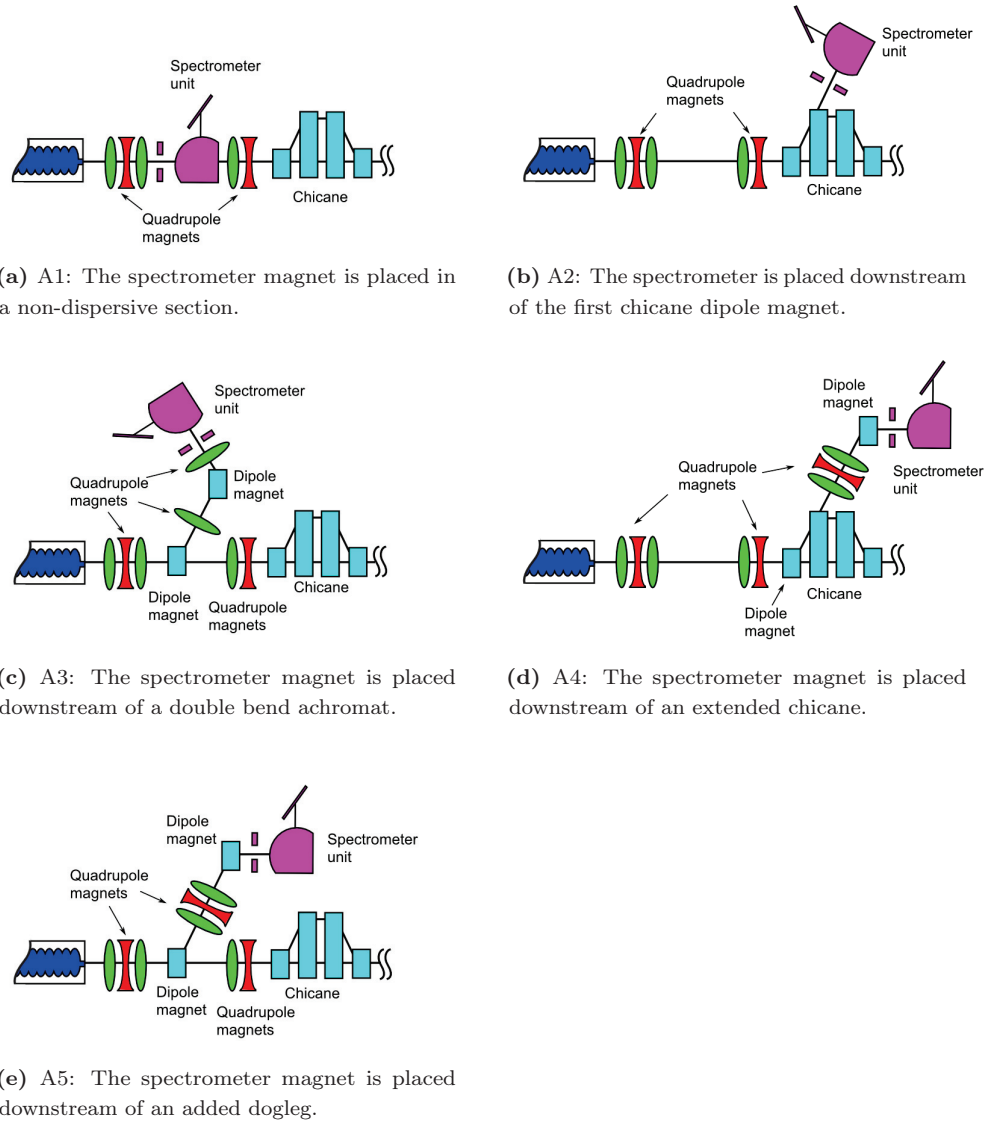


Figure 5.10: Overview of possible spectrometer magnet installations.

Appendix A. A summary of the determined dispersion values in the slit and screen plane is given in Tab. 5.4.

A1 - spectrometer installation in a non-dispersive section of the ELBE beamline Here, the spectrometer magnet is placed directly in the ELBE beamline. The magnet is positioned in the non-dispersive drift section following the triplet of quadrupole magnets downstream of the first accelerator module, as shown in Fig. 5.10a. An essential advantage of A1 is that no additional components are needed. A drawback is the incalculable influence of the small vertical aperture.

The simulated dispersion values of A1 can be seen from Tab. 5.4. Both the first and second order dispersion are zero at the spectrometer entrance slit. First order dispersion is dominating in the screen plane since $|\eta_x| \approx 13 \cdot |\eta_{2,x}| \cdot \Delta p_{\max}/p_0$. The phase space plots in Fig. 5.11 show the expected behaviour. Due to zero dispersion in the slit plane, no correlation between p and x is observed. A narrow entrance slit cuts all particle

Table 5.4: Simulated first and second order dispersion values in the slit and screen plane for the setups A1, A2 and A3. Alternatives A4 and A5 are not listed here since simulations of the measurement were not realisable with these setups, see the following paragraphs for explanation. The included maximum momentum spread of $p_{\max}/p_0 \approx 0.15$ results from the simulations using the zero-crossing phase.

	Parameter (m)	A1	A2	A3
slit plane	η_x	0.00	-0.48	7.49×10^{-3}
	$\eta_{2,x}$	0.00	0.51	0.74
	$ \eta_{2,x} \cdot \Delta p_{\max}/p_0$	0.00	0.08	0.11
screen plane	η_x	-0.40	0.08	-0.41
	$\eta_{2,x}$	0.20	-1.56	0.97
	$ \eta_{2,x} \cdot \Delta p_{\max}/p_0$	0.03	0.23	0.15

energies equally. In the screen plane, a linear p - x -correlation is observed since higher order dispersion effects are negligible, see Fig. 5.11b. A narrow entrance slit sharpens the distribution and therefore improves the resolution of the system. The setup A1 provides an optimum optical setup that meets all the requirements.

A2 - spectrometer installation downstream of the chicane Alternative A2 uses a section of the chicane as shown in Fig. 5.10b. The first dipole magnet of the chicane deflects the beam, the second dipole magnet is switched off. The spectrometer magnet is placed directly downstream of the second dipole magnet at an angle of 20° to ELBE. Setup A2 has a finite first and second order dispersion in the spectrometer slit plane that is caused by the chicane dipole magnet. Here, $|\eta_x| \approx 6 \cdot |\eta_{2,x}| \cdot \Delta p_{\max}/p_0$ and the first order dispersion is dominating which results in an almost linear p - x -correlation at the slit, as can be seen in Fig. 5.12a. The requirement of zero dispersion in the slit plane is not fulfilled. An entrance slit leads to energy filtering, impeding single-shot measurements of all slices. Since the slit is essential to perform high resolution measurements, the setup already proves to be not appropriate. Anyhow, the simulated correlation in the

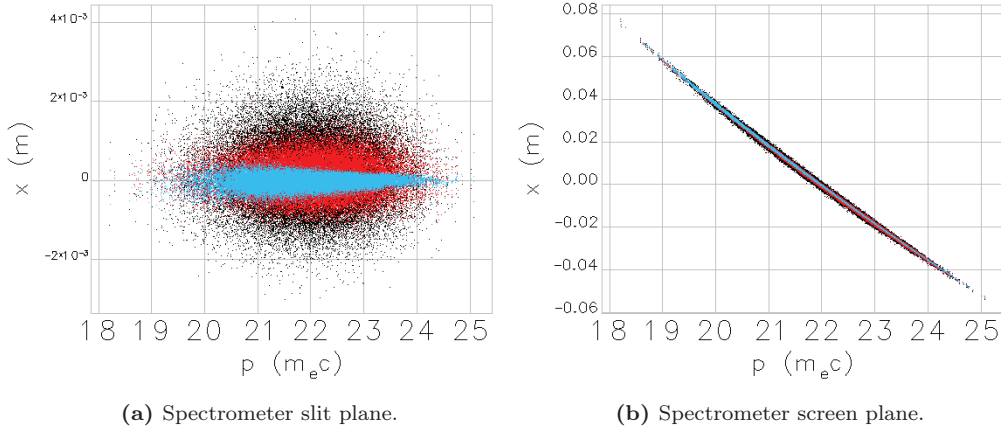


Figure 5.11: Simulated p - x correlations for setup A1. The red, blue and black colours indicate different settings of the quadrupole magnet during the scan.

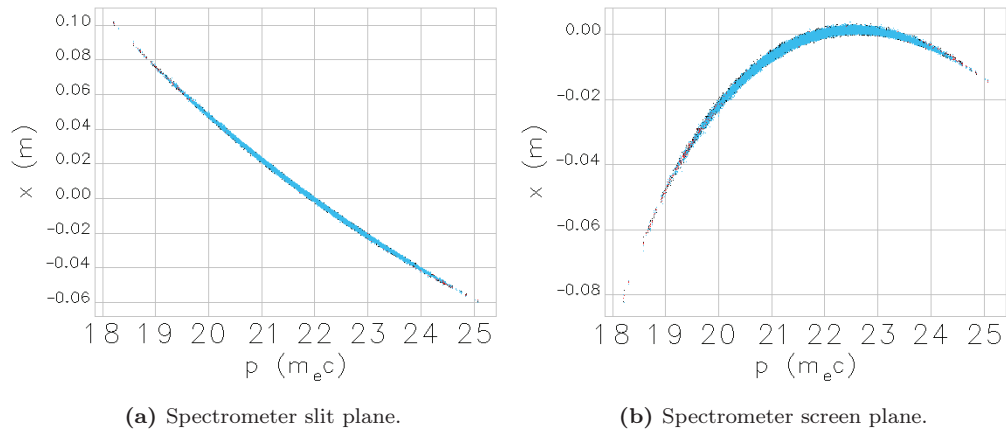


Figure 5.12: Simulated p - x -correlations for the setup A2. The red, blue and black colours indicate different settings of the quadrupole magnet during the scan.

screen plane will be considered briefly. The dispersion requirement is not fulfilled since $|\eta_x| \approx 0.3 \cdot |\eta_{2,x}| \cdot \Delta p_{\max}/p_0$. Non-linear effects are predominating, as mirrors in the p - x -correlation in Fig. 5.12b. Different screen coordinates correspond to the same momentum and the reconstruction of the longitudinal position is unambiguous, making the setup unsuitable for the measurements.

A3 - spectrometer installation downstream of an added double-bend achromat The beam is deflected off the main beamline using a double-bend achromat. The spectrometer magnet is placed downstream of the second dipole magnet, as can be seen from Fig. 5.10e.

For A3, a dominating second order dispersion in the slit plane $|\eta_x| \approx 0.07 \cdot |\eta_{2,x}| \cdot \Delta p_{\max}/p_0$ is found from simulation, which can be seen from Fig. 5.13a. As discussed for A2, the entrance slit acts like an energy filter and non-suitability for the measurement is proved. The dispersion relation in the screen plane is $|\eta_x| \approx 3 \cdot |\eta_{2,x}| \cdot \Delta p_{\max}/p_0$. First order effects are slightly dominating but non-linearities can still be observed in Fig. 5.13b. Thus, A3 is, similar to A2, not suitable for slice emittance measurements.

A4 - spectrometer installation in extended chicane Alternative A4 uses a section of the chicane, as presented in Fig. 5.10d. The first dipole magnet of the chicane deflects the beam, the second dipole magnet is switched off. A triplet of quadrupole magnets and a dipole magnet are added to form a second dogleg and the spectrometer magnet is placed downstream of the second chicane dipole magnet.

Beamline modelling of the setup A4 proved to be problematic. The optimisation of the beamline did not allow for a closed dispersion downstream of the added dogleg. A symmetric magnet setting that usually simplifies dispersion modelling could not be implemented due to the long drift section between the dipole magnets of the chicane and limited space in the accelerator tunnel. Hence, this installation was rejected.

A5 - spectrometer installation downstream of an additional dogleg The alternative A5 uses an additional dogleg installed in a non-dispersive beamline section to deflect the beam off the ELBE beamline. The spectrometer magnet is placed

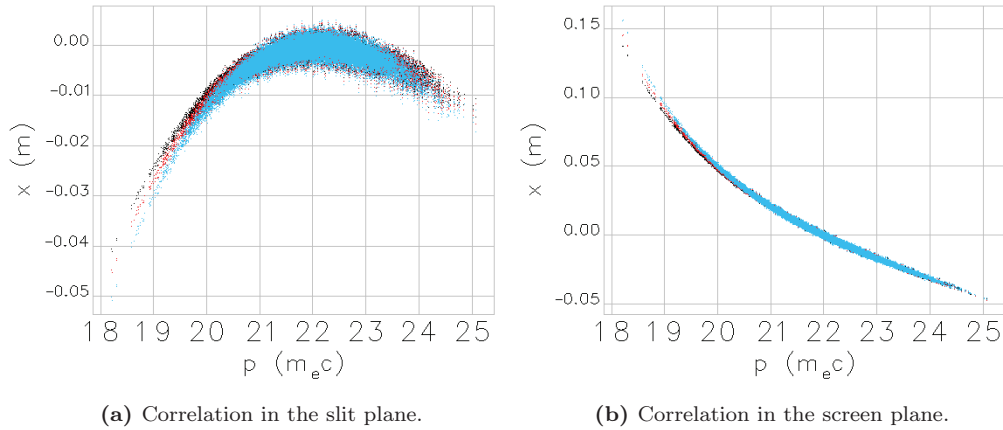


Figure 5.13: Simulated p - x -correlations for the setup A3. The red, blue and black colours indicate different settings of the quadrupole magnet during the scan. The slight deviations observed between the correlations for the different settings are caused by a small amount of non-zero dispersion that remained after optimisation of the beamline.

downstream of the added dogleg, see Fig. 5.10e.

Beamline modelling of this installation option revealed similar problems as occurred for A4. A closed dispersion solution downstream of the dogleg was achievable but required very high strengths of the quadrupole magnets. The resulting solution restrained the quadrupole scanning procedure since a vertical focus on the spectrometer screen could not be achieved. Thus, this installation was discarded as well.

Conclusion of simulations The simulations verified the setup A1 with the installation of the spectrometer magnet in a non-dispersive section of the main beamline to have essential advantages compared to a setup within an added beamline as in A2 and A3. Installation options A2 and A3 show non-linearities in the p - x -correlations in the screen plane which makes them not suitable for slice measurements. The setup A1 permits the full use of the imaging properties of the spectrometer magnet. The linear p - x -correlation on the screen allows for unambiguous reconstruction of the longitudinal slices. Therefore, A1 is the only installation option suitable for the measurements. The spectrometer magnet was installed in the ELBE beamline accordingly and the influence of the small vertical aperture in the magnet was investigated within machine operation. These experiments proved the spectrometer magnet caused aperture limitation to be tolerable. Fig. 5.14 shows a photograph of the spectrometer unit installed in ELBE. The slice emittance measurements described in the following Section 5.1.2 were taken using the setup A1.

5.1.2 Experimental results

This section presents the first results achieved from slice emittance measurements using the zero-phasing technique at ELBE. The main objective of these measurements was a proof of principle using the implemented setup. Moreover, its suitability for future characterisation of the SRF-injector and as a tool allowing the control of the emittance compensation scheme had to be evaluated.

The measurements were taken at a beam energy of ~ 18 MeV and a bunch charge of

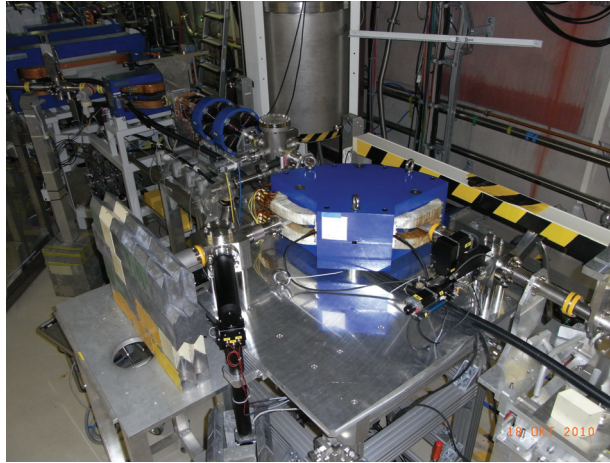


Figure 5.14: Spectrometer magnet mounted in the ELBE accelerator beamline. Beam direction is from right to left.

~ 10 pC. Different injector cavity and chirping cavity RF phase combinations were used. Two measurement periods were performed, the first in October of 2010 and a second in August of 2011, both with similar settings. The measured beam energy, the cavity settings and the entrance slit widths are summarised in Tab. 5.5. Here, 0° refers to the zero-crossing of the RF wave. A cathode DC voltage of 5 kV was applied during the measurement allowing to accelerate electrons even at injection phases of -10° . The beam energy given in the table was taken from the data of the spectrometer magnet. The set effective cavity voltages result in an energy mismatch of up to ~ 1.5 MeV in accordance with experimental data. The bunch charge was determined by a measurement using the Faraday-cup right downstream of the injector. During the first measurement period, the bunch repetition rate was 125 kHz corresponding to an average current of $1.25 \mu\text{A}$ and the spectrometer slit full width had to be set to $\text{FW}_{\text{slit}} = 20$ mm in order to reduce thermionic heat load on the slit material. The slit width could be reduced to 2 mm for the measurements during the second period due to the implemented macro-pulse operation. This mode provides pulse trains of 20 ms length. The repetition rate within the pulse train is 125 kHz while the pulse train repetition rate is 1 Hz. Hence, the average current is lowered by a factor of 50 to $0.025 \mu\text{A}$. Further reduction of the slit width could not be realised due to insufficient image intensity on the screen. The camera was triggered to 1 Hz and the exposure time of $150 \mu\text{s}$ led to averaging of 19 bunches per beam image. For both measurement periods, the resolution of the system was limited by the beam size. Five longitudinal slices were analysed according to the resolution estimations presented in Tab. 5.2.

Measurement procedure

The electron injector was optimised in order to deliver an electron beam of ~ 3 MeV with a bunch charge of ~ 10 pC. The beam was threaded through the dogleg and injected into the ELBE beamline. Particular attention was given to the dispersion characteristic, ensuring to close the dispersion using the quadrupole magnets of the dogleg. The first linac cavity was used to compensate the correlated energy spread induced by the injector. The on-crest phase of the second cavity was found by observation of the maximum in beam energy and the minimum in energy spread. The spectrometer magnet remained switched off and the

Table 5.5: Machine settings and beam parameters for each series of the measurement periods in 2010 and 2011. The scanning was performed using quadrupole magnet Q2 except for ‘series 6’ where Q3 was used. The bunch charge consistently was 10 pC.

	Meas. series	E_{meas} (MeV)	φ_{inj} ($^{\circ}$)	$V_{0,\text{eff},\text{inj}}$ (MV)	φ_{acc} ($^{\circ}$)	$V_{0,\text{eff},\text{acc}}$ (MV)	φ_{chirp} ($^{\circ}$)	$V_{0,\text{eff},\text{chirp}}$ (MV)	FW_{slit} (mm)
2010	1	17.7	0	3.0	90	6.9	72	7.4	20
	2	17.6	0	"	"	"	72	"	"
	3	17.9	10	"	"	"	114	"	"
	4	18.0	-10	"	"	"	"	"	"
	5	18.1	"	"	"	"	"	"	"
	6	17.8	"	"	"	"	120	"	"
2011	7, 8	17.9	13	3.0	90	7.4	63	7.1	2
	9, 10	17.9	0	"	"	"	63	"	"
	11	17.8	-10	"	"	"	55	"	"

electron beam was sent straight through. For the optimisation of the phase settings, the beam was observed on a screen downstream of the dipole magnet operating as a switch to direct the beam to the different experiments supplied by the ELBE. Afterwards, the beam was centred through the scanning quadrupole magnet and the spectrometer slit, again using a screen in forward direction downstream of the spectrometer magnet. Beam centring was mandatory to prevent steering effects of the quadrupole magnet during the scanning procedure and to avoid the beam from being cut by the slit depending on the strength of the quadrupole magnet. Maintaining this optimised machine setup, the spectrometer magnet was switched on and the deflected beam was observed on the spectrometer screen. It was not possible to use the zero-phasing setting of the second linac cavity when imprinting the chirp to the bunch. This was due to the measuring range of the magnetic field probe used to calibrate the spectrometer magnet limiting the beam energy to a minimum of about 15 MeV [47]. Therefore, a non-zero phase had to be used, accepting slope variations of about 20% for the $\pm 2\sigma_{x,s}$ -range. Starting from the on-crest phase of the second linac cavity, the phase was adjusted in order to increase the energy spread to match the dispersed beam size to the size of the spectrometer screen. Afterwards, a quadrupole scan was performed. Beam images and energy data delivered by the spectrometer magnet were saved for each setting of the quadrupole magnet. The range of the magnet strengths was limited by the vertical aperture of the vacuum chamber. An example of a sequence of images on the spectrometer screen is shown in Fig. 5.15.



Figure 5.15: Sequence of measured images on the spectrometer screen for different settings of the quadrupole magnet. From left to right the initially defocused beam is focused and gets defocused again. Due to energy chirp, different slices reveal minimum beam size at different strengths of the quadrupole magnet.

Analysis of the measured data

As introduced in Section 3.2, the vertical beam sizes as well as the transfer matrix elements have to be known in order to determine the slice emittance from the measurement data. These were calculated using the images of the beam and the settings of the beam transport optics as explained below.

A jitter of the beam position on the spectrometer screen was observed which was assumed to be caused by a jitter of the RF phase. All images belonging to one quadrupole scan were loaded and aligned with respect to the maximum of their horizontal (longitudinal) profiles in order to correctly assign slices. Afterwards, a range of the beam to be sliced was defined in horizontal direction. The procedure of trimming and cutting is clarified in Fig. 5.16 by means of a single image of the beam on the spectrometer screen. It was carefully considered to have a reasonable amount of particle intensity in each of the slices, particularly the outer slices, since too little intensity falsifies the calculation of σ_y . The images were cropped to the chosen range and then cut into five slices. The projection of the beam onto the vertical axis for each slice as well as the quality of the results of the fitting routine were checked visually until an appropriate final range to slice was found. The final projections of the slices were calculated after this optimisation. A post-processing routine including the following steps was applied to the profiles prior to the calculation of the beam size σ_y per slice:

- Check projections for saturation,
- perform background subtraction,
- set all intensity values below 1% of the maximum intensity to zero,
- eliminate remaining separate intensity spikes.

Since the different slices have different energies, energy-dependent transfer matrices were used. The energy information delivered by the spectrometer magnet was used to calculate the energy deviation of each slice. The exact energy-dependent transfer matrices for each slice and setting of the quadrupole magnet were taken from ELEGANT simulations. Both the matrix elements and the beam size information were then used to determine the emittance and the uncertainty of emittance applying a least-squares fitting procedure. Using the calculated emittance values and the elements of the σ -matrix determined from the fit, the vertical phase space for each of the slices was reconstructed applying Eq. 2.27.

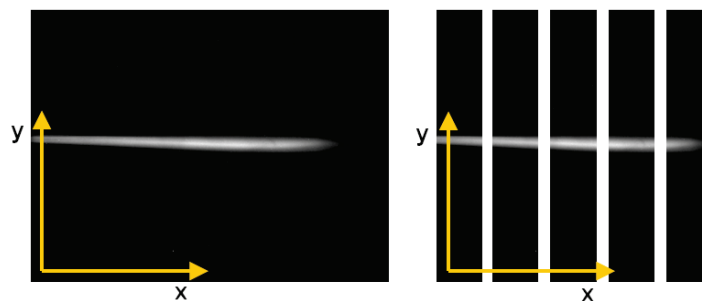


Figure 5.16: Trimming and cutting procedure applied to the images on the spectrometer screen. The range used for slicing was determined by careful examination of the intensity profiles and the results of the fitting procedure. Particular focus was put on the outer slices to avoid falsification of the calculation of the beam size.

Knowledge of both the energy corresponding to a horizontal position on the screen and the used cavity RF phase allows to calculate a longitudinal bunch profile using the relation given in Eq. (5.18). An average longitudinal profile was found from all horizontal profiles on the screen.

Measurement results

The results of the measurements are presented in plots showing the average longitudinal beam profile overlaid by bars representing the position, width and corresponding emittance value of the slices. The error bars in the representation result directly from the least-squares fit. Systematic errors due to the quadrupole calibration are not included. The magnet calibration at ELBE could not be verified by measurements. Typically, calibration errors are in the order of $\sim 1\%$ [48]. Hence, the systematic emittance error lies within the error resulting from the fit. On the right hand side, the reconstructed vertical phase space ellipses are shown. As an example, the results of the measurement ‘series 6’ (2010) are given in Fig. 5.17. The slice emittance values are correlated to the longitudinal intensity profile such that the highest emittance values are observed for slices containing the highest intensity. The behaviour may be explained by space charge effects that cause emittance growth depending on the included charge. A similar emittance characteristic was observed for all measurement series, as can be seen from Figs. B.1 to B.10 in Appendix B. The phase space ellipses of the individual slices differ not only in enclosed areas but also in their orientation since the optics was not optimised in terms of emittance compensation.

A summary of the results from all measurement series except for ‘series 11’ is given in Fig. 5.18. Similar injector cavity phase settings were set to same colours. The measurement periods are indicated by different line types, solid lines indicate period 2010 and dashed lines stand for the period in 2011. The numbering of the slices is from head to tail or from left to right in a presentation according to Fig. 5.17. The determined emittance values vary between (0.5 – 2.5) mm mrad and are in good agreement with results presented by Teichert in [49]. Here, a projected emittance of 1.5 mm mrad was measured using the solenoid of the SRF-injector and the following screen. A table summarising the results of the zero-phasing measurements can be found in Appendix B. All emittance curves

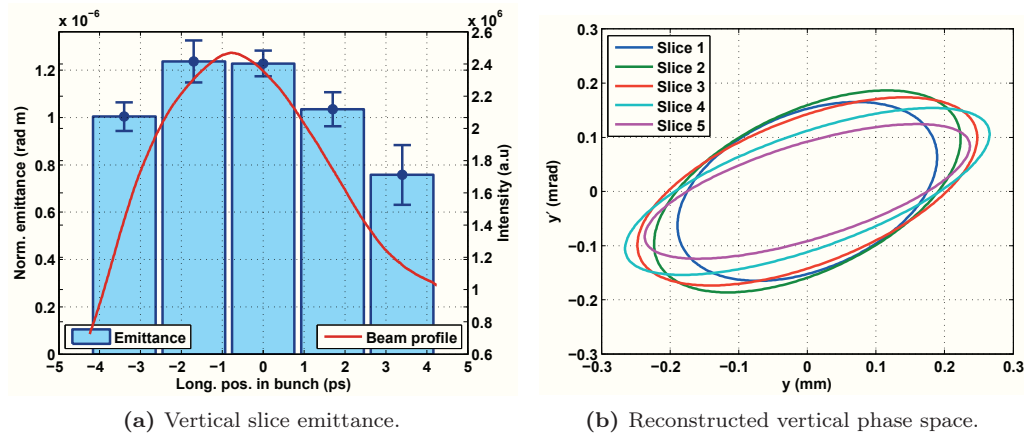


Figure 5.17: Emittance characteristic along the bunch and reconstructed phase space for measurement ‘series 6’ (2010), see Tab. 5.5 for settings.

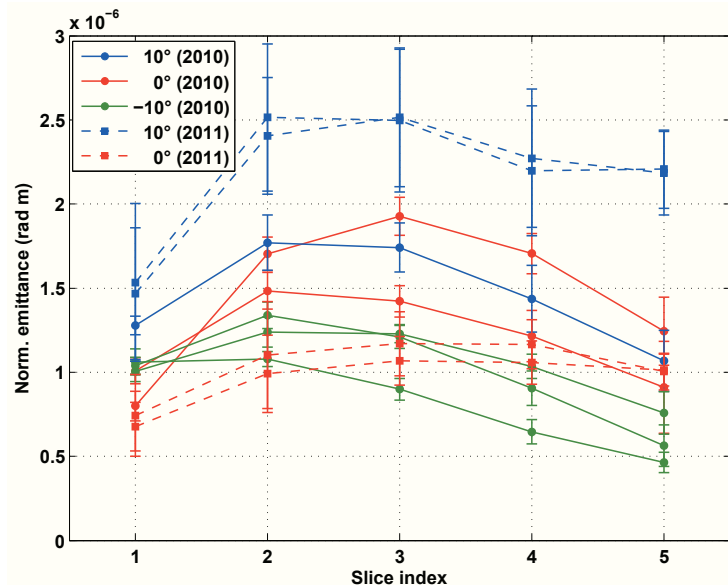


Figure 5.18: Overview of all slice emittance measurement results. The slices are numbered from head to tail of the bunch. Solid lines indicate results of measurement period 2010, dotted lines stand for measurements taken in 2011. The colour code identifies similar injector cavity phase settings.

show a similar characteristic having a larger emittance in the centre of the bunch which is decreasing towards head and tail. Measurement series with flatter longitudinal intensity profiles deliver a flatter emittance characteristic, compare again Appendix B. In the 2011 period, measurements with the same phase settings were taken immediately one after the other. The measured slice emittance values are equal within the estimated error, proving a good reproducibility of the method itself. Same phase settings within the measurement period 2010 do not exactly reproduce each other. This may be caused by repeated interruptions during the measurement procedure enforced by problems with the software of the spectrometer magnet. One observes a tendency of positive injector cavity phases leading to larger slice emittance values, including a distinct emittance maximum at position of the intensity maximum. The largest values are observed for an injector phase of 13° (2011). Phase settings of -10° lead to the lowest slice emittance and the flattest emittance characteristic along the bunch. Unfortunately, no comparison is available here since the images of ‘series 11’ taken in 2011 at a gun phase of -10° revealed a longitudinal double structure of the bunch which made them not evaluable. These results are excluded in Fig 5.18. The measurements having the 0° -setting taken in 2011 reveal a low-emittance profile similarly flat while the 0° -measurements taken in 2010 have a distinct maximum. The difference may be explained by different machine settings and a low-energy tail that was observed on the spectrometer screen during the second period. Optimisation of the beamline was carried out to reduce the effect. Nevertheless, it could not be fully eliminated. An estimation of the rms bunch length from the measured data delivered values of ~ 2 ps for all series.

5.1.3 Simulation results

Simulations consistent with the measurements taken in period 2010 were performed in order to understand the variation of the emittance over the bunch length and to verify the

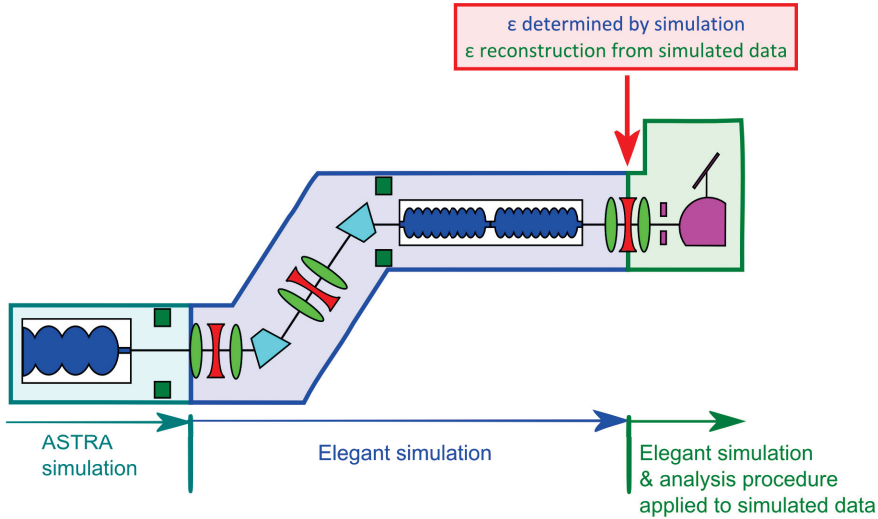


Figure 5.19: Simulation of the zero-phasing measurements were performed using ASTRA and ELEGANT. The output directly given by the simulation programs can be compared to the results achieved by applying the procedure used to analyse the measured data to simulated data.

measurement results described in the previous section. ASTRA [50] was used to model the SRF-injector to the first quadrupole magnet of the injector beamline, including space charge effects. Starting here, ELEGANT was initialised using the output of ASTRA. ELEGANT simulations do not include space charge effects. This was tolerated since the available release of ASTRA did not allow to implement the dipole magnets required for modelling of the dogleg. The procedure of the quadrupole scan was simulated calculating images of the beam on the spectrometer screen. The images were then used to calculate the slice emittance, adapting the same procedure used for analysis of the measured data as described in Section 5.1.2. All settings of the injector and the beamline were implemented according to the measurement.

ASTRA simulation of the SRF-injector

Three different ASTRA simulations including the cavity field, cathode DC field and solenoidal field were performed according to the different phase settings of the gun cavity. Tab. 5.6 summarises the most important simulated parameters at the first quadrupole magnet of the injector beamline. The beam energy, the Twiss-parameters α and β , the normalised projected emittance and the bunch length are given. The parameters are identical for both planes due to rotational symmetry of the injector components. The phase of the injector cavity clearly influences the beam parameters. The β -function and the correlation in phase space increase with a lower phase while a decrease of the bunch length and the emittance is observed. The relation between the bunch length and the injector phase is as expected on the basis of previous bunch length measurements [47]. ASTRA directly provides an output of slice emittance values. The results are presented in Fig. 5.20 for five slices. An explicit correlation between phase and emittance profile is observed. A negative phase leads to a distinct maximum of emittance values for the bunch centre and absolute values higher by a factor of 1.2 to 1.5 compared to lower phases. The 0° -setting leads to an almost flat profile while the 10° -settings unveils a

Table 5.6: Simulated ASTRA output parameters of the SRF-injector for different phase settings. The Twiss-parameters are identical for the horizontal and the vertical plane.

$\varphi_{\text{injector}}$ ($^{\circ}$)	E (MeV)	β (m)	α	σ_t (ps)	ε_n (mm mrad)
10	3.2	25.1	19.2	2.7	0.78
0	"	41.9	31.3	1.9	0.74
-10	"	55.3	41.2	1.4	0.71

broad minimum in slice emittance for the bunch centre. Tab. 5.6 states the bunches at -10° RF phase to be shorter by a factor of two compared to the 10° and by a factor of 1.4 compared to 0° . Thus, space charge effects increase for decreasing RF phase leading to larger slice emittance values observed in Fig. 5.20. Nevertheless, the projected emittance is largest for the phase settings having the lowest slice emittance values. This is caused by misalignment of the slices confirmed by simulation.

Estimation of space charge effects

The influence of space charge effects for the given measurement settings will be briefly estimated here. It is distinguished between the space charge and the emittance dominated regime according to the beam parameters. A beam is dominated by space charge if the relations

$$\frac{\varepsilon_{x,n}^2}{\sigma_x^2} \ll \frac{I_{\text{pk}}}{2I_A \beta \gamma} \quad \text{and} \quad \frac{\varepsilon_{y,n}^2}{\sigma_y^2} \ll \frac{I_{\text{pk}}}{2I_A \beta \gamma} \quad (5.22)$$

derived from the envelope equation [51, 52] are fulfilled. Otherwise the beam is dominated by emittance. The influence of space charge depends on the beam energy, the emittance, the vertical beam size and the peak beam current I_{pk} , with the Alfvén current $I_A = 17 \text{ kA}$. The criterion Eq. (5.22) was examined for the beam parameters determined from simulation

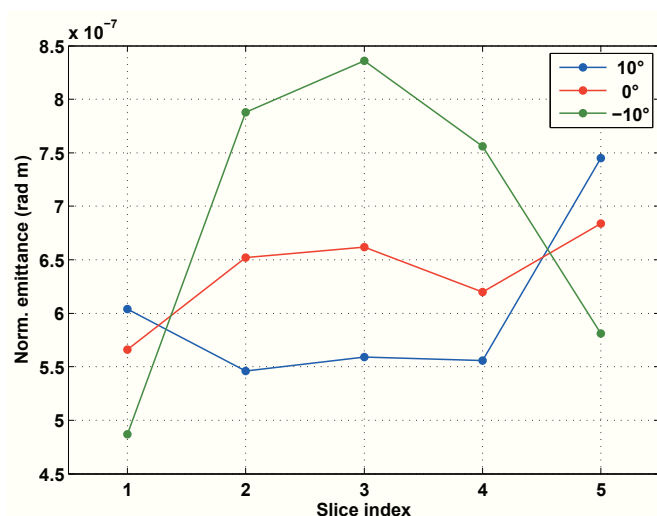


Figure 5.20: Slice emittance output at the first quadrupole magnet in the injector beamline provided by ASTRA simulation. The results are given for five slices and for the three different phase settings of the injector cavity.

Table 5.7: Estimation of the influence of space charge according to Eq. (5.22) for the different phase settings. The peak current was calculated using the bunch charge Q and the rms bunch length from $I_{\text{pk}} = Q/\sigma_t$.

$\varphi_{\text{injector}} (^{\circ})$	ε_n^2/σ^2	$I_{\text{pk}}/(I_A \beta \gamma)$	$\frac{I_{\text{pk}}/(I_A \beta \gamma)}{\varepsilon_n^2/\sigma^2}$
10	1.9×10^{-7}	1.8×10^{-5}	90.5
0	1.1×10^{-7}	2.5×10^{-5}	226.4
-10	8.0×10^{-8}	3.4×10^{-5}	422.7

given in Tab. 5.6. The results are summarised in Tab. 5.7, again assuming symmetry in horizontal and vertical direction. The space charge term $I_{\text{pk}}/(I_A \beta \gamma)$ is higher than the emittance term ε_n^2/σ^2 by a factor of 100 to 400 depending on the phase setting and the beam is space charge dominated for all of the three settings. The development of the quotient $I_{\text{pk}} \sigma^2/(I_A \beta \gamma \varepsilon_n^2)$ as a function of the beam energy was studied in Fig. 5.21 for each cavity phase. The transverse beam size as well as the bunch length were taken as constant values. The influence of space charge decreases with increasing beam energy. The 10° -setting reaches the emittance dominated regime for energies above ~ 10 MeV. Thus, during the measurement the beam is space charge dominated until having passed the first accelerator module in the ELBE beamline. For the beam of the -10° -setting, emittance domination is not achieved until ~ 20 MeV due to the shorter bunch. This significant influence of space charge is assumed to become visible as higher emittance values measured for this setting but could not be confirmed by Fig. 5.18. Fig. 5.21 clearly demonstrates the need for simulations including space charge effects to deliver more accurate results. Nonetheless, ELEGANT simulations neglecting space charge were used for the reasons already stated. The disregard is kept in mind for the interpretation of the results.

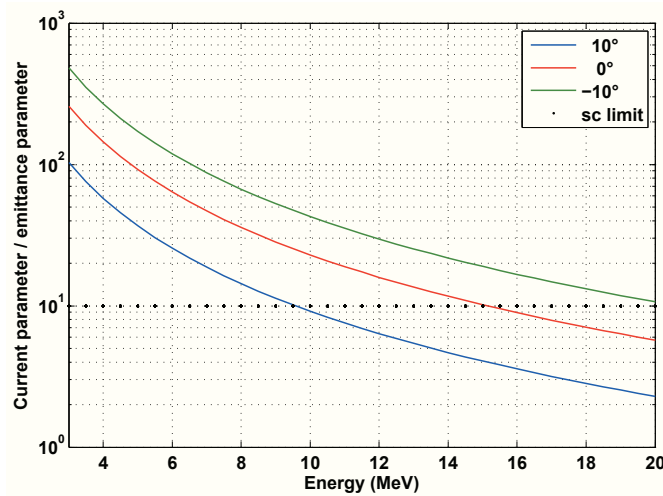


Figure 5.21: Development of $I_{\text{pk}} \sigma^2/(I_A \beta \gamma \varepsilon_n^2)$ as a function of increasing energy. The black dotted line indicates the lower limit of the space charge dominated regime. All values below this line indicate an emittance dominated beam.

Complete simulation with analysis procedure

The modelling of the beamline for the ELEGANT simulation according to the settings applied during the measurements in 2010 was challenging. The simulation of the dogleg required optimisation within tolerances of $\pm 20\%$ of the original magnet settings in order to close the dispersion and fit the β -functions to acceptable values. A beam offset from axis was observed in the simulation for reasons that could not be clarified. A centring element had to be included into the simulated beamline right upstream of the spectrometer slit to bring the simulated beam on-axis and allow for simulation of the measurement procedure.

The results of the simulations including the measurement analysis procedure applied to the spectrometer images are presented in Fig. 5.22. No essential increase in emittance is expected and the emittance characteristic is anticipated to be similar to Fig. 5.20 since no space charge effects are included in ELEGANT. The dependence between the emittance profile and the cavity phase is maintained. The highest values and a pronounced maximum are found for -10° , lower values for 0° and an almost flat profile of low values for 10° .

Evaluation of the data analysis procedure

The analysis procedure applied to the measured data can be evaluated by checking the results given in Fig. 5.22 against the slice emittance at the scanning quadrupole magnet directly provided by ELEGANT, see Fig. 5.19 for explanation. Fig. 5.23 shows the comparison for measurement ‘series 6’. The characteristic of the emittance profiles is identical, but the combination of the simulation and the analysis routine delivers larger emittance values than those directly provided by the simulation. The emittance increase is about 6%. This can be explained by the fact that ELEGANT is directly accessing the temporal coordinates of the particles to slice the bunch while the analysis routine defines slices indirectly according to the x -coordinate on the screen. Hence, the analysis routine is affected by the resolution of the spectrometer magnet, see Section 5.1.1. A larger offset of (30 – 50)% between the profiles is observed towards the outer slices. This is assumed to be caused by the trimming applied to prepare the spectrometer screen images for the

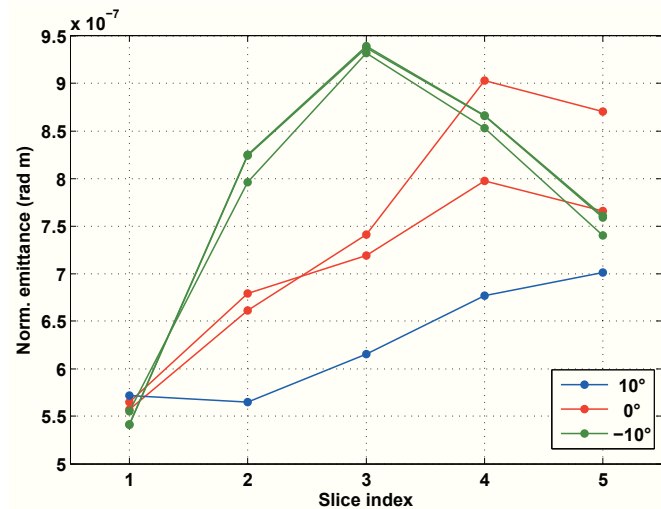


Figure 5.22: Simulated slice emittance for the settings applied during the measurement period in 2010.

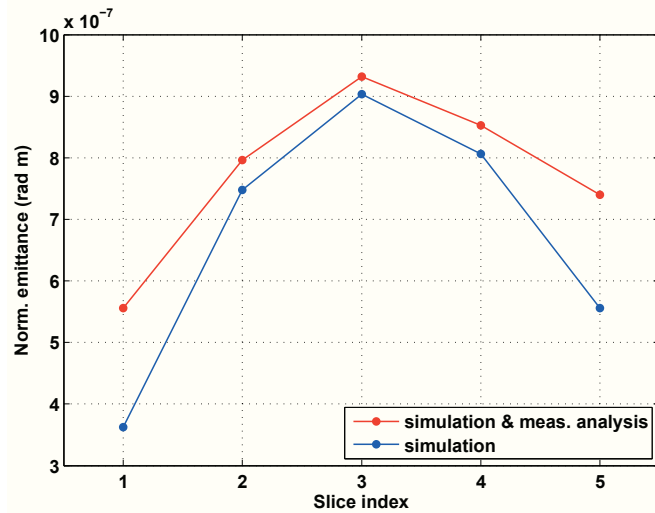


Figure 5.23: Comparison between the slice emittance values reconstructed from the simulated images on the spectrometer screen using the analysis procedure applied to the measurements and the slice emittance values directly given by ELEGANT for measurement ‘series 6’ (2010).

analysis, as described in Fig. 5.16. In doing so, the slices shift towards the centre of the bunch and the position of the slices is slightly different compared to ELEGANT, leading to a higher emittance for the outer slices.

Comparison of measurement and simulation

Fig. 5.24 gives a direct comparison of the measurement and simulation results of the data taken in 2010. The measured emittance values are significantly higher than the simulated values. All simulated values lie below 1 mm mrad while the measured values reach up to 2 mm mrad. Such a deviation had to be expected since space charge effects were only taken into account for the first part of the simulation. The general behaviour of the emittance values depending on the cavity phase is different for simulation and measurement. The simulation indicates a decreasing emittance from -10° to 10° which seems to be reversed in the measurement. Here, the -10° -setting leads to the lowest emittance. Nevertheless, a clear correlation between the cavity phase and the emittance profile has not yet been found for the measured data.

5.1.4 Conclusion

The zero-phasing technique at ELBE proved to be working for slice emittance measurements and the results of the first measurements are satisfying. As expected, the emittance profile resembles the longitudinal intensity profile of the bunch. The measured values lie in the expected range. Reproducibility was shown for measurements carried out directly one after another. The emittance values differ between the first and second measurement period, the 10° -settings of 2011 delivered higher values than observed in 2010. The implementation of the machine settings applied during the measurement for the simulation proved to be problematic and required improvisation. Space charge effects were neglected for part of the simulation, leading to significantly lower values than expected due to measurements. An unambiguous dependence of the emittance on the injector

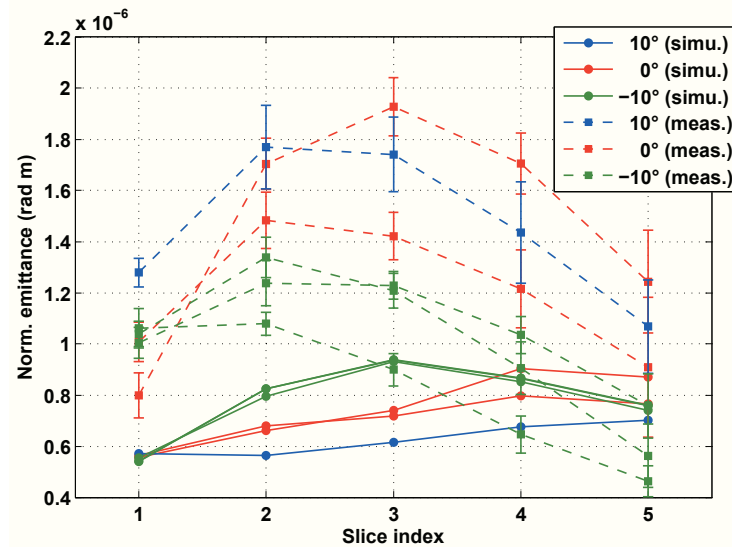


Figure 5.24: Comparison of the measured and simulated slice emittance values for the measurements taken in 2010. The simulation leads to values significantly lower than those observed during the measurement.

cavity phase could not yet be identified. Simulations indicate -10° to yield the largest emittance values, but this was not observed for the measurements. On-line simulation is planned to improve the reliability of simulating the measurement procedure. The idea is to perform several quadrupole scans to determine the phase space distribution at different locations along the beamline, starting at the exit of the SRF-injector. The reconstructed phase space distributions can be directly compared to the simulated phase space. This allows for a stepwise verification of the adapted setup and the properties of the simulated beam. Furthermore, space-charge effects are planned to be included in future simulations by using a new version of ASTRA to replace the current ELEGANT simulations.

Until now, threading the beam through the dogleg has been a time-consuming and lengthy procedure. In the long term, the SRF-injector will replace the thermionic injector installed in straight direction to the ELBE beamline. This makes it easier to study the electron source since the re-adjustment of the dogleg for any changes in phase and hence energy will no longer be required. Detailed characterisation of the injector is planned, including investigations on the phase dependence and measurements at a higher bunch charge.

The most important application of the slice emittance measurements is to put the emittance compensation scheme into operation. It is planned to automate the measurement procedure allowing to save a desired number of spectrometer images for each setting of the quadrupole magnet, reducing statistical errors by beam fluctuations. An on-line slice analysis is desirable to simplify the initialisation and adjustment of the strength of the solenoid magnet used for the compensation. Thus, the implementation of the measurement analysis tool into the control system is essential.

5.2 Transverse deflector technique at PEGASUS

The PEGASUS photoinjector equipped with a 1.6-cell 2.9 GHz cavity is operated by the Particle Beam Physics Lab (PBPL) at the UCLA. The injector is foreseen for various fields

Table 5.8: Current beam parameters of the PEGASUS photoinjector.

Parameter	
Beam energy	4 MeV
Bunch charge	(1 – 100) pC
Bunch length	< 100 fs – 2 ps
Norm. emittance	< 1 mm mrad

of research in accelerator physics and application of beams, e.g. the photoinjector blowout regime and ultra-fast electron diffraction [53, 54]. It currently delivers a low-emittance beam of 4 MeV energy, medium bunch charge and sub-ps pulses. Tab. 5.8 [53] summarises the current PEGASUS beam parameters. A view along the beamline of the photoinjector is shown in Fig. 5.25. The injector cavity is located left of the solenoid which can be seen in the leftmost part of the figure. Different measurement stations follow, including the electron diffraction probe chamber, view screens and a Faraday-cup. Furthermore, two focusing quadrupole magnets, a deflector cavity and a spectrometer magnet separating the diagnostics beamline into a forward direction and a dispersive arm used for energy resolved measurements are included.

The characterisation of the injector requires detailed knowledge of the beams' phase space distribution for which the transverse deflector is implemented into the diagnostics beamline. The deflector is used to measure both the longitudinal phase space and the slice emittance in the horizontal plane. The first slice emittance measurements are considered in the following sections.

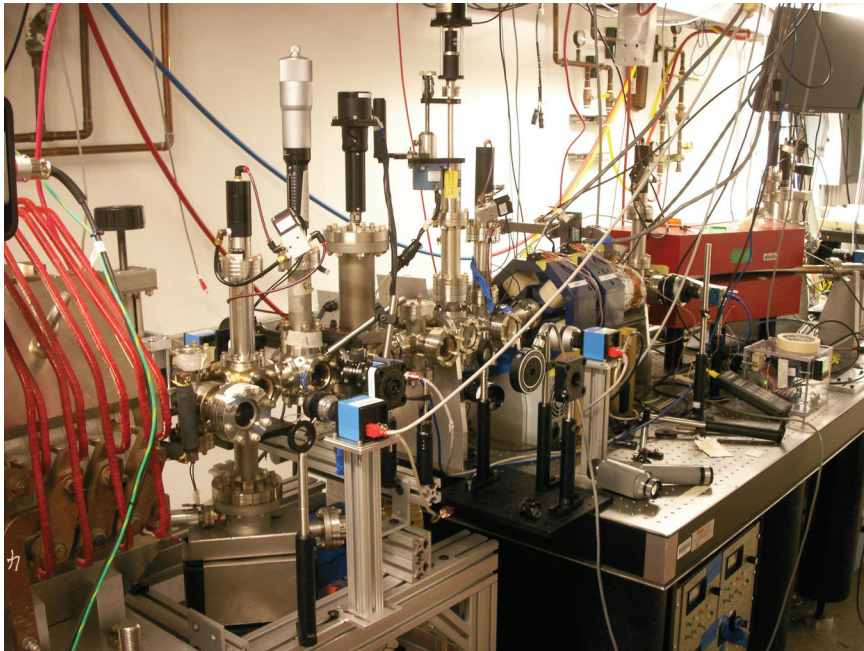


Figure 5.25: View of the PEGASUS photoinjector, beam direction is from left to right. On the left side the solenoid can be seen. The actual electron source located directly to the left of the solenoid is not visible on the photograph. The solenoid is followed by several measurement stations, a doublet of quadrupole magnets, the transverse deflecting cavity and the spectrometer dipole.

5.2.1 Measurement setup

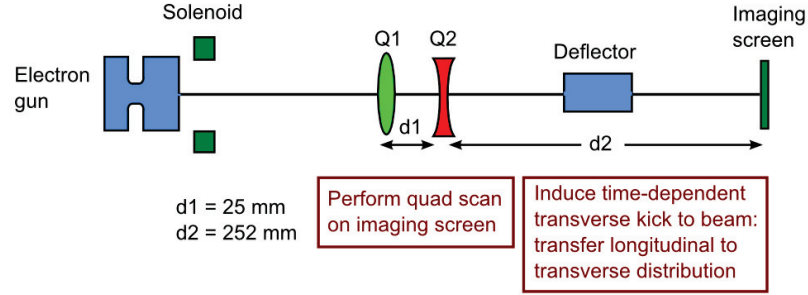


Figure 5.26: Measurement setup for slice emittance measurement using transverse deflecting cavity at the UCLA Pegasus photoinjector.

The setup used for the measurement consists of two quadrupole magnets, the vertically deflecting cavity and a fluorescent YAG-screen, all being separated by drift sections, as shown in Fig. 5.26. Both quadrupole magnets were used during the measurement with the first magnet used for the scanning procedure itself. The first quadrupole magnet focuses the beam in horizontal direction and has a defocusing effect in the vertical plane. Hence, the vertical beam size from emittance $\sigma_{y,\varepsilon}$ varies and becomes large throughout the measurement leading to a poor temporal resolution, see Section 4.5. The second quadrupole magnet is used to compensate for the defocusing effects of the first magnet such that the resolution is optimised. The beam is deflected in vertical direction and therefore the horizontal slice emittance can be measured. The implemented TM_{110} -deflector cavity is a nine-cell standing wave cavity working at a frequency of 9.6 GHz [55].

Temporal resolution of the measurement

A resolution criterion was introduced and discussed in Section 4.5. Using the relation between the transverse screen coordinate and the deflecting voltage in Eq. (4.20), the difference in voltage required to separate two adjacent slices according to Eq. (4.24) is given by

$$\Delta V_{y,\min} = 2\sigma_{y,\varepsilon} \frac{\beta c p_z}{d e}. \quad (5.23)$$

The $\pm 2\sigma_s$ -range of the beam which is analysed as explained in Fig. 4.7b corresponds to a total difference in voltage. According to Eq. (4.25) it is required to be

$$\Delta V_{y,\text{total}} \geq n_{\text{slices}} \cdot \Delta V_{y,\min} \quad (5.24)$$

and the voltage seen by a particle at position $\Delta z = \sigma_z$ in the bunch has to be

$$V_y(\sigma_z) \geq \frac{n_{\text{slices}} \cdot \Delta V_{y,\min}}{4}. \quad (5.25)$$

The required peak deflecting voltage can be found from Eqs. (4.17) and (5.23)

$$V_{y,0} \geq \sigma_{y,\varepsilon} \frac{\beta^2 \lambda}{4\pi \sigma_z} \frac{c p_z}{d e} \cdot n_{\text{slices}}. \quad (5.26)$$

Table 5.9: Beam and deflector parameters used for the estimation of the temporal resolution for realistic measurement conditions. The electron beam energy and bunch length are taken from measurement data. The emittance is the largest expected value, see Tab. 5.8, which is in accordance to values from projected measurements. The β -function is assumed to be constantly kept at a low value of 1 m during the measurement procedure. The deflector voltage and drift length are taken from [56].

Beam parameters				Deflector parameters		Drift
E (MeV)	ε_n (mm mrad)	β -function (m)	σ_t (ps)	f (GHz)	$V_{y,0}$ (kV)	d (m)
3.3	1	1	0.8	9.6	500	0.15

The deflecting voltage increases with growing beam energy, beam size and number of slices and decreases for longer bunches, a higher RF frequency and a longer drift between deflector and screen. Expressing the beam size $\sigma_{y,\varepsilon}$ in terms of the normalised emittance and the β -function gives

$$V_{y,0} \geq \sqrt{\beta_y \frac{\varepsilon_{y,n}}{\beta \gamma}} \frac{\beta^2 \lambda}{4\pi \sigma_z} \frac{c p_z}{d e} \cdot n_{\text{slices}}. \quad (5.27)$$

Rearranging yields the maximum number of slices to be analysed within the resolution

$$n_{\text{slices}} = V_{y,0} \frac{\sqrt{\beta \gamma}}{\sqrt{\beta_y \varepsilon_{y,n}}} \frac{4\pi \sigma_z}{\beta^2 \lambda} \frac{d e}{c p_z}, \quad (5.28)$$

from which the temporal resolution Δt_{\min} can be found

$$\Delta t_{\min} = \frac{4 \sigma_t}{n_{\text{slices}}} = \frac{\sqrt{\beta_y \varepsilon_{y,n}} \beta \lambda p_z}{V_{y,0} \sqrt{\beta \gamma} \pi d e}. \quad (5.29)$$

Using the beam and deflector parameters summarised in Tab. 5.9, a maximum number of five slices is calculated. This corresponds to a temporal resolution of ~ 610 fs.

5.2.2 Experimental results

The electron injector was adjusted to deliver bunches of 3.3 MeV electron energy and a bunch charge of ~ 10 pC. These beam parameters were determined using a spectrometer dipole and a Faraday-cup. The beam was centred through both the quadrupole magnets and the deflecting cavity to avoid steering effects of the magnets. Appropriate settings of the quadrupole magnets had to be found in preparation for the automated measurement procedure. With the TCAV switched off, the strength of the second quadrupole magnet was adjusted until a minimum vertical beam size on the screen was achieved. This procedure was repeated for each setting of the first quadrupole magnet during the scan such that a set of matching combinations of both magnet strengths was found. Afterwards, the zero-crossing RF phase of the TCAV was found by adjustment of the phase such that the centroid of the beam on the screen did not change position while on- and off-switching the deflector. For the actual measurement, the deflector was switched on and the quadrupole scan was performed using the prior saved settings of the quadrupole magnets. Ten repeated images of the deflected beam on the screen were saved for each

setting. The measurement procedure was repeated two times, keeping the same machine settings and both series were analysed individually.

Analysis of the measured data

The analysis procedure is very similar to that applied for the zero-phasing measurements described in Section 5.1.2. The horizontal beam size and the transfer matrix elements are needed to calculate the emittance.

The beam arrival time differs due to limited synchronisation, resulting in a phase change and thus in a significant variation of the vertical beam centroid position on the screen. In a first step, all beam images were aligned in vertical direction and a vertical range to be sliced was found. It was carefully checked for all slices of each image to contain enough beam intensity to avoid falsification of the beam size calculation. This was verified by checking the horizontal profiles and the results of the quadrupole scan fit. The range finally chosen was divided into five slices and a beam profile for each slice of each image was calculated. The same vertical range was used for the analysis of both measurement series. A post-processing routine as explained in Section 5.1.2 was applied to the profiles. The beam size was calculated for the slices of each image and an average σ_x was found from the ten repeated profiles having the same settings. The average beam size values and the transfer matrix elements found using Eq. (3.16) were used as input for a least-squares fitting procedure to determine the emittance of the slices. An average of all longitudinal beam profiles was used for the graphical representation of the results.

Measurement results

The results of the first measurement series are shown in Fig. 5.27. The average longitudinal profile in Fig. 5.27a is overlaid by bars representing the temporal width of the slice and the slice emittance. The errors include contributions from the fitting procedure, systematic errors are assumed to lie within these. Fig. 5.27b shows the horizontal phase space reconstructed using the calculated emittance and Twiss-parameters. The emittance profile resembles the intensity profile. A maximum emittance is observed in the high-intensity centre of the bunch which is explained by space charge effects. The emittance decreases

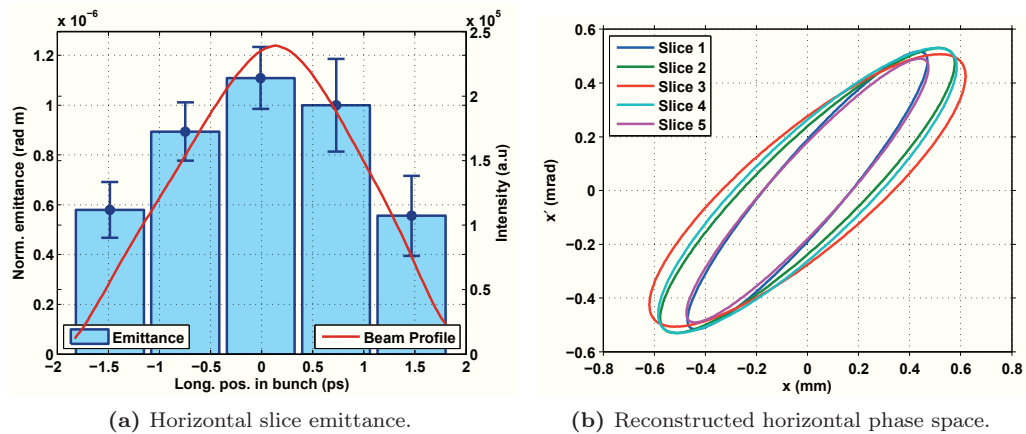


Figure 5.27: Emittance characteristics along the bunch and reconstructed phase space for measurement ‘series 1’.

Table 5.10: Slice emittance values measured using the transverse deflecting cavity at the PEGASUS photoinjector.

Slice	Normalised emittance (mm mrad)	
	‘Series 1’	‘Series 2’
1	0.57 ± 0.11	0.47 ± 0.15
2	0.89 ± 0.12	0.76 ± 0.12
3	1.11 ± 0.12	0.94 ± 0.13
4	1.00 ± 0.19	0.89 ± 0.12
5	0.56 ± 0.16	0.51 ± 0.16

towards head and tail of the bunch and varies around 1 mm mrad. A bunch length of $\sigma_t = 0.8$ ps was reconstructed for both series. The phase space ellipses of the different slices are not aligned since no emittance compensation was applied. Head and tail of the bunch reveal ellipses of similar size and orientation that are visibly misaligned with respect to the inner slices. The emittance results of both measurement series are summarised in Fig. 5.28. The characteristics of the emittance are almost identical but the profile of ‘series 2’ is consistently lower than the profile of ‘series 1’. The slice emittance values are equal within their errors. A maximum deviation of 18% between both series is observed for the centre slice. The absolute emittance values lie between (0.5 – 1.1) mm mrad which is in good agreement with the expectations of projected emittance values ≤ 1 mm mrad [57]. A summary of the exact slice emittance values is given in Tab. 5.10.

5.2.3 Conclusion

The setup consisting of two quadrupole magnets and the horizontally deflecting cavity proved to be adequate for slice emittance measurements and the determined values lie within the expected range. The measurements were reproducible within the error range.

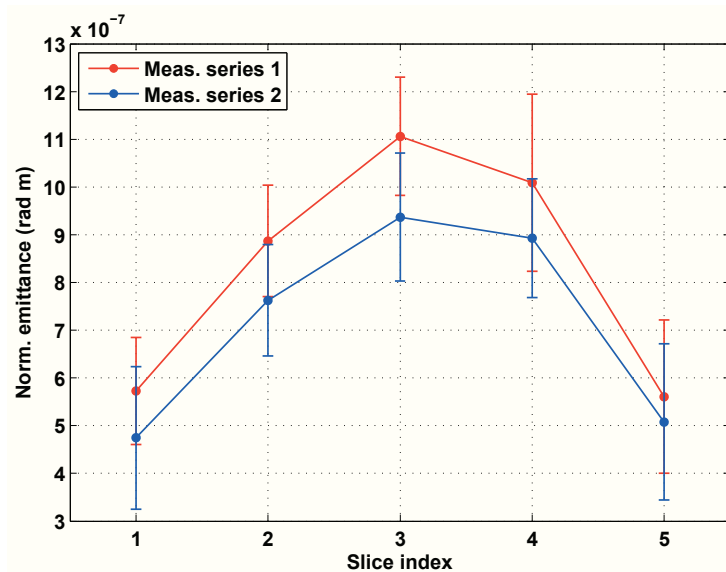


Figure 5.28: Summary of the slice emittance results from both measurement series. The slices are numbered from head to tail of the bunch.

Planned beam studies will investigate the influence of the bunch charge and the laser spot size at the cathode on the emittance along the bunch [57]. Furthermore, the impact of the solenoidal field will be characterised to allow for initialisation, adjustment and verification of the emittance compensation scheme. Future activities include simulations using ASTRA which allows to include space charge and to implement a field map of the deflector to exactly model the induced kick.

5.3 Conclusion of slice emittance measurement techniques

Two different methods to measure the slice emittance were described including their working principle and an example measurement each. Both the zero-phasing technique at ELBE as well as the transverse deflector technique at PEGASUS were successfully applied in real accelerator environments and confirmed their adequacy for slice diagnostics by delivering satisfying results.

The general advantages and drawbacks of the techniques as discussed in the previous sections are summarised in Tab. 5.11. The zero-phasing technique is suitable for a broad energy range up to high energies, allows for ps-resolution and can be realised using mandatory components of the accelerator. Its main drawback is the double correlation required to transfer the temporal to a transverse coordinate. The deflector technique has the advantage of the directly induced correlation between the temporal and the transverse coordinate. Furthermore, the possibility of energy spread measurements is provided when using an additional dipole magnet. The application of the deflector is particularly suitable for low beam energies, where sub-ps resolution can be achieved. The deflection of higher energy beams is possible but needs considerable effort in design and operation, as is briefly explained in the following.

The degree of deflection a particle experiences in a deflecting cavity was introduced in Eq. (4.22). Deflection increases with the particle's position in the bunch, the peak deflecting voltage and the drift length between deflector and observation screen. It decreases with the beam energy and RF wavelength. The peak deflecting voltage provided by a deflector depends on the shunt impedance R_s and the peak RF power P_{RF} coupled

Table 5.11: Comparison of the advantages and disadvantages of the zero-phasing and the transverse deflector technique.

	Zero-phasing	Deflector
Hardware components	cavity, quadrupole, dipole	quadrupole, deflector
Sole use of existing hardware	yes	no
Measurement location	downstream chirp cavity	close to gun
Induced correlations	t - E , E - x	t - x
Sliced σ_E measurement	no	with additional dipole
Measurement in x and y -plane	with additional dipole	with additional polarisation
Energy range	low to high energy	dominantly low energy
Temporal resolution	ps	ps to sub-ps

into the TCAV according to the relation [33]

$$V_{y,0} = \sqrt{2 R_s P_{\text{RF}}}. \quad (5.30)$$

Hence, the deflection can be increased by:

- Increasing the peak RF power coupled into the cavity,
- optimising the shunt impedance,
- operating at a higher RF frequency.

An estimation of the required peak voltage and peak RF power for different beam energies and bunch lengths is presented in Tab. 5.12. Here, a 1.3 GHz single-cell cavity is assumed, as planned to be used for characterisation of the *BERLinPro* gun, see Section 7.1. Ten longitudinal beam slices were required to be analysable within the resolution. The estimation confirms the particular suitability of the deflector technique for low beam energies when deflecting short bunches in the order of 1 ps rms. A sufficient deflection of short sub-ps bunches at higher beam energies is challenging, as the realisation of a suitable deflector for this regime demands designing multi-cell deflecting structures operated at high frequencies. These structures provide high values of R_s in the order of a few tens of $\text{M}\Omega$. In combination with a high-performance RF transmitter, multi-cell deflectors are capable of deflecting short bunches up to tens of GeV. At LCLS, a 1.5 m long 11.4 GHz deflector providing a total shunt impedance of $\sim 30 \text{ M}\Omega$ and a deflecting voltage of $\sim 40 \text{ MV}$ is being designed to deflect a 13.6 GeV beam of sub-ps bunch length [60]. As the energy range, also the temporal resolution of the deflector technique depends on the deflecting voltage, see Eq. (5.29). In addition, the drift length, the RF frequency and the beam energy have to be considered. Optimisation of these parameters allows to achieve a resolution in the fs-range, emphasising the great potential of the deflector technique. The actual temporal resolutions estimated for the deflector setup described in Section 5.2 are summarised in Tab. 5.13, including the most important parameters. For comparison, the values for the zero-phasing technique discussed in Section 5.1 are given. Here, the resolution depends on the slit setting. A resolution better than 150 fs was found for the minimum slit width (optimum case, $29 \mu\text{m}$ rms). In practice, the minimum slit width could not be applied due to the very low beam intensity and the open-slit case is

Table 5.12: Required peak voltage and peak RF power for a 1.3 GHz single-cell cavity of $R_s = 3.5 \text{ M}\Omega$, which is a typical value for a single-cell cavity [58, 59], deflecting a beam of $\epsilon_n = 1 \text{ mm mrad}$ and $\beta = 1 \text{ m}$. The screen is placed in a distance of 2 m and ten slices are assumed to be analysed. The relations introduced in Eqs. (5.27) and (5.30) were used for the estimation. The green colour indicates values achievable with little effort, grey stands for deflection requiring essentially higher effort.

E (MeV)	$\sigma_t = 5 \text{ ps}$		$\sigma_t = 1 \text{ ps}$	
	V_0 (kV)	P_{RF} (kW)	V_0 (kV)	P_{RF} (kW)
2	67	0.6	336	16
5	102	1.5	511	37
10	142	2.9	709	72
50	311	13.8	1556	346

Table 5.13: Comparison of the estimated resolution for the zero-phasing and the deflector technique under measurement conditions. The most important parameters determining the resolution are included as well.

	Zero-phasing (ELBE)	Deflector (PEGASUS)
Resolution	(78 – 140) fs (optimum) (1.1 – 1.9) ps (realistic)	610 fs
Beam energy	18 MeV	3.3 MeV
Beam size (rms) at screen	29 μm (optimum) 400 μm (realistic)	370 μm

more realistic. Now, the resolution is limited by the beam size of 400 μm and worsens by more than a factor of ten. The deflector technique at PEGASUS reaches a resolution of 610 fs, which is better by a factor of two to three compared to the realistic resolution of the zero-phasing technique. It must be noted that the beam energy is much lower here. When changing the energy to 18 MeV, the resolution drops to 1.4 ps and is comparable to realistic values for the zero-phasing technique. Anyhow, the deflector resolution can be increased by extending the short drift section (currently only 0.15 m). Scaling is inversely linear with distance such that a 1.5 m long drift allows for 61 fs resolution. Assuming a RF frequency of 1.3 GHz instead of 9.6 GHz to 1.3 GHz again decreases the resolution by a factor of seven.

The essential advantage of the deflector technique is the dedicated design for the intended use. Several parameters can be optimised to achieve optimal performance, pushing the resolution far beyond what is achievable with the zero-phasing technique. Nevertheless, the effort in constructional design, the substantial increase of cost and the space-consuming integration into the beamline makes the deflection of short bunches of high energy at fs-resolution a greatly challenging task. In contrast, bunches of a few ps can be easily deflected up to 100 MeV using a compact and low-effort single-cell deflector system. This single-cell approach is promising to be used for the ps-resolution slice emittance measurements for the *BERLinPro* gun, as described in Section 7.1.

6 Phase space tomography

The term tomography describes a technique that allows for the reconstruction of a n -dimensional object from its $(n-1)$ -dimensional projections. Tomography is commonly known as a medical diagnostics tool. Here, one-dimensional projections are used to reconstruct two-dimensional images which can be assembled to result in a three-dimensional model of the object [61]. The principle of tomography can similarly be applied to electron beams in order to reconstruct the transverse distribution of the beam in phase space. The 3D bunch is projected onto a 2D screen, imaging the (x, y) -distribution of the bunch. 1D projections (histograms) of the x -coordinate allow for reconstruction of the horizontal phase space while those of the y -coordinate are used to reconstruct the vertical phase space. Phase space tomography primarily works with projections of the complete bunch but can be extended to reconstruct the phase space distribution of temporal slices.

This chapter gives a short introduction to tomography. The basic idea of image reconstruction is introduced. A reconstruction algorithm based on the Maximum Entropy principle that was implemented in Matlab will be explained. An evaluation of the reconstruction will be presented. The method is applied to phase space tomography and results of measurements taken at the BESSY II pre-injector linac will be presented.

6.1 General principle of tomography

Tomography relies on the observation of a distribution from different view angles. The principle of tomography is explained in Fig. 6.1 schematically. A rectangular model distribution is rotated by defined angles, providing four different views of the distribution at which projections can be calculated on a defined axis. The rotation or, more generally, the transformation the distribution has undergone is required to be known in order to allow for reconstruction. The measured histograms are transformed applying the inverse transformation corresponding to the individual histogram. The area within all back-transformed histograms constitutes the initial distribution. The general requirement to yield the full information of the distribution from a tomographic reconstruction is to cover an effective range of 180° rotation angle. Furthermore, the angles should be equidistant in order to minimise reconstruction errors. The rotation angle φ is used throughout this section. In Section 6.2, a different variable Ψ is introduced to evaluate the rotation of phase space distributions.

6.1.1 Tomographic image reconstruction

Unambiguous reconstruction is permitted given an infinite number of projections in a range from 0° to 180° . In practice, the number of projections is limited. This indicates the need for a reconstruction algorithm able to cope with incomplete sets of data. The Maximum Entropy algorithm (MENT) provides a possibility to reconstruct the primary distribution from a small number of measured projections. MENT reconstructs the most probable distribution that fulfils the boundary conditions given by the measured projections. Details on MENT can be found in [62] and [63]. Subsequently, the basics of the application of MENT for image reconstruction will be explained following the nomenclature of [63].

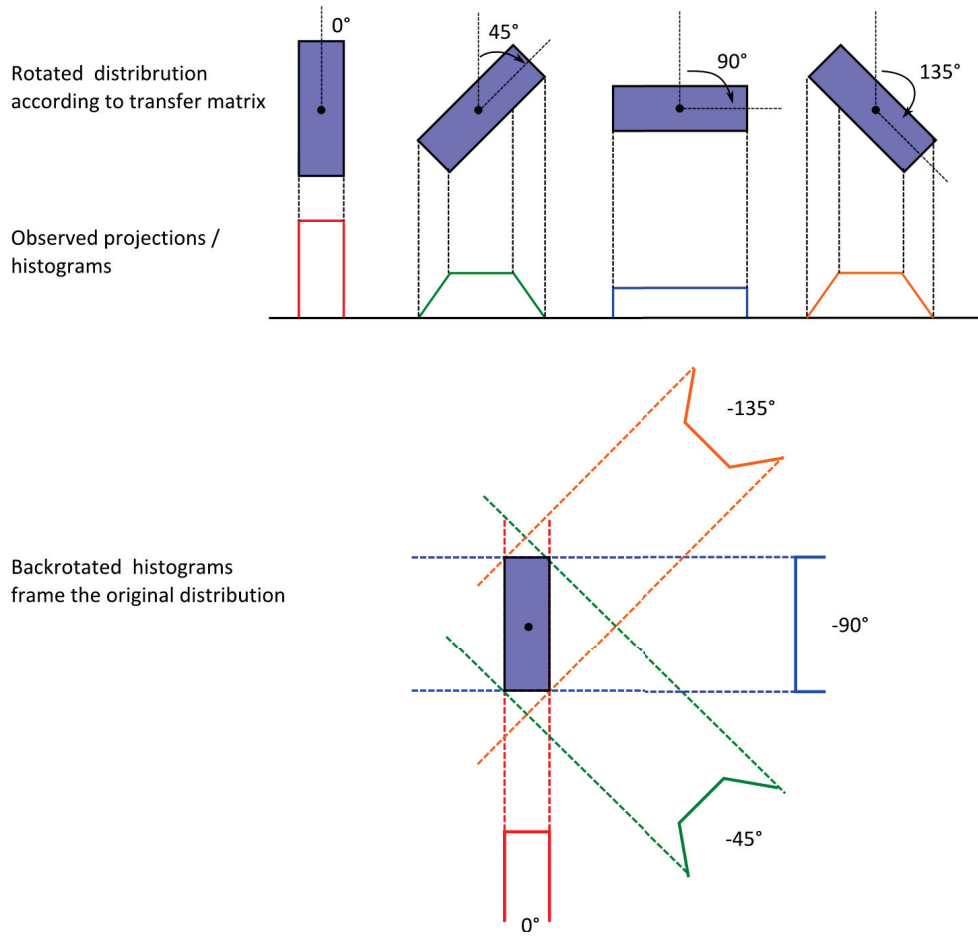


Figure 6.1: Schematic drawing of the working principle of tomography. The model distribution of rectangular shape is rotated by known angles. Thus, the distribution can be observed from different view angles. A histogram is measured for each view, indicated in red, green, blue and orange. The back-transformation of the histograms according to the known transformation of the initial distribution allows for reconstruction of the rectangle.

Description of a binned distribution

The idea of the reconstruction algorithm will be introduced by means of the simple uniform distribution given in Fig. 6.2. The distribution is described by three histograms measured at different view angles. The non-discretised histograms are indicated by the dotted blue line and the light-blue area. The boundaries of the three histograms frame the distribution. To allow for a reconstruction of structures within the distribution, the histograms have to be discretised. In the example, each of the histograms is divided in two bins. The bin boundaries divide the distribution into six polygons. Each polygon has a specific unknown function value ρ , e.g. the particle density for application to phase space, given by the distribution itself. The solid blue lines represent the binned histograms that are used for the reconstruction. One projected value G_{jm} is obtained per histogram bin. The value G_{jm} represents an integration over all polygons contributing to the individual bin m of a histogram j . Thus, the value G_{jm} for a certain bin of an individual histogram is given as the sum of all polygon function values ρ weighted by the size of the polygon

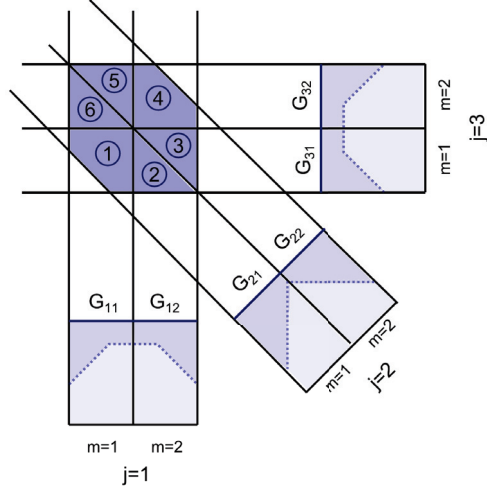


Figure 6.2: Model distribution viewed at three different angles. The solid blue lines indicate the three histograms consisting of two bins each, which divide the distribution into six polygons. For completeness, the non-discretised histograms are drawn as well, indicated by the dotted lines. A projected value G_{jm} is assigned to each bin m of histogram j . The projected value represents an integration over all polygons that lie within the considered bin of the histogram.

area F . This can be expressed by

$$G_{jm} = \sum_{\nu} \rho_{\nu} F_{\nu}, \quad (6.1)$$

with ν indicating the indices of all contributing polygons. The example in Fig. 6.2 provides the following set of six equations

$$\begin{aligned} G_{11} &= \sum_{\nu=1,5,6} \rho_{\nu} F_{\nu}, & G_{12} &= \sum_{\nu=2,3,4} \rho_{\nu} F_{\nu}, \\ G_{21} &= \sum_{\nu=1,2,6} \rho_{\nu} F_{\nu}, & G_{22} &= \sum_{\nu=3,4,5} \rho_{\nu} F_{\nu}, \\ G_{31} &= \sum_{\nu=1,2,3} \rho_{\nu} F_{\nu}, & G_{32} &= \sum_{\nu=4,5,6} \rho_{\nu} F_{\nu}. \end{aligned} \quad (6.2)$$

In order to reconstruct the primary distribution from the projected values, the function value ρ_{ν} of each polygon has to be determined. All areas F_{ν} of the polygons can be calculated using the known bin boundaries. Thus, for the given example, the system of equations can be solved and all ρ_{ν} can be calculated. Generally, the number of polygons exceeds the number of measured projected values. This leads to an under-determined system of equations which cannot be solved exactly. An iterative approach has to be found in order to reconstruct the most probable distribution.

Iterative approach

The iterative method based on the MENT algorithm will be described here. Following the MENT approach, it is convenient to introduce multipliers H , as introduced by Scheins in [63]. One multiplier H_{jm} is assigned to each bin of each histogram, using the same nomenclature as for the projected values G_{jm} . The function value ρ of a polygon is given

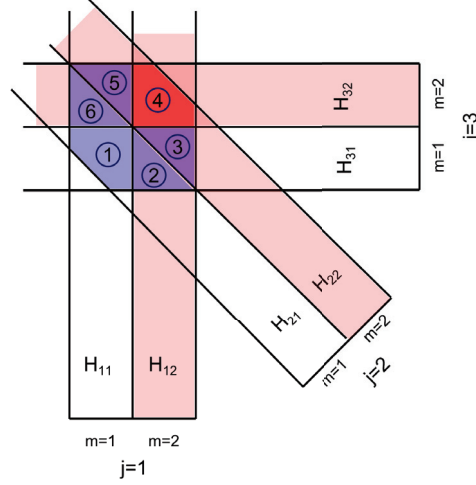


Figure 6.3: Model distribution viewed at three different angles. A multiplier H_{jm} is introduced for each histogram and bin combination. The function value of each polygon is given by the product of the multipliers of all involved bins. The red polygon with index $\nu = 4$ was chosen as an example. The polygon is defined by the red-shaded bins, one of each histogram.

as the product of all multipliers H_{jm} contributing to the polygon ν

$$\rho_\nu = \prod_{j=1}^J H_{jm}. \quad (6.3)$$

Here, J is the total number of histograms. Fig. 6.3 illustrates the meaning of the multipliers schematically. The red polygon of index $\nu = 4$ shall be considered more closely. It is composed of the three red-shaded bins, one of each histogram. The function value ρ_4 is calculated as the product of the H_{jm} corresponding to the red bins, namely

$$\rho_4 = \prod_{j=1}^3 H_{jm} = H_{12} \cdot H_{22} \cdot H_{32}. \quad (6.4)$$

According to Eq. (6.3), all polygon function values which in turn compose the binned distribution can be calculated in case all multipliers H_{jm} are known. Therefore, the main purpose is to find all multipliers H_{jm} representing the distribution. Combining the definitions given by Eqs. (6.1) and (6.3) provides an iteration rule for the calculation of H_{jm} . A straightforward iteration rule is given in [63]

$$H_{jm}^{(i+1)} = \frac{G_{jm}^{\text{meas}}}{G_{jm}^{(i)}} H_{jm}^{(i)}. \quad (6.5)$$

The use of this rule in the algorithm led to overshooting. The iteration rule had to be modified to

$$H_{jm}^{(i+1)} = k^{(i)} \cdot H_{jm}^{(i)} \quad \text{with} \quad k^{(i)} = 10^{\log(G_{jm}^{\text{meas}}/G_{jm}^{(i)})/40} \quad (6.6)$$

$$\text{and} \quad G_{jm}^{(i)} = \sum_{\nu} \rho_{\nu}^{(i)} F_{\nu} = \sum_{\nu} \left(\prod_{j=1}^J H_{jm}^{(i)} \right) F_{\nu} \quad (6.7)$$

to provide convergence. The index i numbers the iteration cycle. The variable G_{jm}^{meas} is the measured projected value of histogram j and bin m while $G_{jm}^{(i)}$ describes the projected values that were calculated from the iterated value $H_{jm}^{(i)}$, as given in Eq. (6.7). The iteration cycle is initialised with $H_{jm}^{(0)} = 1$. The actual H_{jm} -values representing the distribution are determined by comparison of the calculated projected values $G_{jm}^{(i)}$ to the measured values G_{jm}^{meas} . Once all H -multipliers were iteratively determined, the ρ_ν of each polygon can be calculated. Assigning each function value ρ_ν to the corresponding polygon of area F_ν gives a reconstruction of the primary distribution.

6.1.2 Implementation of image reconstruction

The introduced procedure for image reconstruction was implemented using Matlab. A brief description of the developed reconstruction routine will be presented here. The starting point for the reconstruction are the measured profiles of the distribution. The profiles and the known transfer matrices serve as input variables for the reconstruction algorithm.

Step 1: Generation of histogram data The first step is to calculate the histogram of each measured profile. The number of bins can be chosen individually, but is required to be equal for all histograms. The outer bin boundaries and the boundary of the projection have to coincide. Then, the projected intensity values can be calculated for each bin. For each bin, the boundaries and the G_{jm}^{meas} are transferred to the next steps.

Step 2: Calculation of polygon areas This routine calculates the intersections between the bin boundaries. The intersections need to be known to find the smallest polygons formed by the bins.

The calculation procedure is illustrated in Fig. 6.4. First, all bin boundaries given by Step 1 have to be back-transformed using the inverse of the rotation matrix. Afterwards, two histograms are chosen and all intersections between the back-transformed bin boundaries of these histograms are calculated. The intersections form a set of tetragons, as can be seen in part a) of Fig. 6.4. All tetragons are saved as a list of all four coordinates corresponding to each tetragon's vertices.

The back-transformed limits of a third histogram are included and checked for intersections with the existing bin boundaries, as shown in Fig. 6.4 b). Depending on the position and orientation of the bin boundaries, the primal tetragons can be divided into smaller polygons having a different number of vertices. Only intersections and polygons that lie within the outer limits of all histograms are included. All other intersections and polygons are neglected, see Fig. 6.4 c) and d). The list of polygons is expanded such that existing polygons that were divided are replaced by the newly found polygons. Therefore, the list of polygons only contains the coordinates of the vertices of the smallest polygons. This procedure is continued until all histograms have been included. Now, a list of all existing smallest polygons lying within the overall limits of all back-transformed histograms is generated. Finally, the area F_ν enclosed in each polygon is calculated from its coordinates. Additionally, a list containing all indices of the bins building each polygon is generated. Both the list of polygon areas and the indices corresponding to a polygon are sorted by polygon indices.

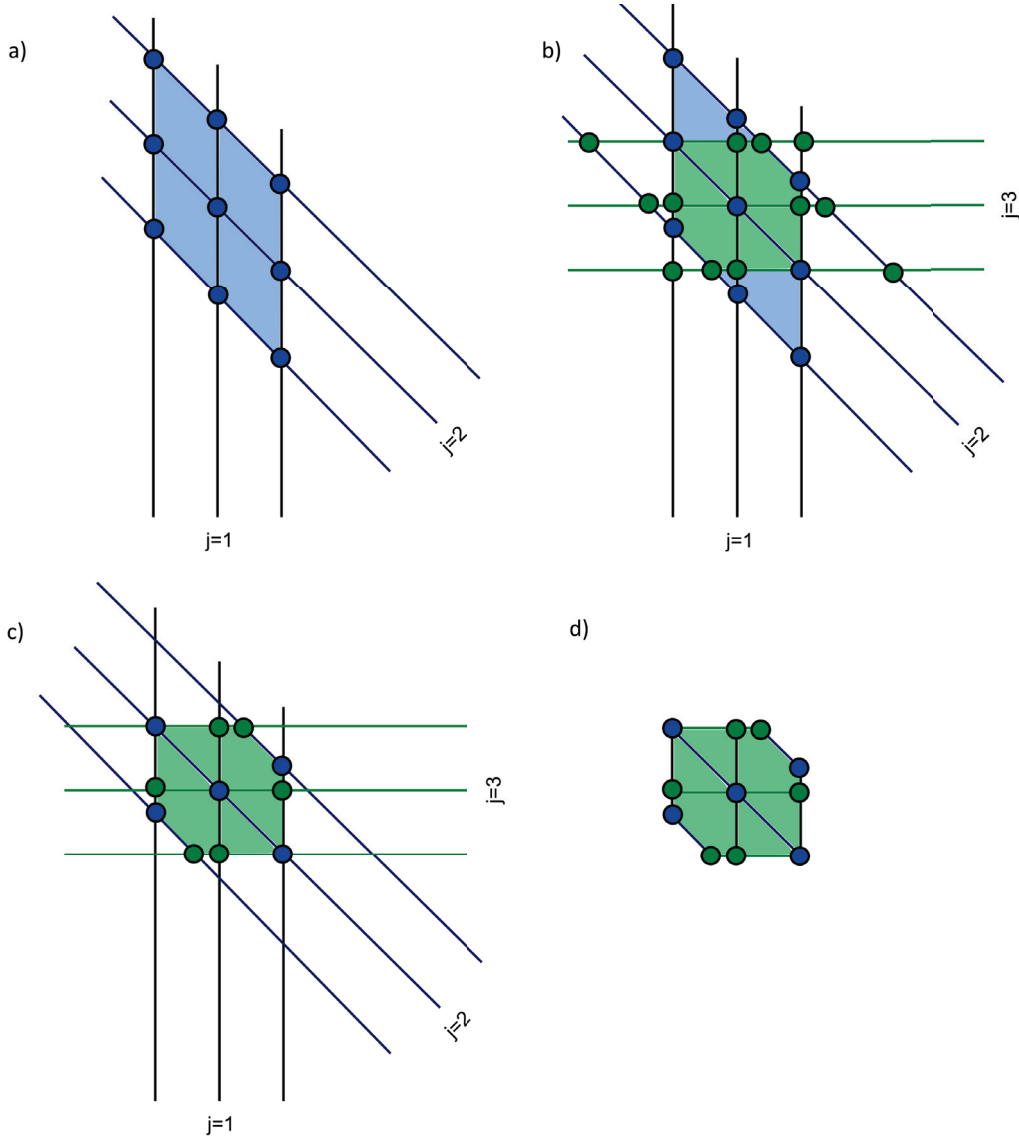


Figure 6.4: Schematic drawing of the procedure to calculate the intersections between the back-transformed bin boundaries of the histograms. First, all intersections between two histograms are calculated. As can be seen from a), these form a set of tetragons. In step b) a third histogram is included and again all intersections are calculated. Intersections and polygons lying within the overall bin boundaries are kept in c). Step d) shows the relevant intersections and the resulting polygons.

Step 3: H_{jm} iteration cycle This part of the algorithm performs the iteration cycle with the purpose to determine all H_{jm} and ρ_ν . The iteration rule was introduced in Eqs. (6.6) and (6.7). Here, the measured projected values G_{jm}^{meas} , the list of bin indices per polygon and the list of F_ν are used. The iteration is terminated by a stopping criterion indicating convergence and the final H_{jm} -multipliers are used to calculate all ρ_ν .

Step 4: Reconstruction of the initial distribution The function values ρ_ν determined by the previous step are assigned to the centre coordinates of each polygon in order to reconstruct the initial distribution. This allows for a graphical representation of the reconstructed distribution.

6.1.3 Testing the reconstruction algorithm

The introduced algorithm was tested by the reconstruction of a defined distribution. For that purpose different types of model distributions were used. Since the reconstruction will be applied to phase space distributions in Section 6.2, the model distributions were created on the basis of expected ideal shapes of phase space distributions: A normal distributed input and a distribution consisting of three partially overlapping normal distributions of different sizes. Both distributions were considered in a (x, x') -coordinate system. A parametric description of the normal distribution was realised using the emittance and the Twiss-parameters in analogy to the phase space characterisation introduced in Section 2. The function values ρ are referred to as particle density in the following. All parameters in plots and tables are given in arbitrary units. The model distributions were rotated to achieve different view angles. For each case, the view angles were chosen in equidistant steps $\Delta\varphi$ covering an effective range of 180° , namely $\varphi = 0^\circ \dots (180 - \Delta\varphi)$. The reconstruction was compared to the model distribution to evaluate the quality of the reconstruction. The reconstruction of both distributions will be presented for a number of histograms between three and ten, each combined with 25 bins. For the normal distribution, the emittance and Twiss-parameters of model and reconstructed distribution provide an additional possibility of comparison and evaluation. These parameters were compared as a function of the number of included bins.

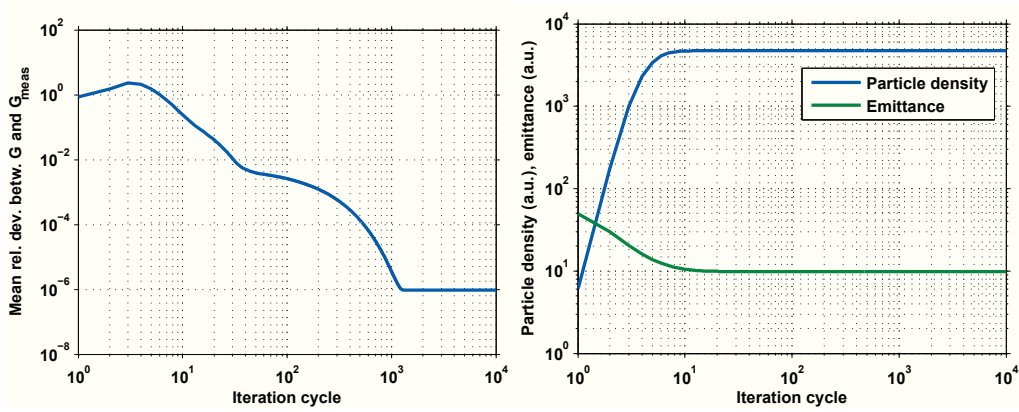
Convergence of the iteration

Numerical simulations require evaluation by convergence studies to verify both the appropriateness of the chosen algorithm and reliability of the simulation results. This section briefly examines the convergence behaviour of the developed algorithm.

The mean deviation between projected values from iteration and measurement is the essential parameter for the given application. The deviation values are calculated according to

$$dG = \frac{1}{J \cdot M} \sum_{j=1}^J \sum_{m=1}^M \frac{|G_{jm}^{(i)} - G_{jm}^{\text{meas}}|}{G_{jm}^{\text{meas}}}, \quad (6.8)$$

where J and M are the number of projections and bins. The deviation is plotted as a function of the iteration cycle. In addition, the development of the overall particle density and the emittance are examined. The convergence study was performed using a normal distribution as input. The reconstruction was started from five histograms of ten bins each. The results can be seen in Fig. 6.5. The overall particle density as well as the emittance of the distribution need less than 100 iteration cycles to reach convergence while the projected value deviation needs approximately 1,000 iterations to be fully convergent. This number of iterations varies for different numbers of histograms and bins. However, the behaviour shown in Fig. 6.5 is similar for all settings. This indicates the possibility to define stopping criteria for the iteration by setting precision limits of the projected value, the emittance and the particle density. In addition, a visual check of the convergence criterion is a requirement for high precision tomographic measurements.



(a) Development of the mean deviation between the iterated and the measured projected values.

(b) Development of overall density and emittance.

Figure 6.5: Convergence studies performed for five histograms and ten bins of a normal distribution. The development of three different parameters during the iteration cycle is examined.

Reconstruction of a normal distribution

A normal distribution of 500,000 particles defined by its centre and semi-axes was used as a model particle distribution. The emittance and Twiss-parameters of the model can be found in Tab.6.1. The number of bins used for the reconstruction influences the accuracy of the reconstruction since a refined binning provides smaller polygons, resulting in a refined scanning and a more accurate estimation of the model. To examine this dependence, the reconstruction was repeatedly performed for three histograms and a number of bins between five and 50. Iteration was continued until the deviation of projected values reached a value $\leq 1 \times 10^{-6}$. Fig.6.7 shows the reconstructed emittance and the iteration time as a function of the number of bins. Three histograms were used here.

The reconstruction overestimates the emittance for a small number of bins, which is expected to be caused by the computed particle density being assigned to the centre coordinates of the polygons, as described before. The emittance is calculated from the variances and covariances of the polygon's centre coordinates, see Section 2.2, weighted by the corresponding particle density. Assuming a polygon at the outer margin of the model distribution being only partly covered with particle intensity, the polygon's centre may be

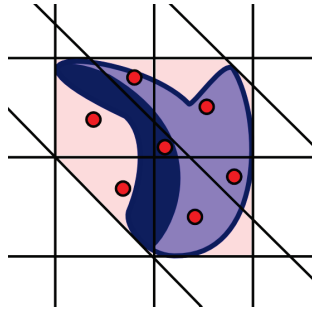


Figure 6.6: Overestimation of emittance due to the reconstructed ρ being used as weighting factors for the centre coordinates of the polygons.

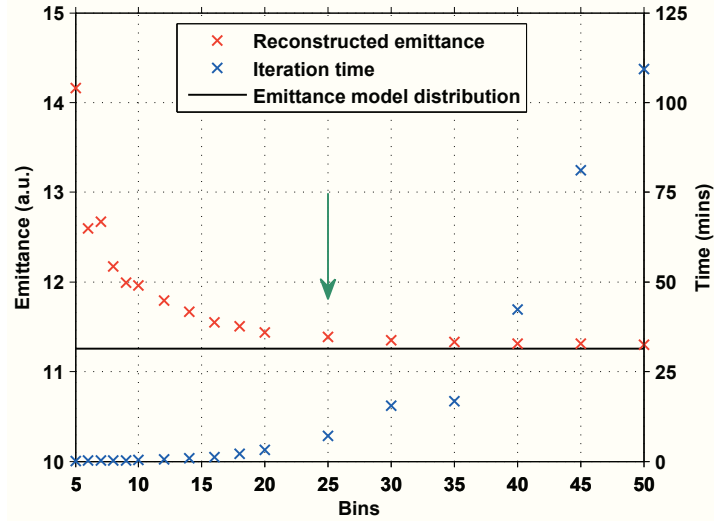


Figure 6.7: Reconstructed emittance and required iteration time as a function of the number of bins. Three histograms were used. The reconstructed emittance values are higher than the emittance of the model distribution for a small number of bins. Convergence of the reconstructed emittance towards the expected value is observed for a larger number of bins. The iteration time increases exponentially with the number of bins. 25 bins (green arrow) provide a good trade-off between accuracy and iteration time.

located outside the actual distribution. A high intensity included in the covered polygon area implies a high weighting factor for the corresponding centre coordinates, leading to an increase of the calculated emittance. The effect is explained in Fig. 6.6 schematically. The model distribution (blue) is approximated by the red shaded polygons formed by three histograms of two bins each. The polygons only partly contain intensity and some of the centre coordinates (red dots) lie outside the distribution. The high-intensity region indicated by a dark blue colour mainly falls within the two leftmost polygons. Hence, the centres of these polygons are highly weighted and exceedingly contribute to the emittance. The more bins included in the reconstruction the smaller the polygons and the better the approximation of the model and the reconstructed emittance converges towards the expected value. Due to the exponential increase in iteration time, the choice of binning is a compromise between computational time and accuracy. As the overestimation of the emittance is $< 2\%$ for a seven minute calculation, the number of bins was limited to 25 for all following reconstructions and studies.

Taking this limitation into account, a symmetric reconstruction error was deduced from the difference between the model and reconstructed parameters. The procedure was repeated for ten histograms and 25 bins and a summary of all parameters can be found in Tab. 6.1. The accuracy of the reconstruction is 1.2% for three histograms. Using ten histograms further increases the accuracy to below 0.6% . Both are excellent results when compared to a typical emittance error of about $\pm 10\%$ resulting from the fitting routine applied to quadrupole scan data, see results in Sections 5.1.2 and 5.2.2. A visual comparison of model and reconstruction is given in Fig. 6.8. Model and reconstruction are almost identical in shape and orientation. The difference plot in Fig. 6.8c reveals small deviations in density of 4% maximum. Both the parameters and plots given in Tab. 6.1 and Fig. 6.8 clarify that the reconstruction algorithm is able to reconstruct a simple model distribution even from a small number of histograms.

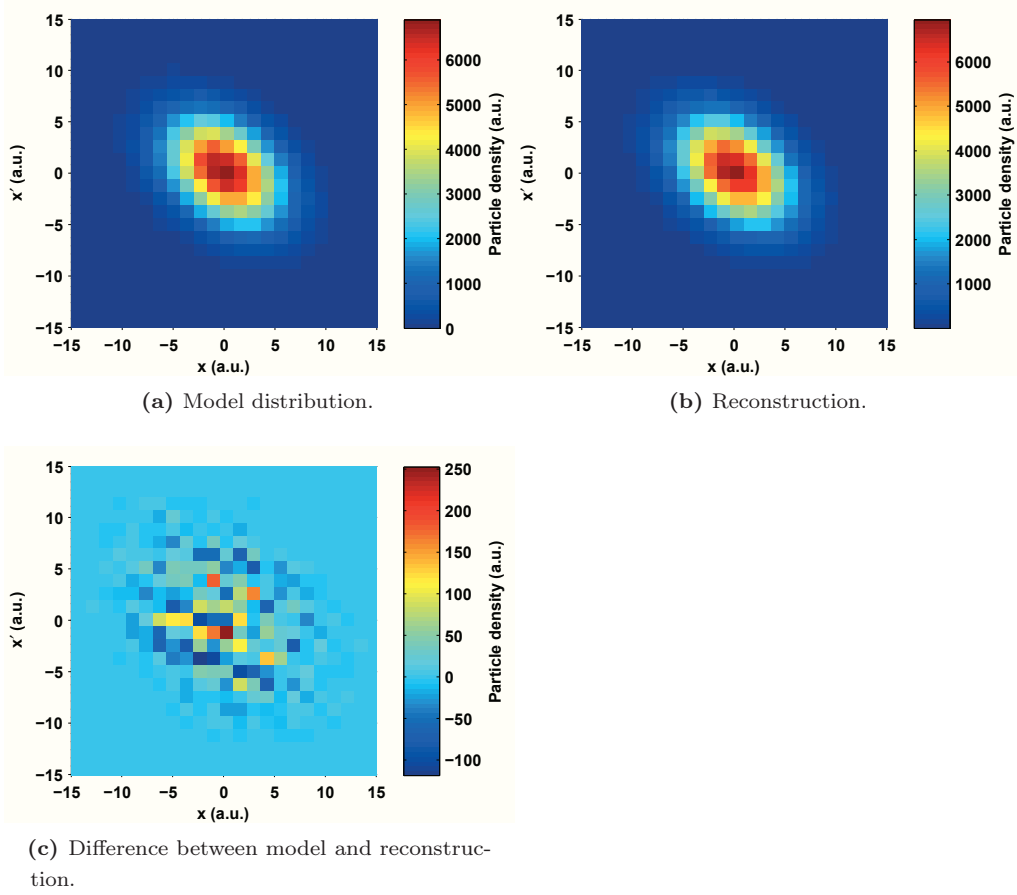


Figure 6.8: Reconstruction of a normal distribution from three histograms and 25 bins.

Table 6.1: Comparison of the emittance and Twiss-parameters of the initial normal distribution and the reconstructed distribution. The number of histograms was $J = 3$ and $J = 10$ each with a number of $M = 25$ bins.

		ε (a.u.)	β (a.u.)	α
Model		11.26	1.16	0.39
Reconstruction	$M = 25, J = 3$	11.39 ± 0.13	$1.16 \pm 2 \times 10^{-3}$	$0.38 \pm 5 \times 10^{-3}$
	$M = 25, J = 10$	11.33 ± 0.07	$1.16 \pm 8 \times 10^{-4}$	$0.39 \pm 2 \times 10^{-3}$

Reconstruction of three partially overlapping normal distributions

A model distribution consisting of three partially overlapping normal distributions of different size and orientation was used to allow for evaluation of the reconstruction quality for irregular distributions. The central distribution was produced using 500,000 particles. The smaller distributions contain a particle number scaled to the occupied area such that the particle density is comparable for each distribution. Visual evaluation of the reconstruction can be performed on the basis of Fig. 6.9, which contains the model, the reconstruction from five histograms and a difference plot. Since the model distribution is more complex than the normal distribution considered before, more than three histograms are needed to deliver acceptable reconstruction results. Five histograms are necessary to

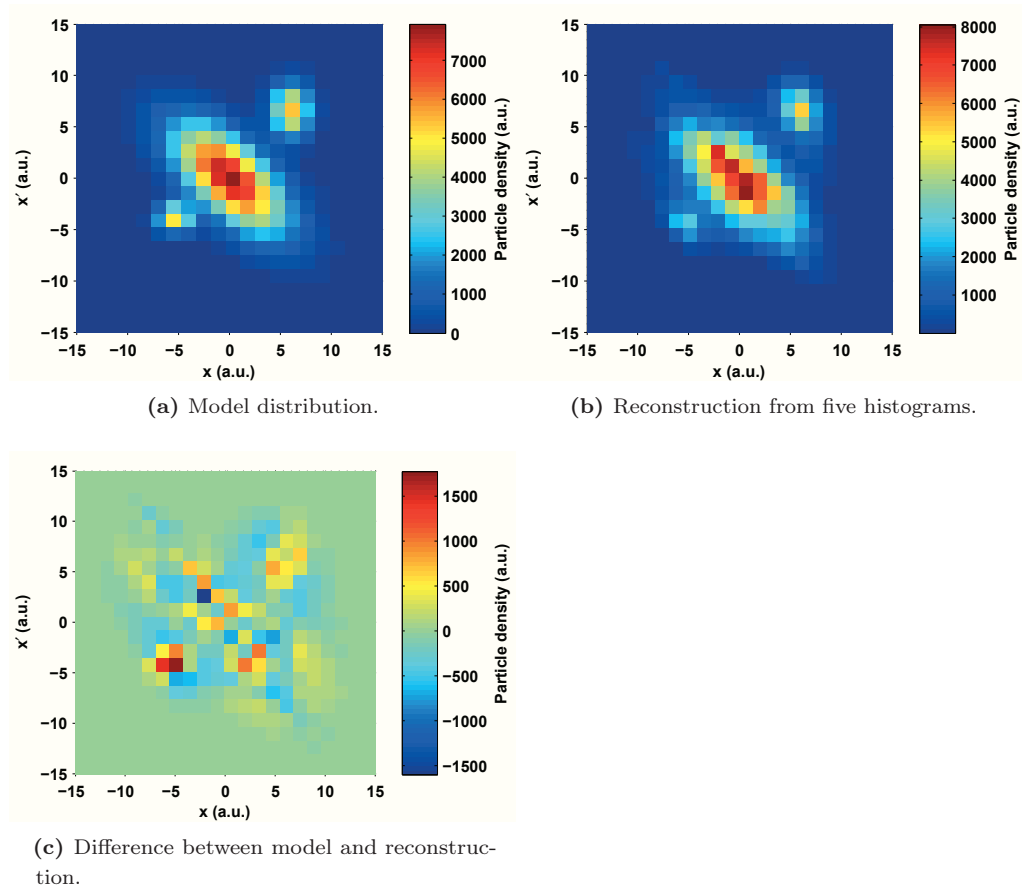


Figure 6.9: Reconstruction of three partly overlapping normal distributions from five histograms and 25 bins.

successfully reconstruct the threefold structure of the distribution, see Fig. 6.9b. From Fig. 6.9c, the difference in particle density is found to be up to 20%. Results from reconstruction of three and ten histograms are presented in Appendix C.

Effects of non-equidistantly distributed projection angles

A random angle deviation of up to $\pm 20\%$ was individually applied to each of ten equidistant projection angles such that each angle achieves a different percentage deviation. The reconstruction of the normal distribution was performed using 25 bins, the ten deviating histograms and their corresponding rotation matrices. 50 different sets were reconstructed due to the random factor in the chosen histograms. The mean and standard deviation of the emittance and Twiss-parameters are summarised in Tab. 6.2.

Table 6.2: Emittance and Twiss-parameters determined from reconstruction using non-equidistant sets of $J = 10$ histograms and $M = 25$ bins. The presented values are the mean and standard deviation calculated from 50 runs.

	ε (a.u.)	β (a.u.)	α
$M = 25, J = 10$	11.51 ± 0.43	1.15 ± 0.02	0.37 ± 0.03

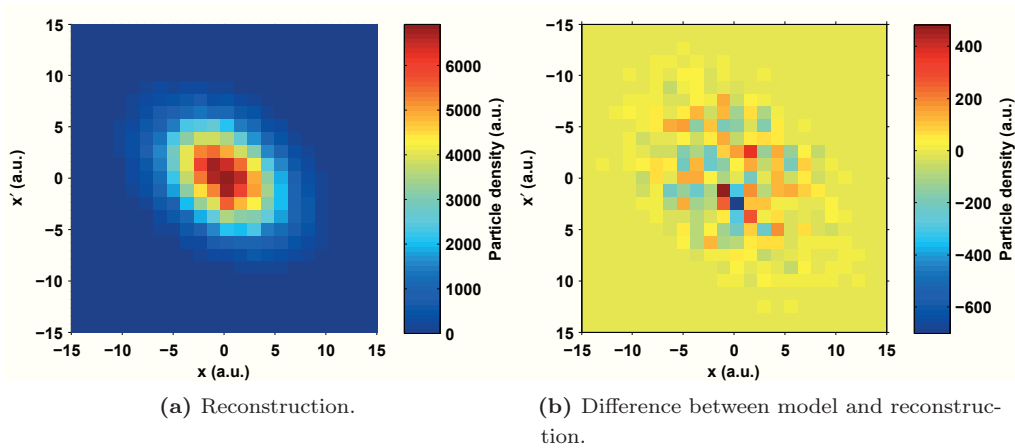


Figure 6.10: Reconstruction of a normal distribution using a non-equidistant set of $J = 10$ projections and $M = 25$ bins.

The angle deviation causes overestimation of the emittance by 2% with respect to the model and by 1% with respect to reconstruction from three histograms. Both the emittance and the Twiss-parameters of the model and the deviated reconstruction are identical within the range of errors. Fig. 6.10 shows the example yielding the highest emittance value of 12.98. Density deviations below 10% were observed.

Conclusion

It was shown that the developed algorithm provides convergence depending on the number of projections and bins. An additional visual check of the convergence of the iteration is recommended for application to measurement analysis. The reconstruction of the model distributions showed good results for adequate sets of projection angles. The more complex the distribution, the more projections are required to be known in order to allow for a reliable reconstruction. A smooth distribution, as the normal distribution, can be reconstructed from only three projections with an emittance accuracy of 1%. The more complex distribution required at least five view angles to recover its inner structure. For practical application to particle beams, a minimum number of five histograms are adequate to unveil possible irregularities in phase space. Examination of the influence of view angles and their distribution proved the algorithm to be robust against small deviations of the projection angles. Here, the mean emittance was found to be 2% larger than the model emittance.

6.2 Phase space tomography

As introduced in Chapter 2, the phase space ellipse rotates along the beamline and transverse beam profiles can be observed from different view angles. Hence, the principle of tomography can be applied to particle beams. Phase space tomography provides a possibility to reconstruct the transverse phase space distribution from a number of transverse beam profile measurements. Fig. 6.11 explains the idea of phase space tomography for the horizontal plane. Reconstruction in vertical direction works accordingly. The 2D projection of the incoming 3D bunch distribution is observed on a screen placed in the

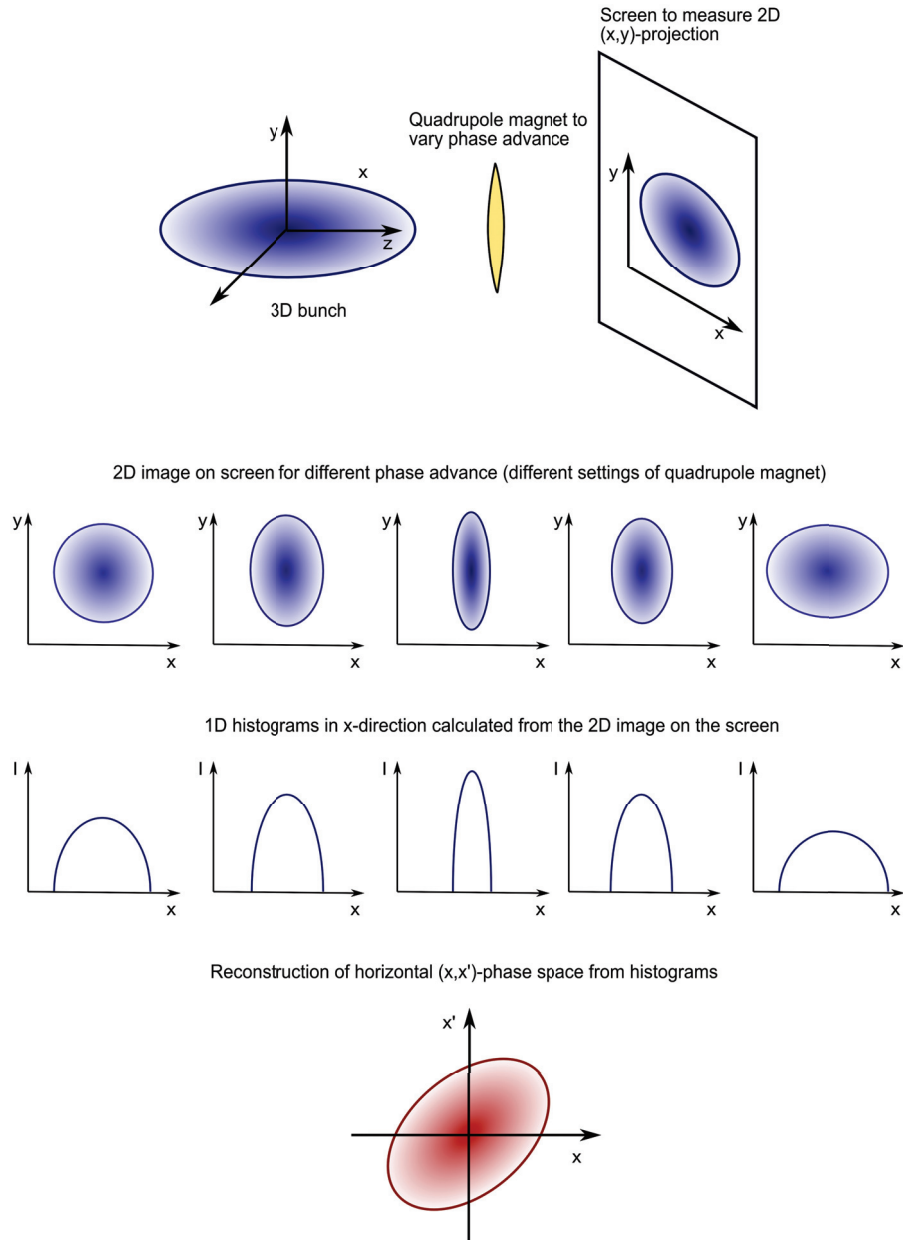


Figure 6.11: Working principle of phase space tomography in horizontal direction. The measurement setup consists of a quadrupole magnet and a screen separated by a drift section. The 3D distribution of the bunch is captured on the screen, leading to a 2D image of the beam. Different projections of the distribution are taken for different settings of the quadrupole magnet. The histograms calculated from the 2D projections are used to reconstruct the horizontal phase space indicated in red.

beamline. Such a (x, y) -distribution is taken for different settings of a quadrupole magnet and hence projection angles of the (x, x') -phase space. From the images on the screen 1D histograms in x -direction are calculated. The distribution in (x, x') -phase space is reconstructed using these histograms. The emittance and the Twiss-parameters may be directly deduced from the reconstructed data using the density-weighted variances and covariances of the polygon's centre coordinates.

A tomographic reconstruction has essential advantages compared to the conventional

quadrupole scan to find the emittance and Twiss-parameters. Due to the emittance calculation based on the definition of the beam matrix, see Section 3.2, the quadrupole scan assumes an ellipsoidal distribution valid only for Gaussian beams. In contrast, a tomographic reconstruction yields the actual particle distribution without any assumptions. Therefore, tomography is a powerful tool capable of reconstructing irregularities and the actual shape of the phase space distribution.

As introduced in Section 6.1, the knowledge of the transformation between views as well as equidistantly spaced angles covering 180° are required. The transformation of the phase space distribution is determined by the optical elements and can be described by the beam transfer matrix. The transfer matrix can be expressed as the product of matrices deduced from the beamline elements as well as in terms of Twiss-parameters and the betatron phase advance Ψ according to [64]

$$M = \begin{bmatrix} \sqrt{\frac{\beta_1}{\beta_0}} (\cos \Psi + \alpha_0 \sin \Psi) & \sqrt{\beta_1 \beta_0} \sin \Psi \\ \frac{1}{\sqrt{\beta_1 \beta_0}} ((\alpha_0 - \alpha_1) \cos \Psi - (1 + \alpha_0 \alpha_1) \sin \Psi) & \sqrt{\frac{\beta_0}{\beta_1}} (\cos \Psi - \alpha_1 \sin \Psi) \end{bmatrix}. \quad (6.9)$$

The sub-indices 0 and 1 indicate the Twiss-parameters at the start of the beamline and a position of measurement in the beamline. Ψ is the phase advance between these positions. The phase advance gives a measure of the phase space projection angle. Using the transfer matrix calculated from the optical elements and Eq. (6.9), the phase advance can be calculated from the matrix element m_{12} as follows

$$\Psi = \arcsin \frac{m_{12}}{\sqrt{\beta_1 \beta_0}}. \quad (6.10)$$

The phase advance is given as a function of β_0 and β_1 , with β_1 in turn depending on the initial Twiss-parameters and the transfer matrix $\beta_1 = f(\beta_0, \alpha_0, M)$ as given in [64]

$$\begin{bmatrix} \beta_1 \\ \alpha_1 \\ \gamma_1 \end{bmatrix} = \begin{bmatrix} m_{11}^2 & -m_{11}m_{12} & m_{12}^2 \\ -m_{11}m_{21} & m_{11}m_{22} + m_{12}m_{21} & -m_{22}m_{12} \\ m_{21}^2 & -m_{22}m_{21} & m_{22}^2 \end{bmatrix} \cdot \begin{bmatrix} \beta_0 \\ \alpha_0 \\ \gamma_0 \end{bmatrix}. \quad (6.11)$$

Hence, the view angles can be approximated from known beam optics and known Twiss-parameters at the start of the beamline.

6.2.1 Application of the quadrupole scan for phase space tomography

A change of the phase advance can be achieved by either measuring at different locations in the beamline or by taking measurements at a fixed location for a changed beam optics. Due to its simplicity and availability in existing accelerator structures, a quadrupole magnet followed by a drift section is the setup of choice for the phase space tomography measurements in this work. The quadrupole magnet is used to change the phase advance and all the projections are measured at the same location in the beamline.

An essential advantage of all projections taken on the same screen is the general possibility of combining phase space tomography and slice diagnostics. A tomographic reconstruction of the phase space distribution for individual longitudinal slices can be achieved [65, 66]. Such time-resolved tomographic measurements were not performed within this work due to limitations given by the slice diagnostics setup. The drawback of this setup follows

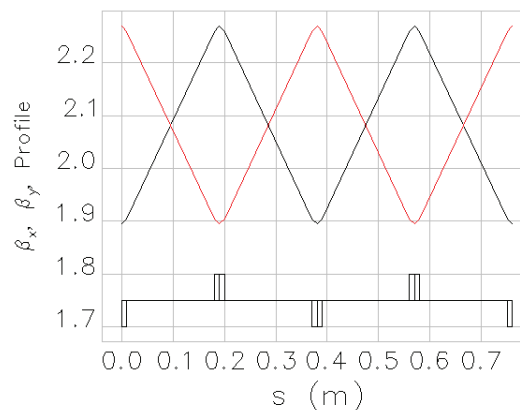


Figure 6.12: Periodic β -functions within a two-cell FODO lattice simulated with ELEGANT.

from the previous considerations based on Eqs. (6.10) and (6.11). The phase advance depends on the Twiss-parameters at the scanning quadrupole magnet $\Psi = f(\beta_0, \alpha_0, M)$. Since these are usually unknown in the first place, the view angle cannot be calculated until these parameters have been determined in an intermediate step.

Periodical FODO structures consisting of focusing (F) and defocusing (D) quadrupole magnets separated by drift sections (O) are commonly used as magnetic setups for phase space tomography sections [67, 68]. These structures have the essential advantage of the phase advance per cell being adjustable by the strength of the quadrupole magnets. For a matched FODO lattice as presented in Fig. 6.12, the β -functions at a defined position in the FODO cell are equal for each of the following cells. According to Eq. (6.10), a periodic magnet optic and β -function provide equal phase advance between defined positions in the FODO lattice. Placing measurement screens at locations of equal β -functions within a multi-cell FODO lattice guarantees constant and known phase advance between the observed projections. Nonetheless, the space required for a FODO setup including a preceding matching section is not always available. Therefore, only the applied combination of a quadrupole magnet and drift section will be considered in the following sections.

Measurement procedure and preparation for analysis

The measurement procedure consists of a quadrupole scan including the measurement of a projection of the beam for each magnet setting. A wide range of strengths of the quadrupole magnet has to be scanned in small steps in order to allow for a large range of projection angles. Now, an appropriate set of projections has to be found from the multitude of measurements. The measured data can be analysed using the conventional procedure for a quadrupole scan described in Section 3.2 to determine the Twiss-parameters at the quadrupole magnet. Then, the phase advance for each setting can be calculated and a set of projections meeting the angle requirements can be selected.

Testing the procedure: Phase space tomography from simulated data

The analysis of the quadrupole scan gives a possibility to evaluate the tomographic reconstruction using the beam transfer matrix for back-transformation of the bin boundaries

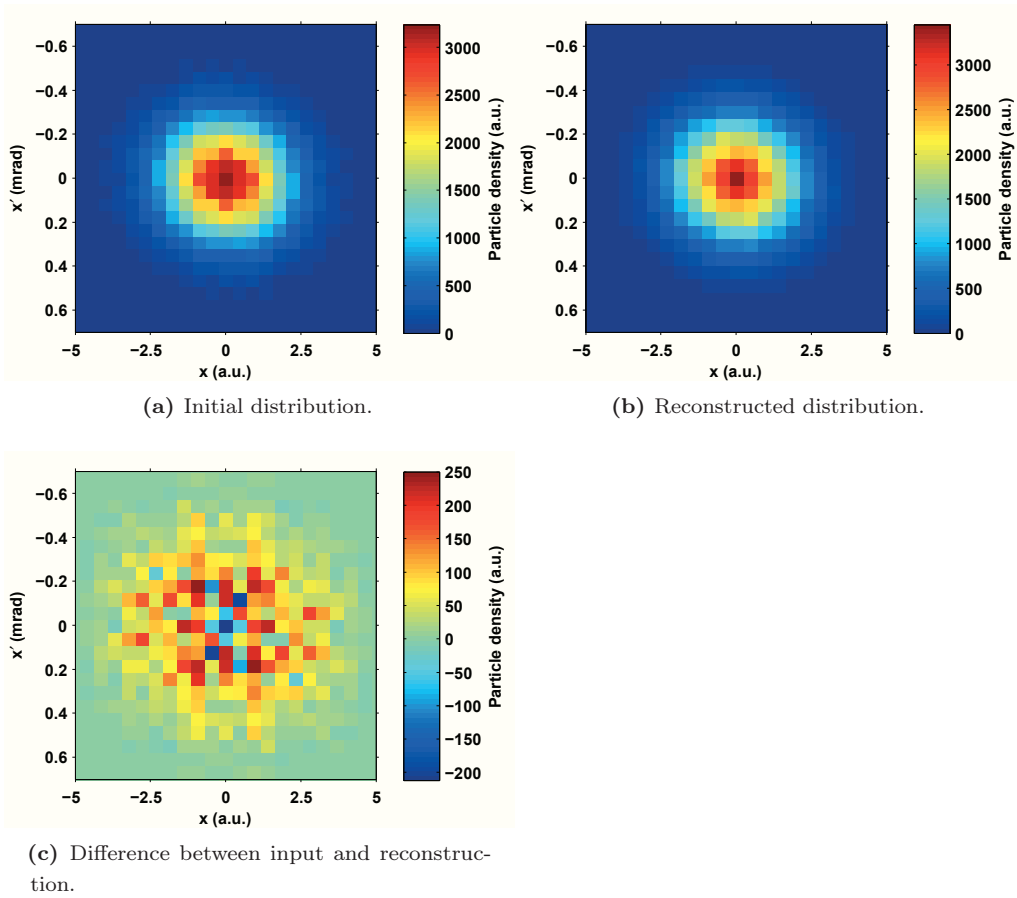


Figure 6.13: Evaluation of the phase space tomography procedure by reconstruction of the initial phase space distribution from simulated projections.

according to Step 2 in Section 6.1.2 and the procedure to select appropriate projections. The found emittance and Twiss-parameters can be used to initialise a simulation of the complete scanning procedure. Six appropriate projections were chosen for reconstruction of the Gaussian input distribution at the quadrupole magnet. The input distribution, the reconstruction and a difference plot are presented in Fig. 6.13. The distributions are very similar in form and size, as can also be seen from the difference plot Fig. 6.13c. Here, a variation of the particle density between model and reconstruction below 10% is observed. The emittance and Twiss-parameters of the distributions are compared in Tab. 6.3. The difference of emittance values is about 2% and the Twiss-parameters differ by < 1%. These results clearly show that the procedure delivers accurate results and is therefore suitable to apply for phase space reconstruction from measured data.

Table 6.3: Emittance and Twiss-parameters calculated from the quadrupole scan data compared to the results achieved from tomographic reconstruction using the ideal set of simulated data.

	ε_n (mm mrad)	β (m)	α
Quadrupole scan	25.22 ± 1.95	7.74 ± 0.11	0.05 ± 0.02
Tomography (simulation, ideal set)	24.82	7.70	0.05

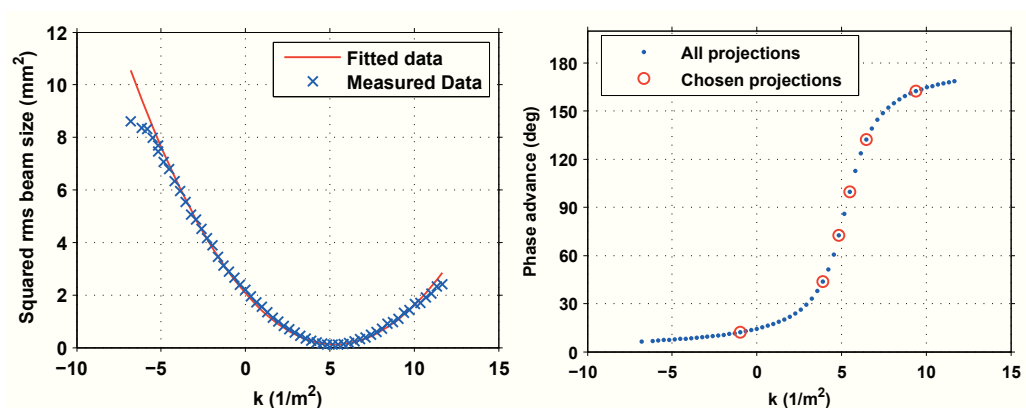
This reconstruction from simulated data served as a proof of principle on the one hand. Moreover, these results will be subsequently used for comparison with tomographic measurements presented in Section 6.3. Therefore, the simulation was initialised anticipating the Twiss-parameters and emittance determined by the actual quadrupole scan measurement presented in Fig. 6.14.

6.3 Phase space tomography at the BESSY II pre-injector linac

Tomographic measurements using the developed reconstruction algorithm were performed within the commissioning phase of the new 50 MeV pre-injector linac [69] of the BESSY II electron storage ring. The measurements were taken in the ‘Long Pulse Operation Mode’ providing bunch trains of 200 ns having a total charge of 2 nC. This corresponds to 100 bunches of 20 pC charge and ~ 20 ps length separated by 2 ns [69, 70]. A quadrupole scan was performed in the injection line to the synchrotron. The image of the beam was observed on a screen viewed by a CCD camera. All measurements were taken for the horizontal plane. The camera was triggered to the pulse train repetition rate of 10 Hz with an exposure time of 20 ms. Thus, the measured beam images represent an integration over one pulse train.

6.3.1 Data analysis procedure

The result of the quadrupole scan fitting procedure is presented in Fig. 6.14a. The emittance and Twiss-parameters at the scanning quadrupole magnet were determined from the fitted curve to $\varepsilon_n = 25.22$, $\beta = 7.74$ m, $\alpha = 0.05$. The calculated phase advance as a function of the magnet strength for all settings of the quadrupole magnet is presented in Fig. 6.14b. These results were used to pick an ideal set of six projections between



(a) Quadrupole scan fitting results. The β -function was estimated from the fitted data (red) and then used to calculate the phase advance.

(b) Calculated phase advance. The data points marked in red were included for tomographic reconstruction.

Figure 6.14: Squared rms beam size and phase advance as a function of the strength of the quadrupole magnet. The phase advance was calculated from the results of the quadrupole scan fitting routine.

Table 6.4: Strengths of the quadrupole magnet and calculated phase advance for the ideal set of projections.

Parameter						
$k \text{ (m}^{-2}\text{)}$	-1.0	3.9	4.9	5.5	6.5	9.1
$\Psi \text{ (}^\circ\text{)}$	12.2	43.7	72.4	99.8	132.3	162.4

12° and 162° with $\Delta\Psi = 30^\circ$. The phase advances corresponding to the ideal set of projections used for the reconstruction are indicated by the red circles in Fig. 6.14b.

Post-processing of the measured projections

Post-processing of the projections is necessary to achieve a reliable reconstruction of the phase space. The implemented data post-processing is briefly described.

The projections were optimised by the following steps:

- Check projections for saturation,
- perform background subtraction,
- set all intensity values below 1 % of the maximum intensity to zero,
- eliminate remaining separate intensity spikes.

The histograms were calculated from the optimised projections. Artefacts due to binning and intensity variation have to be avoided. Thus, more optimisation was applied:

- Apply linear interpolation between the given intensity values of projections,
- normalise histograms to the maximum overall histogram intensity.

Interpolation was required since the number of pixels in the horizontal direction of the saved image is limited, providing ‘pre-binned’ intensity profiles consisting of 659 values. Only the range of the profiles containing intensity is included for the binning procedure. Especially narrow profiles of a horizontally focused beam provide very few intensity values per bin, leading to uneven histograms when divided in 25 bins. Interpolation between the given intensity values had to be applied before binning in order to achieve smooth histograms. 100 interpolated steps were found to deliver good results.

6.3.2 Phase space reconstruction

The reconstructed phase space using the optimum set of projections according to Fig. 6.14b and 25 bins is presented in Fig. 6.15. This is a typical phase space distribution since the statistical fluctuations are averaged over 100 bunches. The normalised emittance calculated from this distribution is 24.88 mm mrad. The distribution clearly deviates from an ideal Gaussian beam and reveals asymmetries with a tail of low particle density. This confirms the expectations based on the asymmetric shape of various horizontal beam profiles observed during the commissioning phase [70]. The influence of the selected projections was estimated using varied sets of projections and their respective phase advance. Starting at the ideal set of histograms, a random deviation of projections, between ± 3 for the first and last and between ± 1 for the second to fifth view, was applied. The maximum deviation in phase advance was $\sim 15^\circ$. A total number of 50 reconstructions

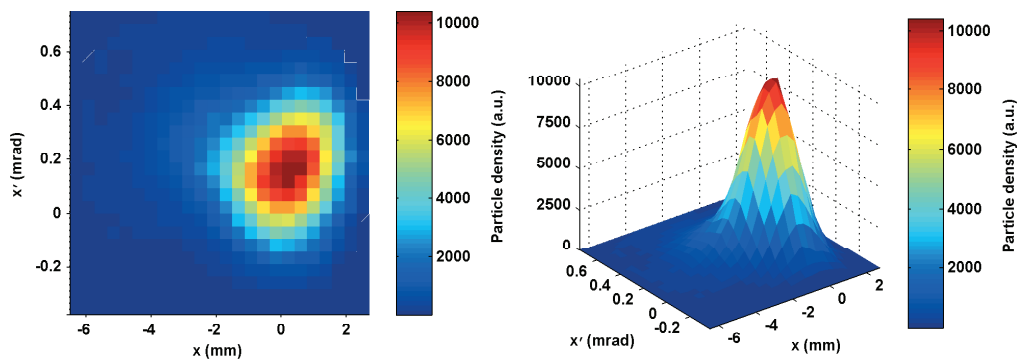


Figure 6.15: Reconstructed horizontal phase space distribution at the scanning quadrupole magnet. Six histograms of 25 bins each were used.

were computed, from which a mean emittance and a standard deviation were determined. This gives an estimation of the error induced to the reconstruction by the individual choice of projections. The procedure was repeated for both the reconstruction from the measured projections as well as from the simulated projections described before, using the same randomly determined deviations. Tab. 6.5 gives a summary of all emittance values and the Twiss-parameters that were determined as described. Additionally, the parameters calculated using the ideal set of projections are given, both for measured and simulated data. The results of the quadrupole scan analysis are included with errors resulting from the fitting procedure. All determined emittance values are in good agreement with the expectation of 25 mm mrad based on various quadrupole scan measurements performed during the optimisation phase [70]. Using the ideal set of projections, an emittance of 24.88 mm mrad was determined from measured projections and a value of 24.82 mm mrad from simulated data. The mean emittance determined from the non-equidistant measured projections is about 4 % higher than the emittance determined from the ideal set of measured data, reflecting the overestimation of emittance caused by angle deviation that was also observed in Section 6.1.3. The emittance from the ideal set lies within the error range of the deviated angle set. A similar behaviour was observed analysing the simulation data. Here, a deviation of 11 % between ideal and non-equidistant projections was found. The error range is small and the emittance determined from the ideal projections is not within the range of errors.

Table 6.5: Summary of the horizontal normalised emittance values and Twiss-parameters determined from the reconstructed phase space distribution. The parameters determined from measured and simulated data are given each for a reconstruction using the ideal set of projections and as mean values determined from deviated sets of projections. The results of the analysis of the quadrupole scan are included as well.

	ε_n (mm mrad)	β (m)	α
Quadrupole scan	25.22 ± 1.95	7.74 ± 0.11	0.05 ± 0.02
Tomography (simulation)	27.79 ± 0.05	7.79 ± 0.19	0.05 ± 0.01
Tomography (simulation, ideal set)	24.82	7.70	0.05
Tomography (measurement)	26.02 ± 2.43	8.53 ± 0.53	0.07 ± 0.10
Tomography (measurement, ideal set)	24.88	8.58	0.07

The emittance is assumed to be most accurately determined by the tomographic reconstruction using the measured data due to the asymmetry of the reconstructed distribution. Comparison of the Twiss-parameters in Tab. 6.3 shows good agreement for the tomography using simulated data and the quadrupole scan. The Twiss-parameters determined by tomography using measured data are higher than these values. The deviations of $\sim 10\%$ for β and $\sim 40\%$ for α are expected to be caused by the Gaussian beam assumption in the analysis of the quadrupole scan and the Gaussian input beam used for the simulation.

6.4 Conclusion of phase space tomography

The working principle of tomography and its application to phase space investigation were discussed in this section. A developed reconstruction algorithm based on MENT was presented. The highly accurate reconstruction of different model distributions showed the great potential of the algorithm. The implemented tomography tool was applied to reconstruct the horizontal phase space at the BESSY II pre-injector linac. Due to its complete independence of any assumptions on the electron distribution, the technique provides the unique possibility of reconstructing the real phase space distribution. At the pre-injector linac, tomography helped realise an asymmetry in the horizontal phase space which could be improved on. The observed transverse beam profiles now suggest a Gaussian beam and lower emittance values of 12 mm mrad were achieved changing the temperature of the linac [70]. Repeated application of phase space tomography is planned to support further optimisation of the machine.

Combination of the developed tomography tool with a slice diagnostics technique introduced in Chapter 4 is highly promising, yielding a detailed time-resolved and model-independent reconstruction of the transverse phase space.

7 Slice diagnostics for *BERLinPro*

The Berlin Energy Recovery Linac Project (*BERLinPro*) aims at the development of a demonstrator energy-recovery linac (ERL) delivering a high-current and low-emittance beam at a beam energy of 50 MeV [1]. An overview of *BERLinPro* is presented in Fig. 7.1. The development of a SRF-photoinjector as the electron source capable of delivering the required beam quality at an energy of ~ 2 MeV is part of the project. Within this framework, slice diagnostics measurements are required to fully characterise the phase space distribution in the electron injector and to adjust and control the emittance compensation. Achieving ≤ 1 mm mrad normalised emittance throughout the machine is one of the design goals. Ideally, the slice emittance measurements would be performed at different positions in the beamline: Downstream of the gun to examine the source properties and initialise the emittance compensation scheme, downstream of the merger to investigate the merger performance and downstream of the first return arc to verify the parameters for future user experiments. The relevant slice parameters for the compensation are not only the emittance in the horizontal and vertical plane but also the mean energy and energy spread [71].

In the first stage, slice emittance measurements are foreseen exclusively within the diagnostics beamline of the SRF-gun. A deflector cavity capable of horizontal and vertical deflection is currently under development at the Technische Universität (TU) Dortmund [33] within a collaborative research project of the Universität Rostock, the TU Dortmund and the Helmholtz-Zentrum Berlin (DoHRO). The deflector allows to determine all the required slice parameters making use of the principles explained in Sections 4.3 and 4.4. In addition, the tools developed for phase space tomography are planned to be used, both independently and in combination with the deflector.

The slice diagnostics for *BERLinPro* itself is planned using existing accelerator structures

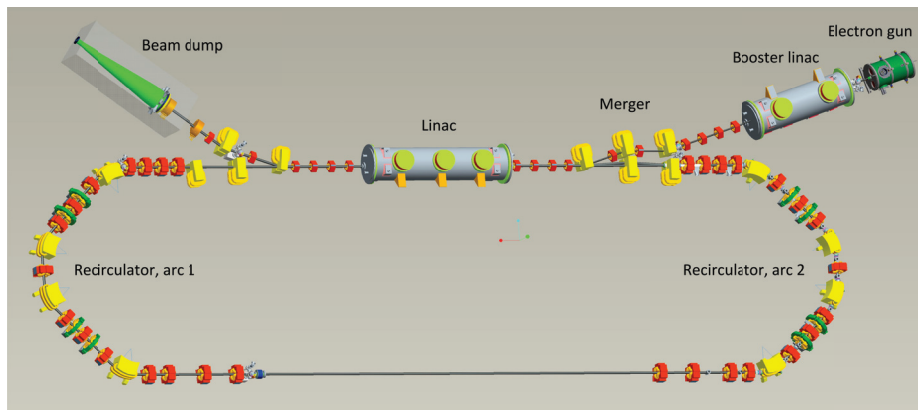


Figure 7.1: Schematic representation of *BERLinPro*. The electron beam is delivered by the injector consisting of a superconducting RF photogun delivering a beam energy of 2 MeV and the booster linac accelerating the beam to 6 MeV. A combination of three dipole magnets (merger) is used to inject the beam into the main linac. Two 180° arcs connected by a straight section bend the beam allowing for a second passage through the linac and recovery of the beam energy. The decelerated beam is then sent to the beam dump. The colour of the magnets indicates their type: yellow is for dipole magnets, red for quadrupole magnets and green for sextupole magnets.

by applying the zero-phasing technique in the early stages of the project. In doing so, only the vertical slice emittance can be determined due to the existing dipole magnets deflecting in horizontal direction. Moreover, the energy information per slice is not to be obtained with this setup. In the long term, another deflector will become necessary to obtain the complete information. This will be discussed in a more advanced stage of the project. The tomographic tools are planned to be used for supporting measurements, again as projected measurements and in combination with slice diagnostics.

7.1 Transverse deflecting cavity for the *BERLinPro* gun

This section introduces the deflector planned for the characterisation of the *BERLinPro* gun. The general idea of the design is described and the parameters required for the operation are estimated.

The single-cell deflector uses a TM_{110} -like mode and is designed to operate at 1.3 GHz, matching the RF frequency of *BERLinPro*. Due to a novel geometry developed by [33], the beam can be deflected in horizontal as well as in vertical direction, such that the slice emittance in both transverse planes can be measured. The novel geometry includes slitted cones on the inner end plates of the cylinder surrounding the beam pipe. These allow for two equivalent perpendicularly oriented polarisations to form according to the horizontal and vertical orientation of the slits. Plungers change the resonant frequency of the polarisations individually such that either horizontal or vertical deflection is enforced. Detailed information on the deflector can be found in [33]. The first design of the deflector presented in Fig. 7.2 served as a proof of principle verifying the simulated field distributions.

The development of an operational TCAV requires revision and further optimisation to precisely fit the beam parameters of the *BERLinPro* gun. Estimations of the deflector aperture and deflecting voltage will be discussed in the following sections using the parameters summarised in Tab. 7.1. Here, a range is given for the normalised emittance and β -function where the bracketed values present the worst case parameters. A large emittance of 3 mm mrad delivered by the gun without emittance compensation applied

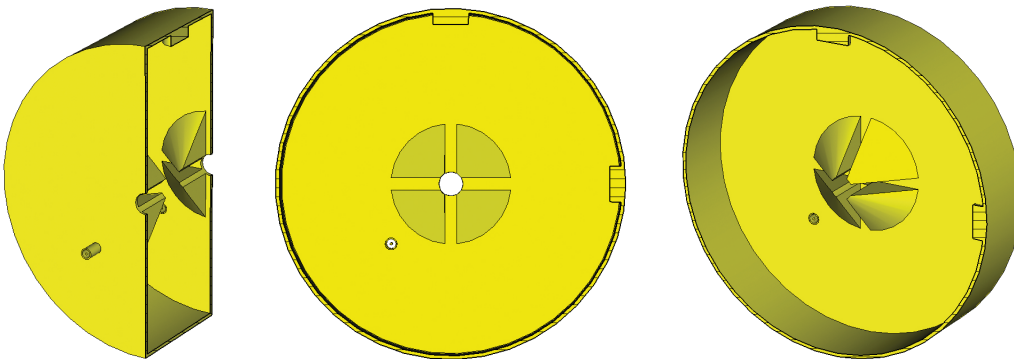


Figure 7.2: First model of the RF deflector designed by the TU Dortmund [33]. The double-slitted cones and two openings in the lateral area for the plungers and a smaller slot in the cylinder plate for the antenna are shown.

Table 7.1: Expected electron beam and deflector parameters [59, 71, 72, 73]. The transverse parameters of the beam are assumed to be equal for both planes.

Beam parameters				Deflector parameters			Drift	Slices
E (MeV)	ε_n (mm mrad)	β -function (m)	σ_t (ps)	f (GHz)	R_s (M Ω)	P_{RF} (kW)	d (m)	n_{slices}
≥ 2	1 (-3)	1 (-40)	5	1.3	3.5	10	2	10

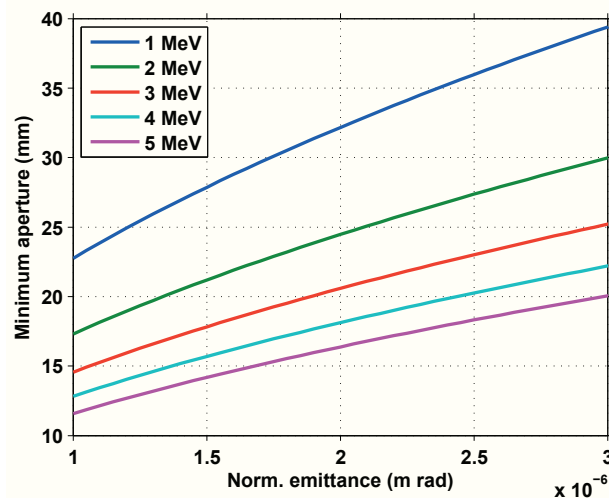
and a β -function up to 40 m occurring during the quadrupole scan were assumed. The number of longitudinal slices required to initialise the emittance compensation scheme was specified to ten by [71]. A shunt impedance of 3.5 M Ω was estimated by [59]. The peak RF power available from existing RF transmitters is 10 kW [72]. The parameter d is the estimated drift length between the deflector and the screen.

7.1.1 Aperture of the beam pipe

The aperture is an important geometric parameter of the deflector design. A small aperture is of advantage to achieve a high shunt impedance R_s and the lower limit of the aperture is given by the beam size since beam losses need to be prevented. The minimum diameter of the deflector aperture d_{tcav} was specified to be six times the transverse Gaussian beam size. Assuming a round beam, only the horizontal direction will be considered. The beam size depends on the β -function and the geometric emittance as introduced in Eq. (2.27). Hence, the aperture can be expressed as

$$d_{tcav} \geq 6 \sigma_x = 6 \sqrt{\beta_x \varepsilon_x} = 6 \sqrt{\beta_x \frac{\varepsilon_{x,n}}{\beta \gamma}}. \quad (7.1)$$

Fig. 7.3 shows the minimum aperture as a function of the normalised emittance for different beam energies and a β -function of 40 m. For beam energies ≥ 2 MeV and a maximum expected emittance of 3 mm mrad, a beam pipe diameter of 30 mm is found to

**Figure 7.3:** Minimum aperture as a function of the normalised emittance for different beam energies. A β -function of 40 m was assumed.

be appropriate and was set as a parameter for the design of the planned deflector.

7.1.2 Deflecting voltage requirements

An expression for the required deflecting voltage was introduced in Eq. (5.27). This relation is used to estimate the deflecting voltage for the parameters given in Tab. 7.1. The results are discussed subsequently.

Tab. 7.2 summarises the deflecting voltage required to analyse ten longitudinal slices for different beam energies, β -functions between 1 m and 40 m and the lowest and highest expected normalised emittance. The 2 MeV case corresponds to the energy delivered by the gun. The 6 MeV case is considered additionally to evaluate the suitability of the deflector for a possible application at positions downstream of the *BERLinPro* booster linac. The voltage needed to deflect a 2 MeV beam is 67 kV for $\beta = 1$ m and increases to 424 kV for $\beta = 40$ m. An increase of the emittance to 3 mm mrad leads to a voltage higher by a factor of $\sqrt{3}$. The voltage required for the 6 MeV beam of 1 mm mrad is approximately equal to the values estimated for the 2 MeV and 3 mm mrad case. The higher beam energy combined with the largest emittance requires 193 kV for 1 m β -function and 1.2 MV for 40 m. The voltage obtained by the 10 kW single-cell deflector, see specifications in Tab. 7.1, can be calculated from Eq. (5.30) to be 265 kV. Hence, the ten slices of the low energy and low emittance beam can be resolved for $\beta < 16$ m. The 2 MeV case of high emittance and the combination of 6 MeV and low emittance allow to keep the resolution condition for $\beta < 5$ m. A further restriction to 2 m is found for the high energy and high emittance case. Fig. 7.4 exemplarily shows a plot of the required voltage as a function of the beam energy and the β -function at the screen for a beam of 1 mm mrad normalised emittance.

An alternative approach is to directly deduce the number of slices for which the resolution criterion is fulfilled from the available peak RF power. Fig. 7.5 presents this relation for the beam energy and emittance combinations considered in Tab. 7.2. A medium β -function of 10 m was used for the calculation. The dotted black line marks the 10 kW available for the *BERLinPro* deflector, the grey lines indicate a range of medium and achievable peak RF power between (5 – 20) kW. The 10 kW deflector allows to analyse 12 slices for the low energy and low emittance beam. Seven slices are possible for both the low energy and high emittance as well as the high energy and low emittance case. Four slices may be analysed for the high energy and high emittance case.

In conclusion, the deflector characterised by the parameters in Tab. 7.1 (3.5 M Ω , 10 kW) is suitable for slice emittance measurements downstream of the gun. The resolution

Table 7.2: Required deflecting voltage in kV calculated according to Eq. (5.27) using the parameters given in Tab. 7.1. The cells coloured in grey indicate a voltage higher than the maximum voltage of 265 kV possible with the parameters $R_s = 3.5$ M Ω and $P_{\text{RF}} = 10$ kW. The green colour stands for achievable voltages.

		2 MeV		6 MeV	
		$\varepsilon_{y,n}$ (mm mrad)		$\varepsilon_{y,n}$ (mm mrad)	
		1	3	1	3
β (m)	1	67	116	111	193
	10	213	368	352	609
	40	424	736	703	1,218

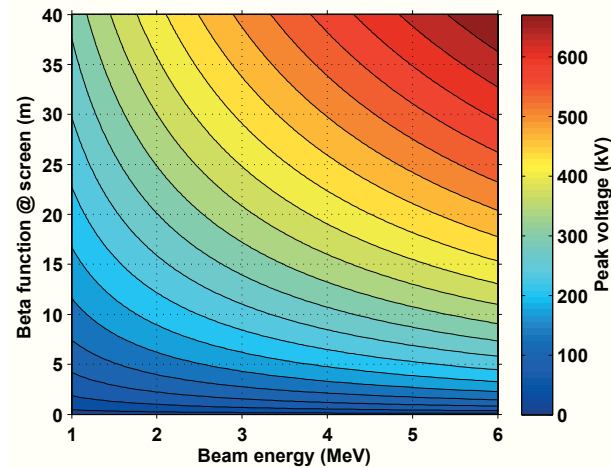


Figure 7.4: Required deflector voltage as a function of the beam energy and the β -function at the screen for a normalised emittance of 1 mm mrad.

criterion is fulfilled for at least ten slices for a low emittance and a β -function below 16 m. An uncompensated emittance of 3 mm mrad lowers the number of slices to seven, possibly still providing enough information to initialise compensation and achieve a lower emittance, which in turn optimises the resolution. Concerning the application of the deflector for measurements downstream of the booster linac at 6 MeV beam energy, one finds a slightly reduced resolution that might be considered sufficient for the very first measurements. Here as well, seven slices can be analysed provided both β and the emittance are low. Hence, the beam optics has to be optimised such that β stays low during the scan maintaining a high resolution. These restrictions on the resolution clarify the general need of a higher deflecting voltage with regard to future implementation of a TCAV in high energy sections of BERLinPro. Options to increase the voltage were introduced in Section 5.3, one of which is a multi-cell deflector having an increased R_s . Maintaining the assumed 10 kW, a shunt impedance doubled to 7 M Ω allows to analyse

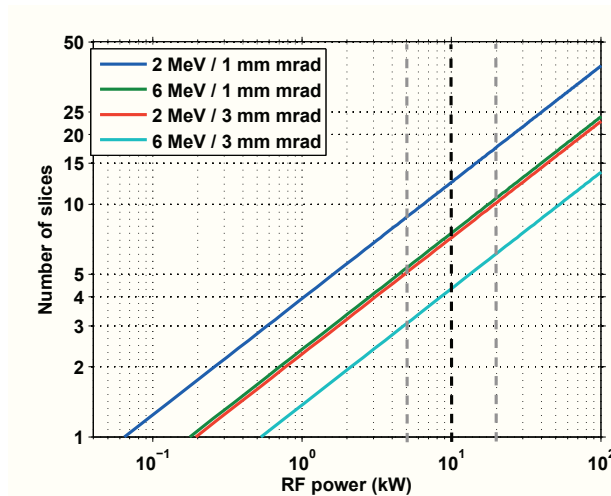


Figure 7.5: Number of slices to be analysed within the resolution as a function of the peak RF power. The curves for different beam energies and normalised emittances are included. A medium β -function of 10 m was assumed.

ten slices of a 6 MeV and 1 mm mrad beam while an emittance of 3 mm mrad requires 20 M Ω , both with $\beta = 10$ m. A combination of a multi-cell design and an increased peak RF power is promising for high-resolution measurements downstream of the booster linac, allowing to sufficiently deflect beams of larger emittance and tolerating higher β -functions at the screen.

8 Summary

The objective of this work was to build up the competence to design and operate slice diagnostic systems for future high-brightness electron sources and single-pass machines, particularly regarding the application for *BERLinPro*. Two slice emittance measurement techniques and the phase space tomography were applied in real accelerator environments. Experimental experience and skills in the data analysis based on the theoretical understanding were achieved.

The zero-phasing technique implemented at the ELBE SRF photoinjector (HZDR) was considered in detail, including the experimental setup, the data taking and data analysis procedures and the simulation of measured data. The temporal resolution of the ‘Brown-Buechner’-spectrometer was estimated to 78 fs – 1.9 ps, corresponding to at least five slices depending on the measurement conditions and the size of the entrance slit. The dependence of the slice emittance on the RF phase of the gun cavity was investigated using bunches of 18 MeV beam energy and 10 pC bunch charge. The measured slice emittance values vary between (0.5 – 2.5) mm mrad and the emittance profile along the bunch resembles the longitudinal intensity profile. The measured values lie within the expected range and were highly reproducible. The phase dependence could not be measured unambiguously. The lowest emittance values and flattest profiles were measured in the first measurement period for a small RF phase and for zero-crossing in the second period. The quality of the data analysis routine was verified using simulated data. Simulations of the measurements indicate a phase dependence contrary to the measurement, namely an emittance increase with a decreasing RF phase. The simulated emittance values of (0.5 – 1) mm mrad are lower than the measured values due to neglected space charge effects. Further slice emittance measurements were taken using a transverse deflector at the PEGASUS photoinjector (UCLA). The temporal resolution under measurement conditions was estimated to 610 fs and five slices of the 0.8 ps long bunch were analysed. The two measurement series performed at a beam energy of 3 MeV and a bunch charge of 10 pC delivered reproducible results. The emittance is 0.5 mm mrad for the outer slices and doubles in the centre of the bunch, meeting the expectations of values smaller than 1 mm mrad. The advantages and disadvantages of each technique were discussed. The zero-phasing technique may be applied using existing accelerator components and is suitable up to high beam energies. The deflector technique is more direct than the zero-phasing and is suitable for low beam energies in particular. A sufficient deflection for beams of high energy and high brightness is possible but takes a higher effort.

An image reconstruction routine based on MENT was developed for phase space tomography. It was tested using different model distributions, simulated data and measurements. The algorithm successfully reconstructed the distribution from three histograms for a normal distribution. More complex distributions require more histograms to be reconstructed properly. Six histograms were appropriate for measured data. The accuracy of the emittance calculated from the reconstructed normal distributions is 2 % for three histograms of 25 bins and 1 % using ten histograms of the same number of bins. The algorithm is robust against deviations from the equidistant angle distribution. The developed tools were successfully used during the commissioning phase of the BESSY II preinjector linac. Six projections of a 50 MeV beam with a bunch train charge of 2 nC were used. Slight asymmetries in phase space were revealed and the emittance calculated from the

reconstruction was found to be 25 mm mrad, meeting the expectations. In the last part, a potential deflector design to be used for slice diagnostics downstream of the *BERLinPro* gun was introduced. The requirements on the deflecting voltage were estimated as a function of the emittance and the β -function. A 2 MeV bunch of 5 ps length having a normalised emittance of 1 mm mrad requires a voltage of 213 kV when ten slices are to be analysed and $\beta = 10$ m. The estimated shunt impedance of 3.5 M Ω and available peak RF power of 10 kW were shown to be sufficient for measurements at 2 MeV. A potential use of the same design to deflect a 6 MeV beam downstream of the booster is possible at the expense of resolution and may serve as a temporary solution. In the long term, an advanced deflector design becomes necessary.

In conclusion, the investigated experimental techniques and the developed data analysis tools are highly suitable for extensive phase space studies. The combination of the tomographic reconstruction with a time-resolved technique allows for a completely model-independent full 5D (time-dependent transverse phase space) characterisation of the electron distribution. Depending on the technique, a temporal resolution in the ps or sub-ps range can be achieved. Extending the deflector technique by a dipole to allow for sliced energy spread measurement would extend the phase space investigation to a full 6D characterisation. This unique combination of multi-dimensional time-resolved phase space reconstruction is highly promising for the characterisation of high-brightness beams, including *BERLinPro*. The design of the slice diagnostic systems to be installed downstream of the injector and booster is still in its early stages. In a first step, the requirements on the deflector intended for measurements directly downstream of the gun were specified. Short- and medium-term plans include detailed specification of the design and adapting the existing analysis tools to *BERLinPro* needs. Future work at ELBE includes the improvement of the experiments and simulation tools. The measurement procedure as well as the analysis routines are planned to be automated to allow for extensive studies exploring emittance compensation schemes and their dependence on the bunch charge as well as the gun cavity phase. Furthermore, the simulations need to be improved by on-line modelling to clarify the discrepancies between measurement and simulation. The newly acquired experience will be taken into account for the implementation of the diagnostic tools at *BERLinPro*.

A Dispersion function for setups A1, A2 and A3

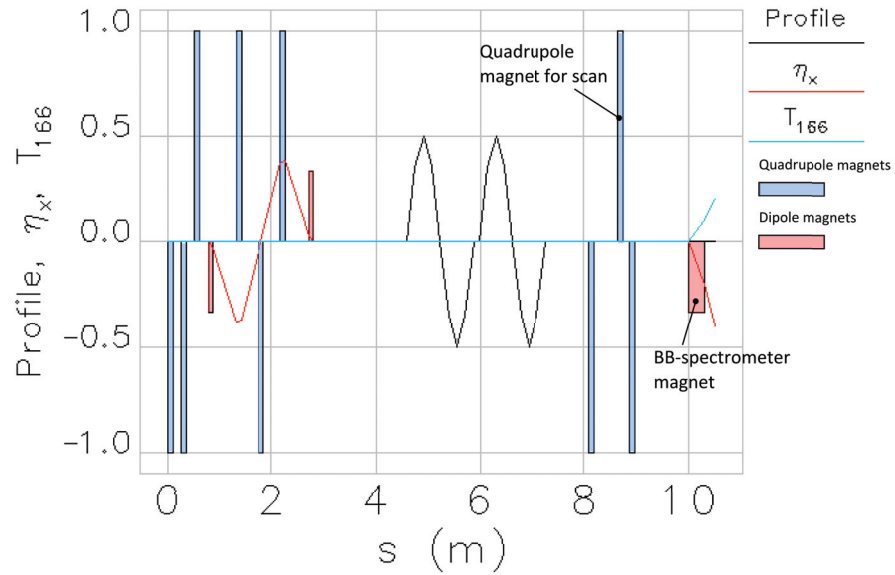


Figure A.1: First (red) and second order (blue) dispersion along the beamline for A1.

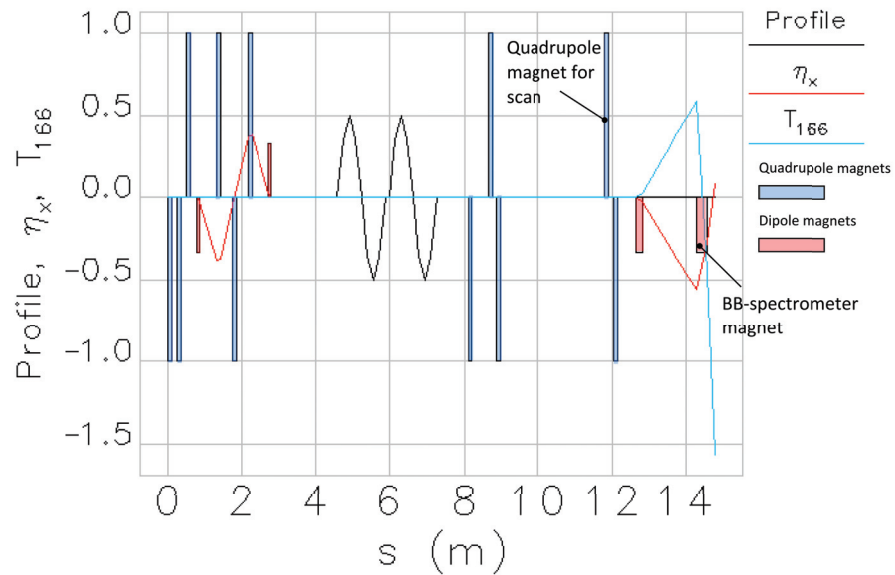


Figure A.2: First (red) and second order (blue) dispersion along the beamline for A2.

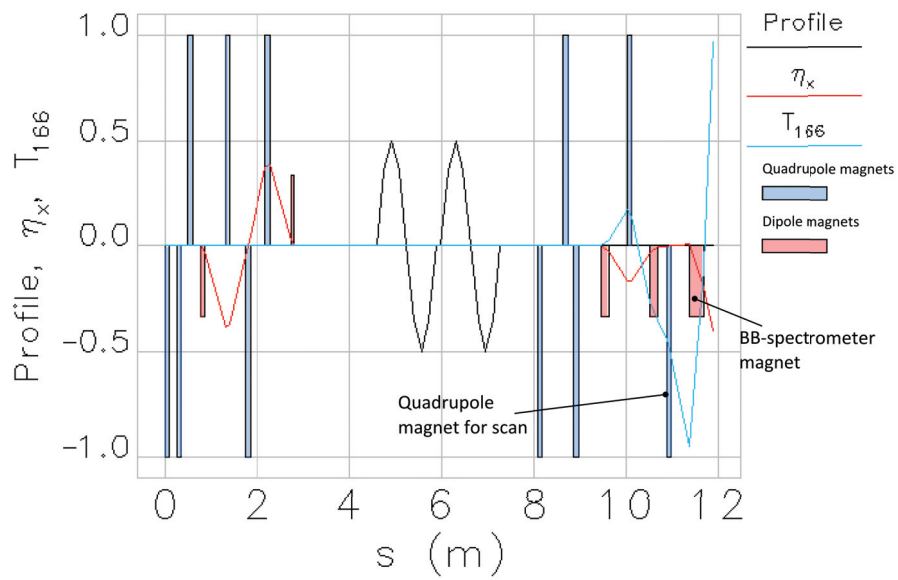
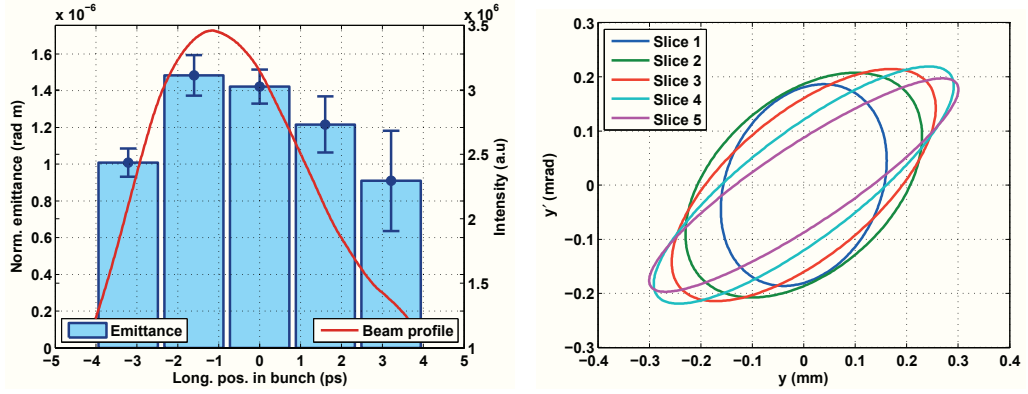


Figure A.3: First (red) and second order (blue) dispersion along the beamline for A3.

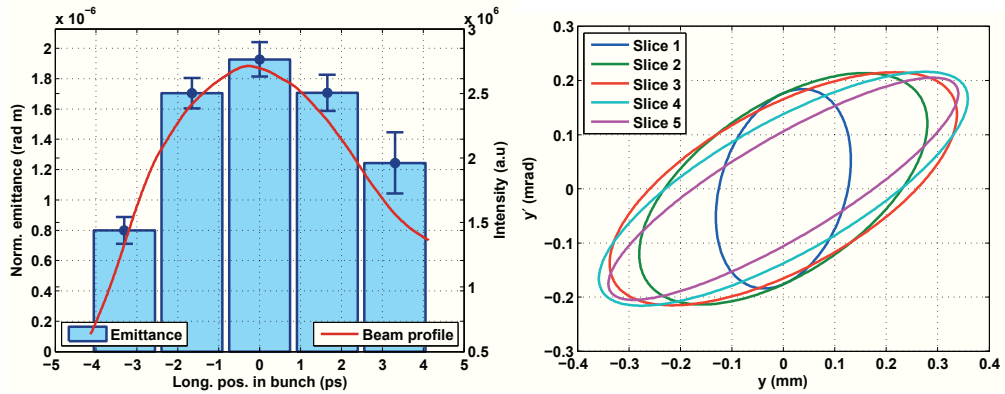
B Results of the zero-phasing measurements



(a) Vertical slice emittance.

(b) Reconstructed vertical phase space.

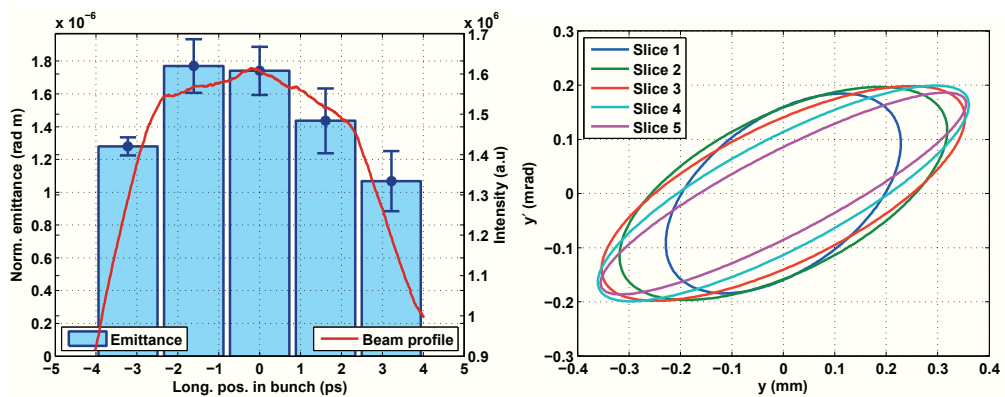
Figure B.1: Zero-phasing: slice emittance for measurement 'series 1' (2010)



(a) Vertical slice emittance.

(b) Reconstructed vertical phase space.

Figure B.2: Zero-phasing: slice emittance for measurement 'series 2' (2010)



(a) Vertical slice emittance.

(b) Reconstructed vertical phase space.

Figure B.3: Zero-phasing: slice emittance for measurement 'series 3' (2010)

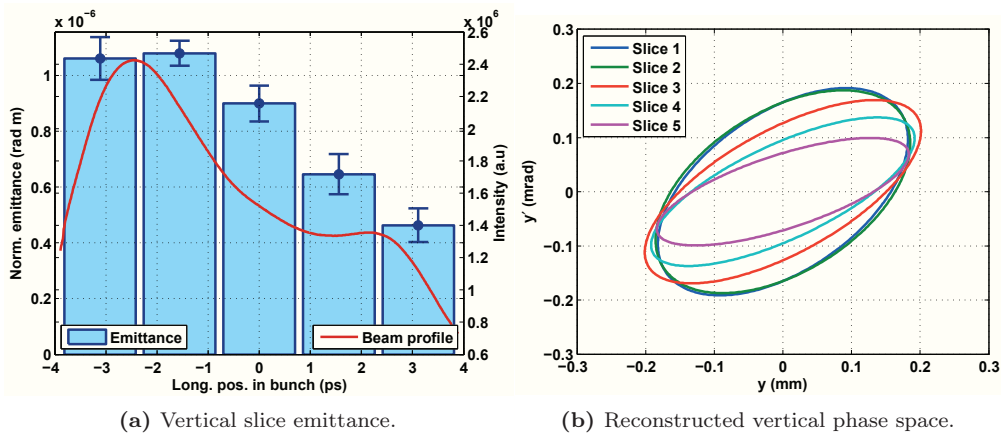


Figure B.4: Zero-phasing: slice emittance for measurement 'series 4' (2010)

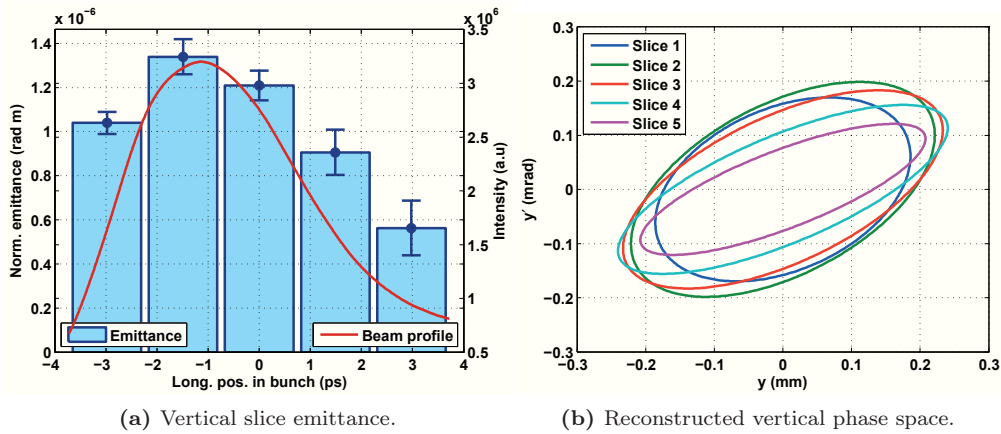


Figure B.5: Zero-phasing: slice emittance for measurement 'series 5' (2010)

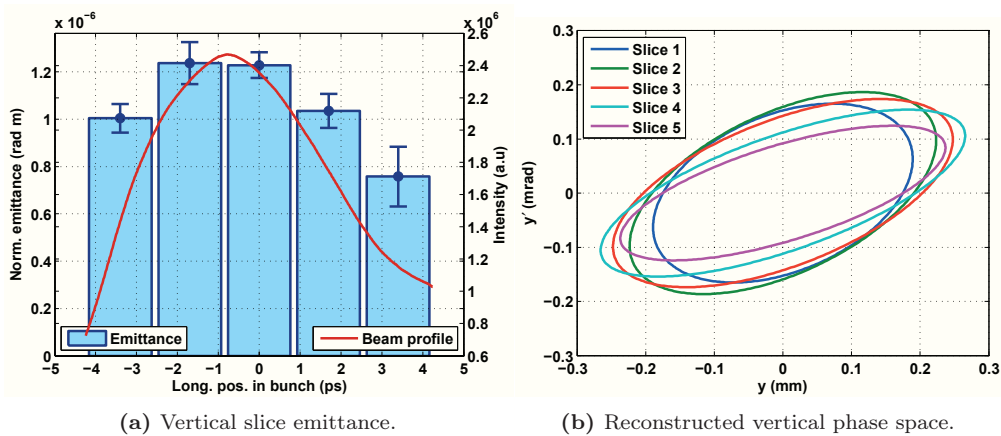


Figure B.6: Zero-phasing: slice emittance for measurement 'series 6' (2010)

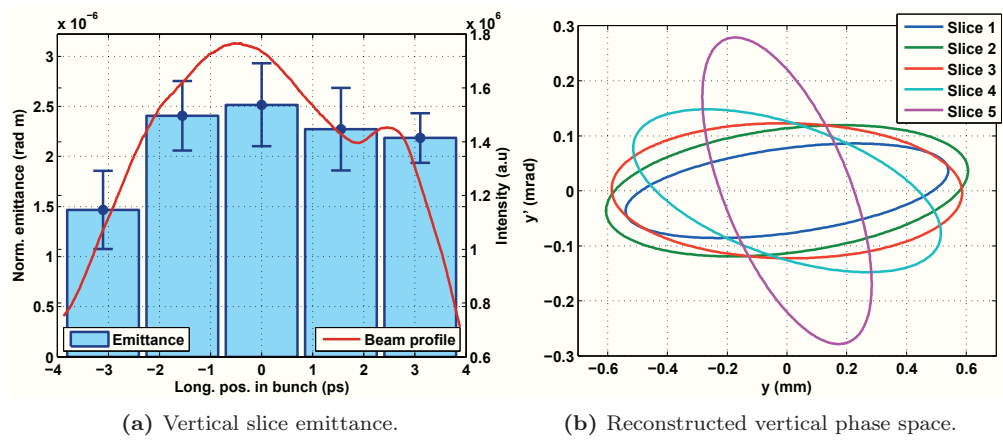


Figure B.7: Zero-phasing: slice emittance for measurement 'series 7' (2011)

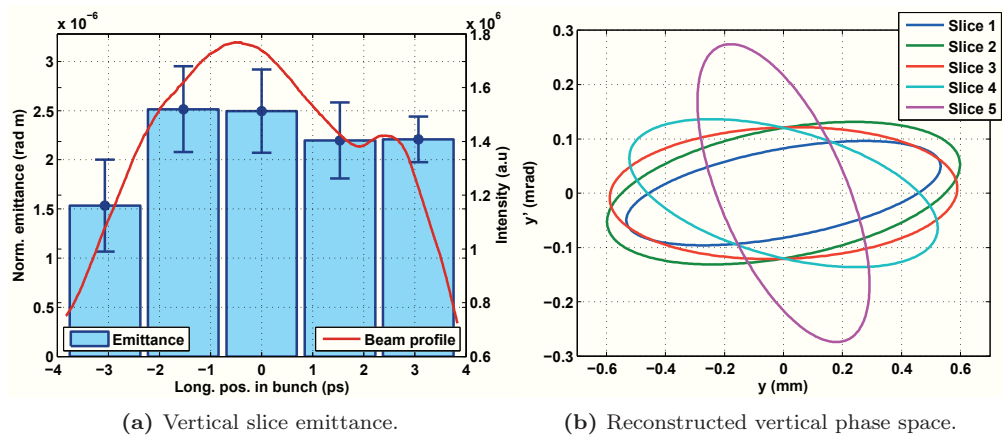


Figure B.8: Zero-phasing: slice emittance for measurement 'series 8' (2011)

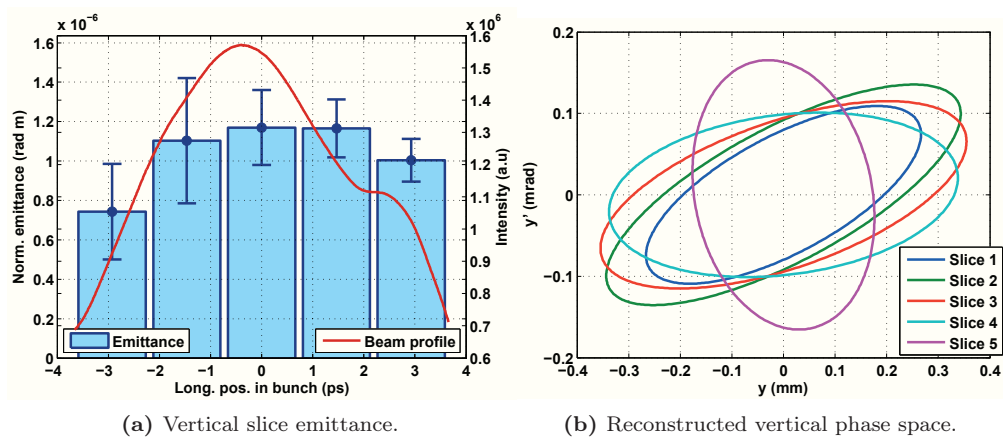


Figure B.9: Zero-phasing: slice emittance for measurement 'series 9' (2011)

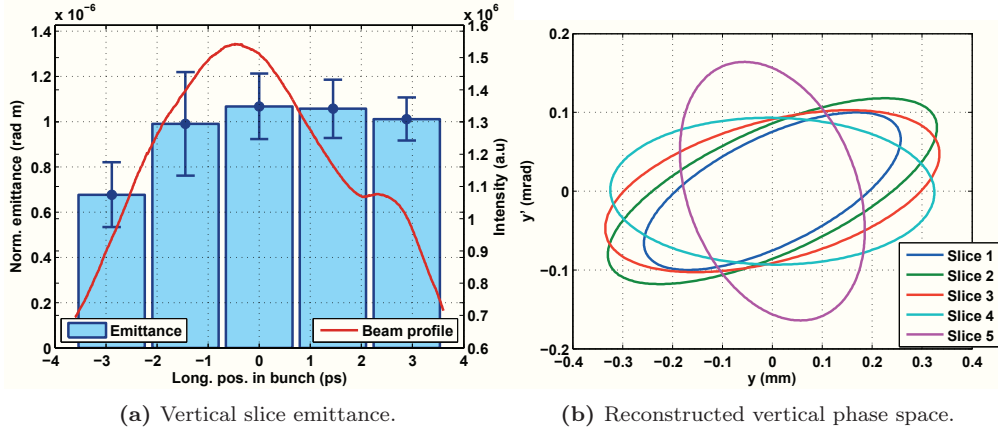


Figure B.10: Zero-phasing: slice emittance for measurement ‘series 10’ (2011)

Table B.1: Summary of the slice emittance values measured during the first and second measurement period. For measurement conditions see Section 5.1.2.

Slice	Normalised emittance (mm mrad)				
	‘Series 1’	‘Series 2’	‘Series 3’	‘Series 4’	‘Series 5’
1	0.10 ± 0.08	0.80 ± 0.09	1.28 ± 0.06	1.06 ± 0.08	1.04 ± 0.05
2	1.48 ± 0.11	1.70 ± 0.10	1.77 ± 0.16	1.08 ± 0.05	1.34 ± 0.08
3	1.42 ± 0.93	1.93 ± 0.11	1.74 ± 0.15	0.90 ± 0.06	1.21 ± 0.07
4	1.22 ± 0.15	1.71 ± 0.12	1.44 ± 0.20	0.65 ± 0.07	0.91 ± 0.10
5	0.91 ± 0.27	1.24 ± 0.20	1.07 ± 0.18	0.46 ± 0.06	0.56 ± 0.14
	‘Series 6’	‘Series 7’	‘Series 8’	‘Series 9’	‘Series 10’
1	1.01 ± 0.06	1.47 ± 0.39	1.53 ± 0.49	7.43 ± 0.24	0.68 ± 0.14
2	1.24 ± 0.09	2.41 ± 0.35	2.52 ± 0.44	1.10 ± 0.32	0.99 ± 0.23
3	1.23 ± 0.07	2.52 ± 0.41	2.50 ± 0.42	1.17 ± 0.19	1.07 ± 0.14
4	1.04 ± 0.07	2.27 ± 0.41	2.20 ± 0.39	1.17 ± 0.15	1.06 ± 0.13
5	0.76 ± 0.13	2.18 ± 0.25	2.21 ± 0.23	1.00 ± 0.11	1.01 ± 0.09

C Testing the tomographic reconstruction algorithm

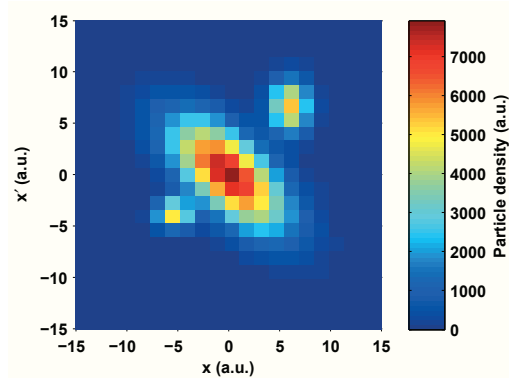


Figure C.1: Model distribution of three partly overlapping normal distributions.

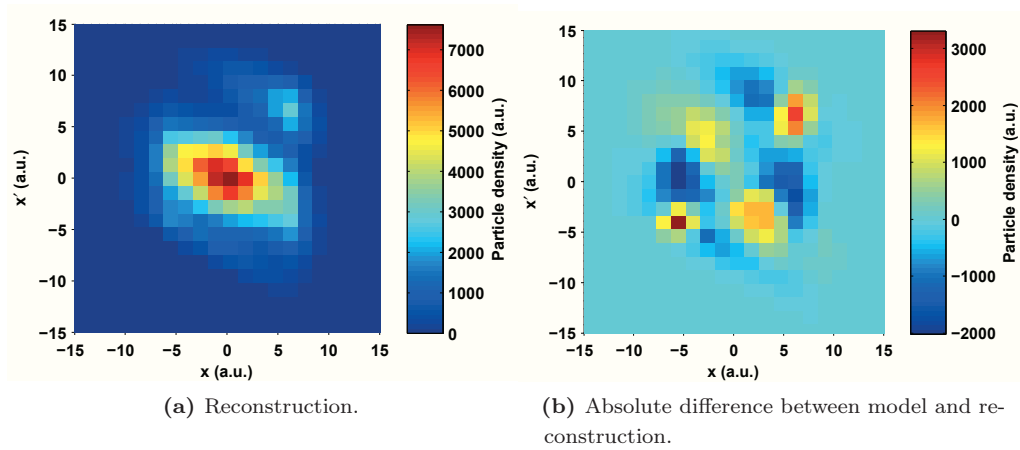


Figure C.2: Reconstruction of three partly overlapping normal distributions from three histograms and 25 bins.

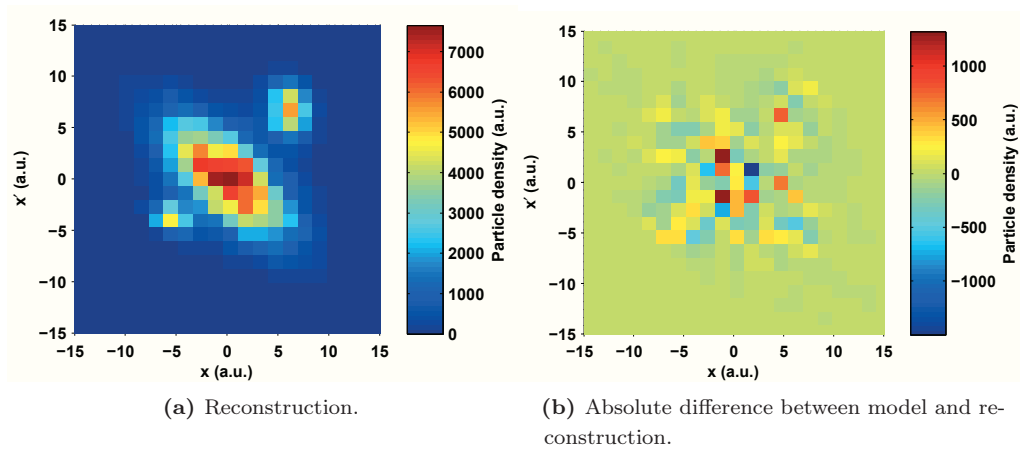


Figure C.3: Reconstruction of three partly overlapping normal distributions from ten histograms and 25 bins.

References

- [1] J. KNOBLOCH, M. ABO-BAKR, W. ANDERS, R. BARDAY, K. BÜRKMANN-GEHRLEIN, V. DÜRR, S. HESSLER, A. JANKOWIAK, T. KAMPS, O. KUGELER, B. KUSKE, P. KUSKE, A. MATVEENKO, G. MEYER, R. MÜLLER, A. NEUMANN, K. OTT, Y. PETENEV, D. PFLÜCKHAHN, T. QUAIST, J. RAHN, AND S. SCHUBERT, *Status of the BERLinPro Energy Recovery Linac Project*, Proceedings of IPAC 2012, New Orleans, Louisiana, USA, (2012), pp. 601–603.
- [2] J. TEICHERT, A. BUECHNER, P. EVTUSHENKO, F. GABRIEL, U. LEHNERT, P. MICHEL, AND J. VOIGTLÄNDER, *Results of Beam Parameter Measurement of the ELBE Electron Accelerator after Commissioning*, Nuclear Instruments and Methods in Physics Research A, 507 (2003), pp. 354–356.
- [3] P. MUSUMECI, J. MOODY, AND G. GATTI, *Ultrafast Beam Research at the PEGASUS Laboratory*, Proceedings of PAC07, Albuquerque, New Mexico, USA, (2007), pp. 2751–2753.
- [4] C. LEJEUNE AND J. AUBERT, *Emittance and Brightness: Definitions and Measurements*, Advances in Electronics and Electron Physics, Supplement 13A, (1980).
- [5] P. STREHL, *Beam Instrumentation and Diagnostics*, Springer-Verlag Berlin Heidelberg, 2006.
- [6] U. MORTENSEN, *Vektoren und Matrizen für Anwendungen in der multivariaten Statistik*. Skriptum zur Vorlesung: Evaluation und Forschungsmethoden Statistik III + IV, Westfälische Wilhelms-Universität Münster, 2007.
- [7] H. MALLOT, *Wissenschaftliches Rechnen für Neurowissenschaftler*. Vorlesungsskript, Eberhard Karls Universität Tübingen, 2009.
- [8] F. HINTERBERGER, *Physik der Teilchenbeschleuniger und Ionenoptik*, Springer-Verlag Berlin Heidelberg, 1997.
- [9] A. W. CHAO AND M. TIGNER, eds., *Handbook of Accelerator Physics and Engineering*, World Scientific, 1999, ch. Optics and Lattices: Single Element Optics.
- [10] H. WIEDEMANN, *Particle Accelerator Physics*, vol. 1, Springer-Verlag Berlin Heidelberg New York, 2007.
- [11] J. FELDHAUS, J. ARTHUR, AND J. B. HASTINGS, *X-ray Free-Electron Lasers*, Journal of Physics B: Atomic, Molecular and Optical Physics, 38 (2005), pp. 799–819.
- [12] *LCLS Parameters*. Available at https://slacportal.slac.stanford.edu/sites/lclscore_public/Accelerator_Physics_Published_Documents/LCLS-parameters.pdf, March 2011.
- [13] M. J. VAN DER WIEL, *Applications of High-Brightness Electron Beams*, The 2nd ICFA Advanced Accelerator Workshop on The Physics of High Brightness Beams, UCLA, Los Angeles, USA, (1999).
- [14] N. THOMPSON, *Introduction to Free-Electron Lasers*. Available at http://www.stfc.ac.uk/ASTeC/Resources/PDF/Thompson_FELs.pdf, Jan. 2012.
- [15] *Linac Coherent Light Source (LCLS) Conceptual Design Report*, 2002. SLAC.
- [16] A. ZHOLENTS, *Beam Parameter Trade Offs for Free-Electron Lasers*. Talk at the Workshop on Application of Dielectric Wakefield Accelerators to Next Generation X-ray Free-Electron Laser Facilities, Argonne, USA, 2011.

- [17] *The European X-Ray Free-Electron Laser Technical Design Report*, 2007. DESY Hamburg, DESY 2006-097.
- [18] A. MOSTACCI, A. BACCI, M. BOSCOLO, E. CHIADRONI, A. CIANCHI, D. FILIPPETTO, M. MIGLIORATI, P. MUSUMECI, C. RONSIVALLE, AND A. R. ROSSI, *Analysis Methodology of Movable Emittance-Meter Measurements for Low Energy Electron Beams*, *Review of Scientific Instruments*, 79 (2008), p. 013303.
- [19] F. LÖHL, *Measurements of the Transverse Emittance at the VUV-FEL*, diploma thesis, University of Hamburg, 2005.
- [20] K. T. McDONALD AND D. P. RUSSELL, *Methods of Emittance Measurement*, tech. report, Joseph Henry Laboratories, Princeton University, 1989.
- [21] M. G. MINTY AND F. ZIMMERMANN, *Measurement and Control of Charged Particle Beams*, Springer-Verlag Berlin Heidelberg, 2003.
- [22] H. PRUYS, *Die Methode der kleinsten Quadrate. Vorlesungsskript Datenanalyse*, Sommersemester 2004, Universität Zürich, 2004.
- [23] S. LIDIA, *RF and Space Charge Emittance in Guns*. USPAS course on High Brightness Electron Injectors for Light Sources, 2007.
- [24] B. E. CARLSTEN, *New Photoelectric Injector Design for the Los Alamos National Laboratory XUV FEL Accelerator*, *Nuclear Instruments and Methods in Physics Research A*, 285 (1989), pp. 313–319.
- [25] X. QIU, K. BATCHELOR, I. BEN-ZVI, AND X.-J. WANG, *Demonstration of Emittance Compensation through the Measurement of the Slice Emittance of a 10-ps Electron Bunch*, *Physical Review Letters*, 76 (1996), pp. 3723–3726.
- [26] J. SCHMERGE, P. BOLTON, J. CLENDENIN, D. DOWELL, S. GIERMAN, C. LIMBORG, AND B. MURPHY, *6D Phase Space Measurements at the SLAC Gun Test Facility*, tech. report, SLAC, 2003. SLAC-PUB-9681, LCLS-TN-03-1.
- [27] D. WANG, G. A. KRAFFT, AND C. K. SINCLAIR, *Measurement of Femtosecond Electron Bunches using a RF Zero-Phasing Method*, *Physical Review E*, 57 (1998), pp. 2283–2286.
- [28] THE MATHWORKS, INC., *MATLAB R2012a*.
- [29] M. RÖHRS, *Investigation of the Phase Space Distribution of Electron Bunches at the FLASH-Linac using a Transverse Deflecting Structure*, PhD thesis, Universität Hamburg, 2008.
- [30] Y. DING, A. BRACHMANN, F.-J. DECKER, D. DOWELL, P. EMMA, J. FRISCH, S. GILEVICH, G. HAYS, P. HERING, Z. HUANG, R. IVERSON, H. LOOS, A. MIAHNAHRI, H.-D. NUHN, D. RATNER, J. TURNER, J. WELCH, W. WHITE, AND J. WU, *Measurements and Simulations of Ultralow Emittance and Ultrashort Electron Beams in the LCLS*, *Physical Review Letters*, 102 (2009), p. 254801.
- [31] R. AKRE, L. BENTSON, P. EMMA, AND P. KREJCIK, *Bunch Length Measurements using a Transverse RF Deflecting Structure in the SLAC LINAC*, *Proceedings of EPAC 2002*, Paris, France, (2009), pp. 1882–1884.
- [32] D. ALESINI, *RF Deflector Based sub-ps Beam Diagnostics: Application to FEL and Advanced Accelerators*, *The Physics and Applications of High Brightness Electron Beams*, *Proceedings of the 46th Workshop of the INFN ELOISATRON Project*, Erice, Italy, (2005).

- [33] A. V. FERRAROTTO, *Design und Charakterisierung eines TM_{110} -HF-Deflektors zur longitudinalen Strahldiagnose von Pikosekunden-Elektronenbunchen im MeV-Bereich*, diploma thesis, Technische Universität Dortmund, 2011.
- [34] *Longitudinal Phase Space Measurement*. Available at http://pbpl.physics.ucla.edu/Research/Facilities/PEGASUS/Long_Phase_Space/, Jan. 2012.
- [35] R. AKRE, D. DOWELL, P. EMMA, J. FRISCH, S. GILEVICH, G. HAYS, P. HERING, R. IVERSON, C. LIMBORG-DEPREY, H. LOOS, A. MIAHNAHRI, J. SCHMERGE, J. TURNER, J. WELCH, W. WHITE, AND J. WU, *Commissioning the Linac Coherent Light Source Injector*, Physical Review Special Topics - Accelerators and Beams, 11 (2008), p. 030703.
- [36] A. ARNOLD, H. BÜTTIG, D. JANSSEN, T. KAMPS, G. KLEMZ, W. LEHMANN, U. LEHNERT, D. LIPKA, F. MARHAUSER, P. MICHEL, K. MÖLLER, P. MURCEK, C. SCHNEIDER, R. SCHURIG, F. STAUFENBIEL, J. STEPHAN, J. TEICHERT, V. VOLKOV, I. WILL, AND R. XIANG, *Development of a Superconducting Radio Frequency Photoelectron Injector*, Nuclear Instruments and Methods in Physics Research A, 577 (2007), p. 440.
- [37] T. KAMPS, A. ARNOLD, D. BÖHLICK, M. DIRSAT, G. KLEMZ, D. LIPKA, T. QUAST, J. RUDOLPH, M. SCHENK, F. STAUFENBIEL, J. TEICHERT, AND I. WILL, *Electron Beam Diagnostics for a Superconducting Radio Frequency Photoelectron Injector*, Review of Scientific Instruments, 79 (2008), p. 093301.
- [38] J. TEICHERT, *Status and Future Plans for the SRF Gun at ELBE*. Talk at the ICFA Advanced Beam Dynamics Workshop on Future Light Sources, Newport News, USA, 2012.
- [39] J. TEICHERT, *High Rep Rate Guns: FZD Superconducting RF Photogun*. Talk at the ICFA Advanced Beam Dynamics Workshop on Future Light Sources, Menlo Park, California, 2010.
- [40] J. TEICHERT, A. ARNOLD, H. BÜTTIG, D. JANSSEN, M. JUSTUS, U. LEHNERT, P. MICHEL, P. MURCEK, C. SCHNEIDER, R. SCHURIG, F. STAUFENBIEL, R. XIANG, T. KAMPS, J. RUDOLPH, M. SCHENK, G. KLEMZ, AND I. WILL, *Status of the SRF Gun Operation at ELBE*, Proceedings of FEL, Malmö, Sweden, (2010), pp. 453–456.
- [41] C. BROWNE AND W. BUECHNER, *Broad-Range Magnetic Spectrograph*, The Review of Scientific Instruments, 27 (1956), pp. 899–907.
- [42] W. BUECHNER, M. MAZARI, AND A. SPERDUTO, *Magnetic Spectrograph Measurements on the $Al^{27}(d,p)Al^{28}$ Reaction*, Physical Review, 101 (1956), pp. 188–195.
- [43] K. DUNKEL, *FZD Spektrometer Design Report*, ACCEL, 2008.
- [44] M. MLADJENOVIC, *Development of Magnetic β -Ray Spectroscopy*, Springer-Verlag Berlin Heidelberg New York, 1976, ch. Prismatic (Sector) Spectrometers.
- [45] M. BORLAND, *elegant: A Flexible SDDS-Compliant Code for Accelerator Simulation*, Advanced Photon source, 2000.
- [46] *Mobiles Elektronen-Energie Spektrometer FZD Forschungszentrum Dresden, Handbuch*, tech. report, RI Research Instruments GmbH, 2008.
- [47] J. TEICHERT, 2011. private communication.
- [48] D. ROBIN, G. PORTMANN, H. NISHIMURA, AND J. SAFRANEK, *Model Calibration and Symmetry Restoration of the Advanced Light Source*, Proceedings of EPAC, Barcelona, Spain, (1996).

- [49] J. TEICHERT, A. ARNOLD, H. BÜTTIG, D. JANSSEN, M. JUSTUS, U. LEHNERT, P. MICHEL, P. MURCEK, A. SCHAMLOTT, C. SCHNEIDER, R. SCHURIG, F. STAUFENBIEL, R. XIANG, T. KAMPS, J. RUDOLPH, M. SCHENK, G. KLEMZ, AND I. WILL, *Initial Commissioning Experience with the Superconducting RF Photoinjector at ELBE*, Proceedings of FEL, Gyeongju, Korea, (2008), pp. 467–472.
- [50] K. FLOETTMANN, *ASTRA: A Space Charge Tracking Algorithm*, DESY.
- [51] L. SERAFINI AND J. ROSENZWEIG, *Envelope Analysis of Intense Relativistic Quasilinear Beams in RF Photoinjectors: A Theory of Emittance Compensation*, Physical Review E, 55 (1997), pp. 7565–7590.
- [52] I. BAZAROV AND G. KRAFFT, *Electron Sources: Space Charge in Injectors*. USPAS Course on Recirculated and Energy Recovered Linacs, 2008.
- [53] *Photoelectron Generated Amplified Spontaneous Radiation Source (PEGASUS)*. Available at <http://pbpl.physics.ucla.edu/Research/Facilities/PEGASUS>, May 2012.
- [54] J. MOODY, M. GUTIERREZ, P. MUSUMECI, AND C. SCOPY, *Longitudinal Beam Dynamics of The Photoinjector Blowout Regime*, Proceedings of PAC, Vancouver, Canada, (2009), pp. 1–3.
- [55] R. J. ENGLAND, *Longitudinal Shaping of Relativistic Bunches of Electrons Generated by an RF Photoinjector*, PhD thesis, University of California Los Angeles, 2007.
- [56] P. MUSUMECI, J. T. MOODY, C. M. SCOPY, M. S. GUTIERREZ, AND T. TRAN, *RF Streak Camera Based Ultrafast Relativistic Electron Diffraction*, Review of Scientific Instruments, 80 (2009), p. 013302.
- [57] P. MUSUMECI, 2010. private communication.
- [58] S. BELOMESTNYKH, V. SHEMELIN, K. SMOLENSKI, AND V. VESHCHEREVICH, *Deflecting Cavity for Beam Diagnostics in ERL Injector*, Proceedings of PAC, Albuquerque, USA, (2007), pp. 2331–2333.
- [59] A. V. FERRAROTTO, 2011. private communication.
- [60] J. W. WANG AND S. TANTAWI, *X-Band Travelling Wave RF Deflector Structures*. SLAC-PUB-13444, 2008.
- [61] T. LEHMANN, W. OBERSCHELP, E. PELIKAN, AND R. REPGES, *Bildverarbeitung für die Medizin: Grundlagen · Modelle · Methoden · Anwendungen*, Springer-Verlag Berlin Heidelberg New York, 1997.
- [62] G. MINERBO, *MENT: A Maximum Entropy Algorithm for Reconstructing a Source from Projection Data*, Computer Graphics and Image Processing, 10 (1979), pp. 48–68.
- [63] J. J. SCHEINS, *Tomographic Reconstruction of Transverse and Longitudinal Phase Space Distributions using the Maximum Entropy Algorithm*, tech. report, DESY, 2004. TESLA Report 2004-08.
- [64] K. WILLE, *The Physics of Particle Accelerators*, Oxford University Press, 2005.
- [65] M. RÖHRS, C. GERTH, H. SCHLARB, B. SCHMIDT, AND P. SCHMÜSER, *Time-Resolved Electron Beam Phase Space Tomography at a Soft X-Ray Free-Electron Laser*, Physical Review Special Topics - Accelerators and Beams, 12 (2009), p. 050704.
- [66] D. STRATAKIS, R. A. KISHEK, R. B. FIORITO, K. TIAN, I. HABER, P. O’SHEA, M. REISER, AND J. C. T. THANGARAJ, *Time-Dependent Phase-Space Characteriza-*

tion of Intense Charged Particle Beams, Physical Review Special Topics - Accelerators and Beams, 12 (2009), p. 020101.

- [67] M. G. IBISON, K. M. HOCK, D. J. HOLDER, AND M. KOROSTELEV, *Development of Tomographic Reconstruction Methods for Studies of Transverse Phase Space in the EMMA FFAG Injection Line*, Proceedings of IPAC, Kyoto, Japan, (2010), pp. 4346–4348.
- [68] G. KOURKAFAS, G. ASOVA, J. BÄHR, S. KHODYACHYKH, M. KRASILNIKOV, J. MEISSNER, A. OPPELT, AND F. STEPHAN, *Tomography Module for Transverse Phase-Space Measurements at PITZ*, Proceedings of DITANET, Seville, Spain, (2011).
- [69] T. ATKINSON, V. DÜRR, M. HELMECKE, D. SCHÜLER, E. WEIHRETER, D. JOUSSE, J.-L. PASTRE, AND A. SETTY, *Commissioning of the 50 MeV Preinjector Linac for the BESSY II Facility*, Proceedings of IPAC, San Sebastian, Spain, (2011), pp. 3140–3142.
- [70] T. ATKINSON, 2011. private communication.
- [71] A. MATVEENKO, 2012. private communication.
- [72] W. ANDERS, 2012. private communication.
- [73] *BERLinPro Conceptual Design Report*, 2012. Helmholtz-Zentrum Berlin.

Selbständigkeitserklärung

Ich erkläre, dass ich die vorliegende Dissertation selbständig und ohne fremde Hilfe verfasst, andere als die von mir angegebenen Quellen und Hilfsmittel nicht benutzt und die den benutzten Werken wörtlich oder inhaltlich entnommenen Stellen als solche kenntlich gemacht habe.

Rostock, den 18.09.2012

Jeniffa Rudolph